Structural and Spin Peierls Transitions In Charge Transfer Complexes

Henderson, James

Award date:
2020

Awarding institution:
University of Bath

Structural and Spin Peierls Transitions In Charge Transfer Complexes

submitted by

James Martindale Henderson

for the degree of Doctor of Philosophy

of the

University of Bath

Department of Physics

September 2019

Abstract

This thesis examines and characterises structural transitions in two different organic charge transfer complexes: peryelene-tetracyanoquinodimethane (Perylene-TCNQ) and dibenzotetrathiafulvalene-tetraflourotetracyanoquinodimethane (DTTF-F_4TCNQ. Both complexes were grown via physical vapour transport using a Carbolite EHC 12/600B three zone furnace.

We experimentally established two completely novel polymorphs of Perylene-TCNQ and demonstrated that these polymorphs undergo a reversible temperature dependent phase transition, converting from one to the other, at around 280 K. We characterised the physical structure of both polymorphs using x-ray crystallography and provided estimates for the degree of charge transfer via bond length based methods and infra-red spectroscopy. Notably, we discovered that the benzene rings of perylene are heavily distorted in both polymorphs. This is unusual as it is normally extremely energetically favourable for aromatic rings to be planar. This deviation appears to be a result of nitrogen short contact interactions. These results have been published in "New Polymorphs of Perylene:Tetracyanoquinodimethane Charge Transfer Cocrystals", *Cryst. Growth Des.* 2018, 18, 4, 2003-2009. (https://doi.org/10.1021/acs.cgd.7b01391)

For DBTTF-F_4TNCQ we demonstrated a hitherto unconfirmed high temperature Spin Peierls induced structural transition close to 400 K. This transition can be seen in both the unit cell parameters and the relative inter-molecular distances between adjacent DBTTF and F_4TCNQ molecules, as determined by x-ray crystallography. While this behaviour was previously predicted it has never been experimentally confirmed until now. In the process we also ascertained, via both bond length and spectroscopic methods, that the degree of charge transfer does not appear to change over this structural transition.

We also performed low temperature measurements to further probe the behaviour of the DBTTF-F_4TCNQ system. Electron Paramagnetic Resonance (EPR) measurements were carried out and appear to demonstrate a low temperature transition at around 150 K. We also carried out low temperature x-ray crystallography measurements in an attempt to ascertain any corresponding structural changes, but the results were inconclusive.

Acknowledgements

I would like to thank my colleagues at the *Dipartimento di Scienze Chimiche* at Parma University and the *Dipartimento di Chimica Industriale Toso Montanari* at the University of Bologna Research Unit for their spectroscopic measurements. I would also like to thank collaborators at the Chemical Research Support at the Faculty of Chemistry of the Weizmann Institute of Science for their electron paramagnetic resonance measurements, and the Advanced Light Source at the Lawrence Berkeley National Laboratory and the Chemical Characterisation and Analysis Facility (CCAF) at the University of Bath for their x-ray diffraction facilities.

I also grateful to the Engineering and Physical Sciences Research Council (EPSRC) for providing a Doctoral Training Partnership (DTP) studentship to support this research.

Finally, I am indebted to the numerous technical support staff: Harry Bone, Philip Jones, Martin Fullick, Richard Cousins, Paul Reddish and Wendy Lambson, for their tireless assistance in the face of equipment failure, technical difficulties and, in one case, an exploding resistor. Without their assistance many of these experiments would not have been possible.

Contents

Chapter 1

Introduction

1.1 Preface

"So what's your PhD about?"

This is a question every PhD student is asked sooner or later, and one that most dread. Part of the problem is that there are often several layers of explanation to be given before one can even get round to answering the question. "I'm looking at transitions in charge transfer complexes" is a useless answer to the vast majority of people, who have no idea what a charge transfer complex is, or why it matters that they have transitions. Then one has to try and manage an explanation in the hope that the questioner does not get bored half way through, assuming they were actually even interested in the first place, and were not just asking out of some sense of social obligation.

The study of charge transfer (CT) complexes sits at a crossroads. It is in part organic chemistry, and in part condensed matter physics. Due to the complex and difficult process of making CT complexes, it incorporates a bit of process engineering as well. The field itself is also a mixture of new and old; it has come back into vogue again after a brief flurry of research interest almost 50 years ago. It could lead to the future of flexible, wearable electronics, or cheap printable solar panels. It is a fascinating field, but not one that can be readily explained in 30 seconds to someone who knows nothing about it. I've been asked the opening question many times at this point, and the explanation I've converged on is something like this:

"I look at a type of material known as 'charge transfer complexes'. Just as you can bind atoms together to make molecules that have new properties, these are molecules

that are bound together like Lego bricks in what's called a supra-molecular complex. Sodium is a metal, chlorine is a toxic gas, sodium chloride is table salt. In exactly the same way, I can stick two insulating molecules together and make something that's a conductor, or a semiconductor, or maybe even a superconductor."

In theory I could continue my explanation, talking about why this is actually interesting, and the applications that it might lead to. There is a lot that such an answer does not even attempt to cover. The majority of the time, however, whomever I'm talking to will either clearly have got bored or have asked another question at this point. Their initial enquiry was just to be polite. If you are reading this thesis, presumably you are actually interested in the answer, and as you read it, I hope that you will come to understand what exactly a charge transfer complex is, and why it matters that they have transitions.

1.2 Overview

This thesis is divided into eight chapters. The first chapter, this one, is the Introduction, and it provides a broad overview of the entire work. The second, Background, explains what CT complexes are, and why people study them. Chapter Three reviews the principles and theoretical underpinnings for the experimental techniques used in this work. It covers both crystal growth and the range of analytic tools used to study the crystals after they were grown.

Chapter Four describes the specific chemicals used, pereylene, dibenzotetrathiafulvalene (DBTTF), tetracyanoquinodimethane (TCNQ) and its fluorinated derivatives. It describes their properties in isolation as well as when combined together into specific CT complexes. Chapter Five covers specific experimental procedure. While Chapter Three gave the theory, this chapter details specific procedures and experimental protocols that were developed, and why.

Chapters Six and Seven cover the actual results of the work. Chapter Six covers the discovery of two novel polymorphs of perylene-TCNQ, and the reversible interconversion between the two. Chapter Seven looks into high and low temperature spin transitions in DBTTF-F_4TCNQ. Chapter Eight is the Conclusion.

Chapter 2

Background

2.1 Introduction

In this chapter we discuss the properties of charge transfer complexes and the theoretical models used to describe them. We also examine the current state of the field regarding their study.

2.2 Charge Transfer Complexes

A charge transfer (CT) complex is a supramolecular structure formed by the association of two or more molecules which are bonded together by electrostatic attraction due to partial charge transfer between the Highest Occupied Molecular Orbital (HOMO) of electron rich donor molecules and the Lowest Unoccupied Molecular Orbital (LUMO) of electron deficient acceptors. These complexes have received research interest due to the fact they can display novel optoelectronic properties not seen in the compounds that make them up. This started with the discovery of the organic metal TTF-TCNQ (tetrathiafulvalene-tetracyanoquinodimethane) in 1973 [2]; in isolation TCNQ and TTF have unremarkable electrical properties, but combined together they form an organic conductor that exhibits metallic conductivity for temperatures above 58 K, with a peak conductivity of 1.47×10^4 S cm^{-1} reported at 66 K. [18]

Much of this early work focused on the creation of high temperature superconductors or simply the creation of materials with high room temperature conductivity. More recently, charge transfer complexes have seen renewed interest in the field of organic

electronics due to a much wider range of technologically relevant properties in light emitting diodes and solar cells. [31] Of critical importance is that is it very easy to tune the electronic properties of charge transfer complexes by changing the molecular arrangement or by functionalising the electronegativity of one or more of the molecules, such as by fluorination.

One main area of research concerns the creation of organic semiconductors. Most integrated circuits utilise complementary metal oxide semiconductor (CMOS) structures, which rely on complementary pairs of p- and n-type field effect transistor (FET) channels for logic functions. To create efficient low power organic integrated circuits it is important to be able to replicate this capacity and, ideally, produce single layer systems capable of operating in both p- and n-type modes. Unfortunately most monomolecular organic compounds are unipolar (typically p-type) and are therefore unsuitable for the task. [33] This is not necessarily the case for charge transfer complexes, however. For example, the charge transfer complex DBTTF-TCNQ (dibenzotetrathiafulvalene-tetracyanoquinodimethane) has demonstrated an electron mobility of 0.13 cm^2 V^{-1} s^{-1} and a hole mobility of 0.04 cm^2 V^{-1} s^{-1}, both acceptable values for organic semiconductors. [110] Furthermore, it is possible to drastically alter the electrical properties of this complex by fluorinating the TCNQ molecule, changing the electronegativity of the acceptor and converting it from n-type, to ambipolar, and to p-type devices by shifting the Fermi-energy with respect to the semiconductor band gap energy. [100]

Charge transfer complexes have also demonstrated potential for efficient photocurrent generation. [4] One main problem with current organic photovoltaic cells (OPCs) is the efficient photogeneration of charge carriers. For OPCs, the first step in photocurrent generation is the creation of excitons, or bound electron-hole pairs. [82] These excitons subsequently charge separate, and then electrons are transported to the cathode, and holes to the anode, producing a current.

For single layer OPCs this occurs via the formation of Frenkel excitons, which are highly localised and confined to a single molecule. Unfortunately, this means that the excitons readily recombine before they can form an electron-hole pair and this also limits the active photon-energy range for excitonic absorption to above 1.7 eV. [105]

However, by using solar cells consisting of a donor-acceptor pair it is possible to engineer a system where the hole and electron occupy adjacent molecules, known as charge transfer excitons, which allows much more efficient dissociation of the pair. [10] Charge transfer complex based systems should have much lower optical gap energies, with values of between 0.5 and 2 eV, accessible by tuning the constituent molecules and

stoichiometry (as with ambipolar transport properties). [104] As with FETs it should be possible to tune the properties of charge transfer based OPCs as the hole and electron photocurrents and diffusion length are directly proportional to the charge transfer energy gap. [106]

2.2.1 Theory of Charge Transfer Complexes

The charge transfer interaction cannot be regarded either as simply ionic or covalent and it is most commonly modelled using a molecular orbital based approach in which each member of the charge transfer can be treated as an atom, and the overall complex as a molecule. [8] The band structure of the resultant charge transfer complex is derived from, but different to, the parent compounds, with the HOMO energy level of the complex close to and corresponding to the HOMO of the donor, while the LUMO corresponds to that of the acceptor. Figure 2-1 is a simplified energy scheme for the isolated donor, acceptor and CT complex (in this case tetracene-TCNQ).

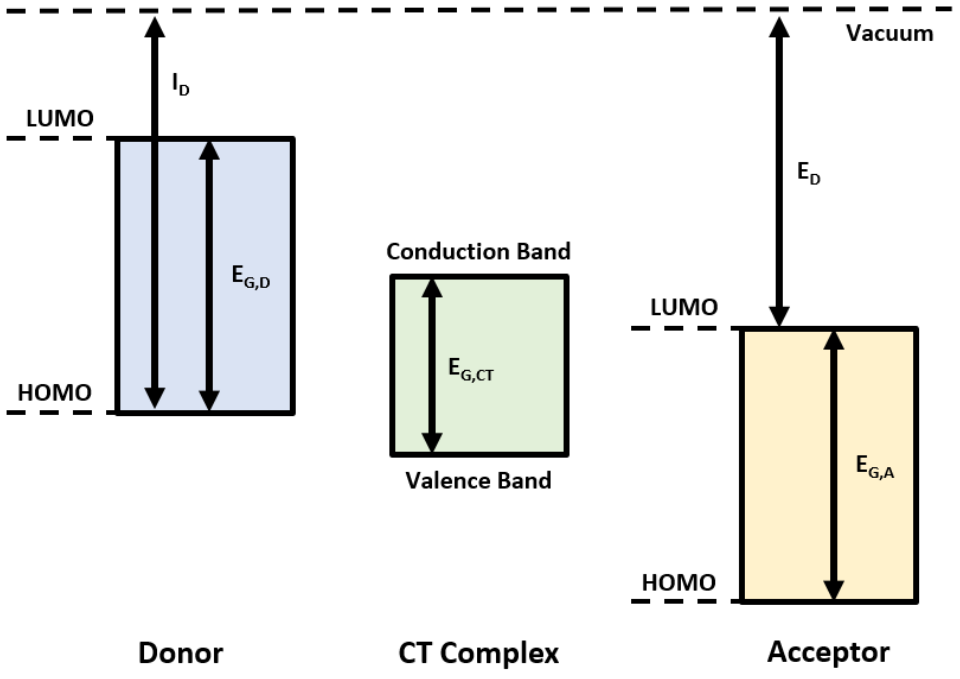

Figure 2-1: *The donor band structure (blue), acceptor band structure (yellow), and an approximation of the CT band structure (green).*

2.2.2 The Valance Bond Method

It is possible to examine the mechanics of charge transfer complexes using a valence bond (or resonance) based approach or by applying a Linear Combination of Atomic Orbitals (LCAO) based technique. Both methods have been proved to be equivalent, although the resonance based method is generally considered preferable except in the case of very strongly charged complexes in the singlet state. For the ground state both approaches are comparable, although the molecular orbital method is often more computationally tractable. [8]

Considering first a simple dimer system, comprising of a donor molecule, D, and the acceptor, A, and applying the valence bond approach as outlined by Mulliken [73, 74, 75, 76] and reported in a review by Bender, [8] the total wavefunctions of the system (to a first order approximation) can be treated as the linear combination of two states, a non-ionic pair, $\Psi_0(D, A)$, which can also include additional polarization effects, and an ionic pair, $\Psi_1(D^+A^-)$, which describes the first order dative covalent bonding interaction (a covalent bond where both bonding electrons derive from the same atom). A more complex representation should also include higher order terms (such as $D^{2+}A^{2-}$ etc.), but this is not necessary to understand the important features of the system. The overall ground state is thus:

$$\Psi_N(DA) = a\psi_0(D, A) + b\psi_1(D^+A^-). \tag{2.1}$$

Likewise, the excited (or virtual) state can be written using the same basis functions as:

$$\Psi_V(DA) = c\psi_0(D, A) + d\psi_1(D^+A^-), \tag{2.2}$$

where a, b, c and d are constants which can be found by imposing orthonormality conditions.

$$\langle\Psi_N|\Psi_N\rangle = 1 = a^2 + b^2 + ab\,\langle\psi_1|\psi_0\rangle + ab\,\langle\psi_0|\psi_1\rangle\,, \tag{2.3}$$

$$\langle\Psi_V|\Psi_V\rangle = 1 = c^2 + d^2 + cd\,\langle\psi_1|\psi_0\rangle + cd\,\langle\psi_0|\psi_1\rangle\,, \tag{2.4}$$

$$\langle\Psi_N|\Psi_V\rangle = 0 = ac + bd + ac\,\langle\psi_1|\psi_0\rangle + bd\,\langle\psi_0|\psi_1\rangle\,. \tag{2.5}$$

From 2.5 it can be shown that $ac = -bd$. This means that if the ground state is predominately non-ionic (i.e. $\psi_N \approx \psi_0(D, A)$ with $a \gg b$) then the excited state will be ionic as $d > c$, and vice versa. Therefore during excitation the character of

the complex changes and hence the excitation process is associated with a transfer of charge from the donor to the acceptor.

From this analysis it is also possible to derive a relationship between the CT band and the ionisation potential of the donor (ID) and the electron affinity of the acceptor (EA).

The energy difference between the ground and first excited state can be found by substituting the trial wavefunction $\Psi_N(DA) = a\psi_0(D, A) + b\psi_1(D^+A^-)$ into the Schrödinger Equation and applying the variational principle, which assumes that the real energy of a system will always be greater than the calculated value and can thus be obtained by minimising energy with respect to the coefficients a and b. Thus:

$$\frac{\partial E}{\partial a} = \frac{\partial E}{\partial b} = 0, \tag{2.6}$$

where E is energy, to yield the secular equations:

$$\begin{vmatrix} E_0 - E & H_{01}ES_{S1} \\ H_{01} - ES_{01} & E_1E \end{vmatrix} = 0, \tag{2.7}$$

where H_{01} is the resonance integral $\langle\psi_0|\hat{H}|\psi\rangle$, S_{01} is the overlap integral $\langle\psi_0|\psi_1\rangle$. E_0 is equal to the sum of the separate energies of A and D, modified to include attractive interactions due to ionic, ionic-dipole, dipole-dipole, hydrogen bonding, London dispersion forces and any repulsive effects due to exchange interactions. E_1 is a similar term to E_0, but also includes energy due to ionic and covalent bonding. $\hat{H}$ is the Hamiltonian.

This expression yields a quadratic equation, the roots of which correspond to the energies of the ground and excited state, E_n and E_v.

$$E_n \approx E_0 - \frac{(H_{01} - S_{01}E_1)^2}{E_1 - E_0}, \tag{2.8}$$

$$E_v \approx E_1 - \frac{(H_{01} - S_{01}E_1)^2}{E_1 - E_0}. \tag{2.9}$$

We can define the charge transfer energy, hv as:

$$hv = E_v - E_0, \tag{2.10}$$

and thus:

$$hv_{ct} = E_1 - E_0 - \frac{(H_{01} - S_{01}E_0)^2 - (H_{01} - S_{01}E_1)^2}{E_1 - E_0}. \tag{2.11}$$

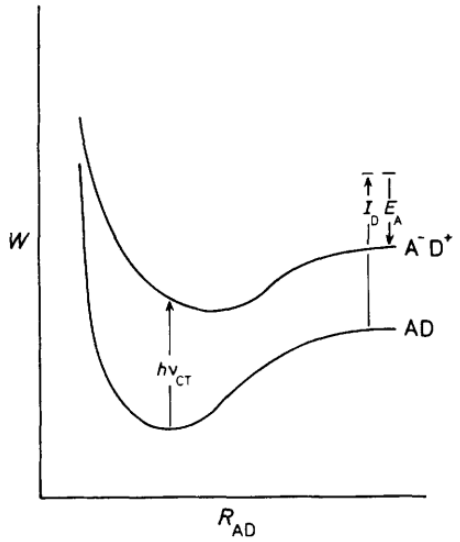

Figure 2-2: *Potential energy surface representation of the charge energy transition and its dependence on ID and EA. Figure adapted from Bender. [8]*

It is possible to re-write this equation in terms of the ionisation energy, I_D, and electron affinity, E_A, at infinite separation, plus a correcting term (Figure 2-2). The ground state can be expressed as $E_0 = E_\infty - G$, where, E_∞ is the vacuum energy. The excited state is $E_1 = E_\infty + I_D - E_A + G'$. Mulliken suggests that G can be interpreted as a non-bonding stabilisation term, primarily due to London dispersion forces and that G' also includes Columbic and exchange interactions due to the nature of the excited state. [75]

This charge transfer energy, which corresponds to the absoption energy for CT transitions, is thus:

$$h\nu_{ct} = I_A + E_A + G + G' + \frac{(H_{01} - S_{01}E_1)^2}{E_1 - E_0}. \tag{2.12}$$

It is therefore possible to vary the charge transfer properties by modifying the electron affinity and ionisation potential of the constituent molecules. [31]

2.2.3 Linear Combination of Atomic Orbitals Based Method

By contrast the LCAO based approach assigns the electrons involved in the charge transfer to a delocalised orbital (or orbitals in the case of multiple charge transfer effects) spread across the nuclei of both molecules, and charge transfer is simply an

excitation from this occupied delocalised orbital to a virtual molecular orbital.

For larger multi-molecule complexes it is important to take into account the effects of long range Columbic interactions, which obviously do not appear with dimers. McConnell *et al.* [70] apply the same reasoning as before to a three dimensional crystal formed from stacks of alternating donor acceptor molecules. Once again disregarding any higher order ionisation terms (i.e. only considering charge states of -1, 0 or +1) yields a matrix where the diagonal elements depend on the ionization potential of the donor, and electron affinity of the acceptor, as well as Coulomb interactions between ion molecules.

The largest off-diagonal elements are the Mulliken resonance integrals (analogous to those derived before):

$$\gamma = \langle ...DA...|\hat{H}|...D^{+}A^{-}...\rangle \,. \tag{2.13}$$

Provided these contributions are small, we can apply perturbation theory, [61] yielding an energy of:

$$E = N(\epsilon_0\rho - \epsilon_1\rho^2), \tag{2.14}$$

where N is the total number of molecules in the crystal stack, ρ is the average charge density per molecule (this can also be thought of as the degree of charge transfer, ranging from 0 to 1), $N\epsilon_0$ refers to the total energy required to transfer one unit of charge from each acceptor to each donor molecule, disregarding Coulomb interactions between molecules (i.e. $\epsilon_0 = \frac{1}{2}(I_D - E_A)$), and $-N\epsilon_1 1\rho^2$ corresponds to the Madelung energy of the system, with $2\epsilon_1$ being the energy required to remove an ion (either D^+ or A^-) from a fully ionic lattice.

Based on the above arguments, the energy of the system is minimised for either $\rho = 0$ or $\rho = 1$, meaning we should expect to see two clearly distinct types of complex, those with fully neutral ground states, and those with fully ionic states. While this holds true for low temperatures, in real systems it is typically not the case. Although the value of ρ will usually lie close to one of these two extremes, there will still be some degree of partial charge transfer. This follows from a more rigorous phenomenological examination by Strebel *et al.*, [98] which takes into account contributions due to electrical and magnetic excitations and leads to a greater overlap between neighbouring molecules.

We can thus delineate two broad classes of charge transfer complexes. A "neutral"

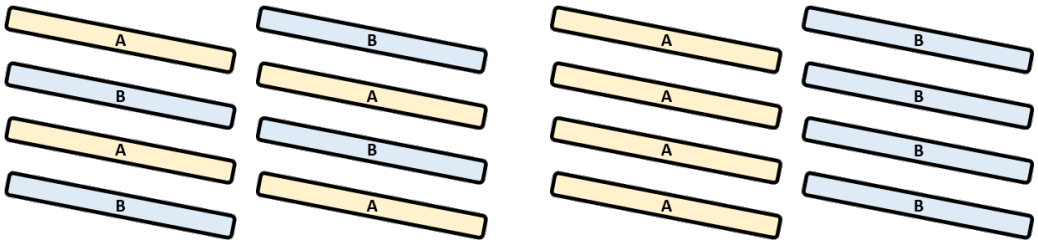

(a) *Mixed stacks* ***(b)*** *Segregated stacks*

Figure 2-3: *Crystalline packing of 1:1 charge transfer complexes.*

complex is defined by $\rho < 0.5$ and will occur when $\epsilon_0 < \epsilon_1$, meaning that the Madelung energy of the crystal is significantly greater than $I_D - E_A$. If the reverse is true and the Madelung energy is significantly less, the complex can be classified as "ionic", with $\rho > 0.5$. [31]

2.2.4 Structure

So far we have considered the most basic charge complex arrangement, a 1:1 mixed stack stoichiometry; however a range of alternate configurations is possible, although these are generally rarer.

TTF-TCNQ, for example, forms what is known as a segregated stack geometry, which consists of adjacent ...AAAA... and ...DDDD... stacks. (Figure 2-3) Other ratios, such as 1:2 or 3:2 are also possible and in these cases the extra molecules either exist within the stack (such as DDADDA) or in the interstitial space between them. In the latter case these molecules do not necessarily directly contribute to the charge transfer process, but can nevertheless have an effect on the properties of the system due to the modification of the lattice arrangement compared to the more basic mixed and segregated stack structures.

For example, the degree of axial tilt between molecules with respect to the stacking axis is correlated to the coupling between their molecular orbitals and hence the degree of charge transfer can be altered by binding electrostatic interactions with these extra molecules.

One might assume that for aromatic $\pi - \pi$ interactions it would be energetically favourable if the molecules are perfectly aligned on top of each other within a given stack, in what is known as a sandwich or co-facial parallel stacked geometry (Figure 2-4a). In fact, in most molecular systems this is not the case. More commonly, the molecules in

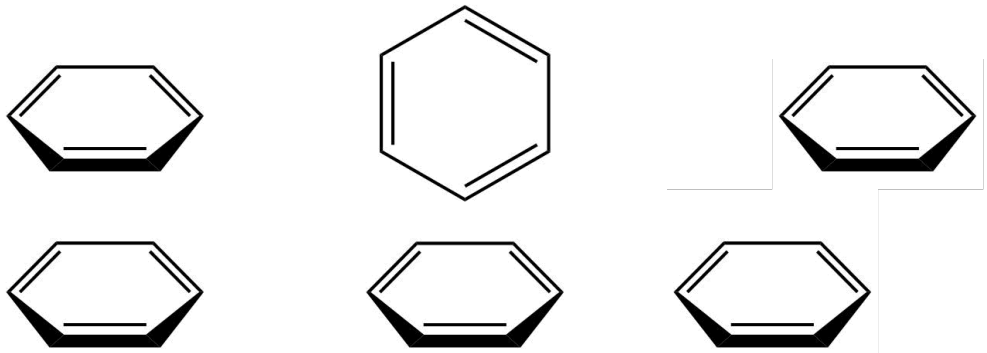

(a) *Sandwich or cofacial parallel stacked configuration* ***(b)*** *Edge to face T configuration* ***(c)*** *Parallel displaced configuration*

Figure 2-4: *The three most common stacking configurations for aromatic systems.*

a stack are arranged in an edge-to-face "T" configuration, where alternating molecules within a stack are perpendicular to one another, (Figure 2-4b) or a parallel displaced configuration, where alternating molecules are offset from one another, sometimes by as much as one molecular ring in distance. (Figure 2-4c) [94] Generally for small un-substituted aromatic compounds the T configuration is favourable, whereas larger multi-ring molecules or substituted molecules tend to demonstrate a parallel displaced geometry. [102] Examples of this can be seen in Chapter 4 in the structures of the various charge transfer complexes.

2.2.5 Excitations

For a neutral complex the lowest energy excitation is expected to be triplet excitons corresponding to a bound pair of parallel spins propagating through the crystal lattice. [70] The triplet state is typically lower energy than the corresponding singlet state as it includes exchange interaction.

$$...ADAD^{+} \uparrow A^{-} \uparrow DADA... \tag{2.15}$$

The excitation energy is $2\epsilon_0 - \epsilon_1'$, where ϵ_1' is the Coulomb interaction between the ion pair (excitation energy is ϵ_0 per ion).

The energy required to produce a charge carrying excitation, which would consist of electrons propagating through acceptor molecules, and holes through donors, is simply equal to ϵ_0 per ion with a band width of γ^2/ϵ_2, where ϵ_2 is the energy required to create an ion pair next to a pre-existing ion in an otherwise neutral chain. γ refers to the

resonance integral as defined in equation 2.13. In general this energy is of the order of electron volts and is therefore most readily accessible through optical excitation.

For ionic complexes, the lowest energy excitations are instead linear spin waves. These are the spin excitations of a linear chain of spin $\frac{1}{2}$ molecules corresponding to the Hamiltonian

$$H = \sum_i JS_i \cdot S_{i+1}, \tag{2.16}$$

where

$$J = \frac{4\gamma^2}{4\epsilon_1 - 2\epsilon_0 - \epsilon_1'}. \tag{2.17}$$

Here the excitation energy per charge carrier is $2\epsilon_1 - \epsilon_0$ with a band width of γ^2/ϵ_3, where ϵ_3 is the energy required to create two neutral molecules next to a pre-existing neutral molecule within the chain. [70]

2.3 Metallic Behaviour

A large proportion of CT complexes are insulating or, at best, act as semiconductors. However, segregated stack complexes can display a high degree of anisotropic conductivity and even metallic behaviour along the direction of the stacks. The quintessential example of such a complex is TTF-TCNQ, which should now be familiar, and this complex will be referred to extensively in the proceeding sections as it has been extensively studied and its behaviour is typical of other similar systems.

This conductivity occurs due to the fact that there is considerable π-orbital overlap between the molecules in a given stack. Due to the CT interaction these orbitals are only partially filled, and this results in a high degree of delocalisation as the electrons can travel freely up and down the chain in what can be described as a one dimensional conduction band. This band can be treated a one dimensional as the interactions between neighbouring molecules within a stack are considerably stronger than any inter-stack interactions. In the case of TFF-TCNQ even the largest inter-chain coupling is one sixtieth the strength of the intra-chain ones. [9]

This one dimensional behaviour cannot be adequately explained by conventional metallic conduction models. Not only are these conduction bands extremely narrow, on the order of 0.2 to 0.5 eV [91], the conductivity demonstrates a strong and distinctive tem-

perature dependence. Starting at high temperatures, conductivity will rapidly increase as temperature lowers until it reaches a maximum. With TTF-TCNQ, resistivity (equal to $1/\sigma$) increases with $1/T^2$ in this high temperature region, compared to 1/T behaviour which occurs in normal metals due to phonon scattering. [25] In some systems this relationship can be as high as $1/T^4$. [91] Beyond the maximum further lowering will cause an even more rapid drop in conductivity, and in most cases the material becomes a semiconductor or even an insulator. [91]

The number of charge carriers remains constant (ρ does not change significantly), so this behaviour must be caused by a change in mobility. In part, this mobility change is caused by lattice contraction, particularly along the stacking direction, as temperatures decrease. However, the primary cause is a reduction in phonon-charge carrier interactions as temperature is reduced. The sudden transition to an insulating or semi-conducting phase is due to the presence of what is known as Peierls transition.

2.4 Electronic-Peierls Transition

As first shown by Peierls, an equally spaced one dimensional chain is fundamentally unstable at low temperatures, and it will undergo a lattice distortion (known as a Peierls transition, or Peierls distortion). Neighbouring molecules will be displaced in opposite directions by an equal amount, causing them to dimerise. This lattice distortion results in spatially periodic modulation of electron density known as a charge-density wave. This wave can potentially travel freely along the one dimensional chain through phonon coupling, resulting in conductive behaviour. Here we follow the derivation reported by Schwoerer & Wolf. [91]

It is important to note that the transition should more accurately be referred to as an Electronic Peierls transition, as there is also an analogous, although less common, spin based magneto-elastic transition that can occur in charge transfer complexes. This is covered in Section 2.5.

2.4.1 Theory

We first consider a one dimensional free electron system of length L and derive several key characteristics. The energy of the free electrons will be equal to:

$$E(k) = \frac{\hbar^2}{2m}k^2, \tag{2.18}$$

where $\hbar$ is the Reduced Planck's constant, m is the mass and k is the wavevector, equal to:

$$k = \pm l\frac{2\pi}{L}, l = 0, 1, 2... \tag{2.19}$$

As each state can be occupied by two electrons with opposing spins, the density of states in reciprocal space is simply:

$$D(k) = 2\frac{L}{2\pi} = \frac{L}{\pi}. \tag{2.20}$$

For T=0 all states up to the Fermi level, E_f, will be filled and these will have wavevectors $\pm k_f$. For all finite temperatures, some electrons will occupy higher energy states, which the occupation probability for a given state with energy E given by the Fermi distribution function:

$$f(E) = \frac{1}{e^{(E-E_f)/k_bT} + 1}. \tag{2.21}$$

The total number of electrons, N, must satisfy the condition:

$$\int_0^\infty F(E)D(E)dE, \tag{2.22}$$

where D(E) is the density of states. For T=0 all states above the Fermi energy are unfilled, so this must be equal to:

$$\int_0^{E_f} F(E)D(E)dE. \tag{2.23}$$

The density of states can then be determined by substitution (using equations 2.18 and 2.20) to be equal to:

$$D(E) = \frac{\sqrt{2m}L}{\pi\hbar}\frac{1}{\sqrt{E}}, \tag{2.24}$$

with the Fermi energy equal to:

$$E(f) = \frac{\pi^2 \hbar^2}{8m} n^2, \tag{2.25}$$

where n is the electron number density, equal to N/L. The Fermi wavevector will then be equal to

$$K(f) = \frac{\pi}{2} n. \tag{2.26}$$

Next we consider a chain of atoms. This can modelled by applying a periodic one dimensional potential with spatial period a_M and amplitude V. This will lead to the formation of Brillouin Zones, with the first extending between $q = \pm\frac{\pi}{a_M}$. If V is weak, it will lead to band gap at the boundary of the first Brillouin Zone equal to 2V.

If there are two electrons per unit cell then $n = 2/a_m$ and $k_f = \pm\frac{\pi}{a_M}$. Therefore the band will be filled and the system will act as an insulator. If there are fewer electrons the band will only be partially filled (as would be the case in a CT system with partial ρ) and the system will be metallic.

For two dimensional and three dimensional systems, phonons with any wavevector can contribute to scattering processes. However, for a one dimensional system, the phonon mediated relaxation of electrons is only possible if the electron goes from having a wavevector of $+k_f$ to $-k_f$, or vice versa. This is because phonon energy is always small, and so scattering processes that occur close to the Fermi surface are allowed. In a one dimensional system, the Fermi surface only consists of two points at $\pm k_f$. Hence, only photons where $q = 2k_f$ can be involved with scattering processes in order for both conservation of momentum (wavevector) and energy to be fulfilled.

The Peierls transition occurs due to instability in the periodic lattice potential caused by these phonons. By applying a modulation of $2k_f$ this leads to a band gap at the Fermi level. This results in a lowering in the energy of the states just below the Fermi level, and increasing the energy for the states above it. For a one dimensional metal where only the states $k \leq k_f$ are occupied, this leads to an overall reduction in energy. (Figure 2-5) Of course, the lattice distortion itself has an energy cost, so there is in fact only a net energy saving at low temperatures. Above a critical temperature, known as the Peierls temperature, the energy gap closes as the Peierls distortion is quenched by phonons.

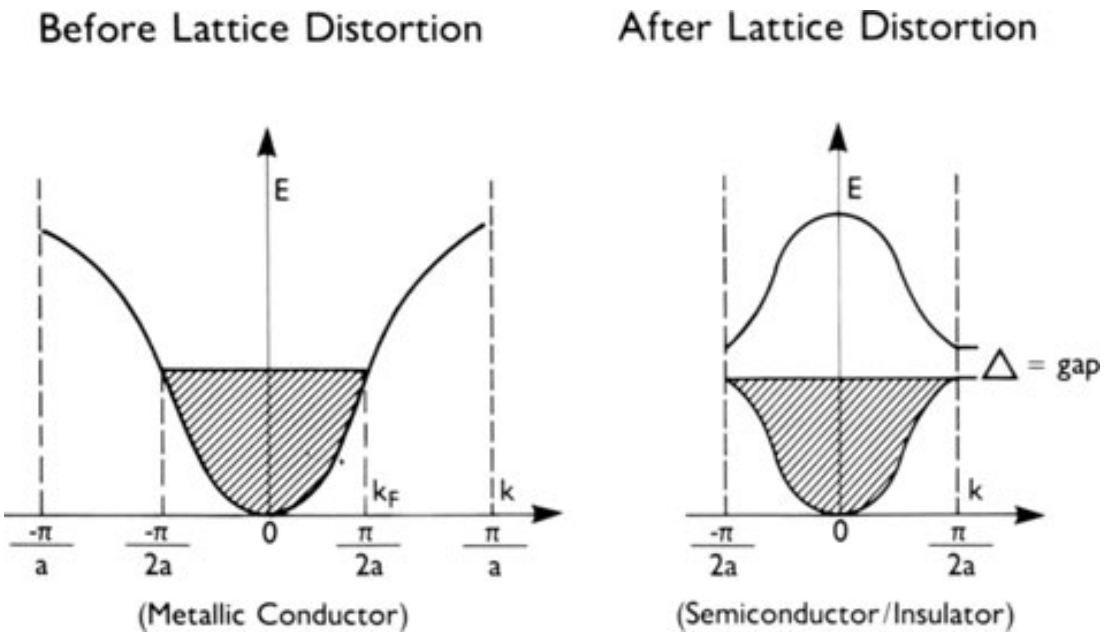

Figure 2-5: *A representation of the electronic-Peierls transition, showing the energy dispersion E(k) for a uniform band filled up to the Fermi level, and for a dimerised chain. Figure adapted from James W. Bray* et al. *[12]*

2.5 Spin-Peierls Transition

Spin-Peierls (SP) transitions are a type of magneto-elastic transition that can occur in quasi one dimensional insulators. Indeed, it has been claimed that both the electronic-Peierls transition and the spin-Peierls transition are both specific examples of a more generalised phenomenon. SP transitions were first discovered experimentally in 1975 in TTF-TCNQ. [11] Here we primarily follow the derivation by James W. Bray *et al.* [12]

Most magnetic systems demonstrate long range ordering (typically ferromagnetic or anti-ferromagnetic) beyond a critical transition point. For an ideal one dimensional system this transition temperature can only occur at T = 0. For real systems weak inter-chain interactions raise this transition temperature. This magnetic ordering is for a rigid lattice, if, as before, we allow for the possibility of elastic distortions, then a new type of ordering is possible. Notably, unlike the electronic-Peierls transition, SP systems remain insulating at all temperatures.

2.5.1 Theory

We consider an array of one dimensional antiferromagnetic (AF) spin chains described by a spin $\frac{1}{2}$ Heisenberg Hamiltonian. We will only consider nearest neighbour interactions, and inter-chain magnetic coupling will be neglected. We are considering phonon interactions. This can be written as

$$\mathbf{H} = \sum_{j} \mathbf{J}(j, j+1)(\mathbf{S}_j \cdot \mathbf{S}_{j+1}) + \sum_{\mathbf{q},\alpha} \omega_0(\mathbf{q}, \alpha) b^{\dagger}_{q\alpha} b_{q\alpha}, \tag{2.27}$$

for lattice sites up to j, where $\mathbf{J}(j, j+1)$ is the exchange energy as a function of the separation between the two sites j and $j+1$, $\mathbf{S}$ is the spin vector, ω_0 is the unrenormalised phonon energy and $b^{\dagger}_{q\alpha}$ and $b_{q\alpha}$ are the creation and destruction operators for the three dimensional phonons with wave vector $\mathbf{q}$ on branch α, respectively.

Thus we have a one dimensional magnetic system coupled to a three dimensional phonon system. The overall system can therefore be described as quasi-one dimensional.

For a one dimensional AF Heisenberg chain quantum zero-point fluctuations will populate low lying excited states as the excited state is degenerate with the ground state for $q = 0, \pm\frac{\pi}{a}$. As a result, both the singlet ground state and triplet excited states will be populated. If the chain is dimerised, a gap opens up in the excitation spectrum, raising the energy of the excited states, and meaning they can no longer be populated, lowering the net magnetic energy. This is also the case for an XY AF chain; however it is not the case for the Ising model, where the spin vectors can only occupy two states (+1 or -1), or classical AF chains. In the case of the former, there is already an energy gap between the ground and excited state, and in the case of the latter, there is no zero-point energy. Further, because quantum fluctuations decrease rapidly for $|\mathbf{S}| > \frac{1}{2}$ high spin materials will also not demonstrate an SP transition.

Unfortunately, this Hamiltonian cannot be solved exactly, and so approximations must be made. One method is to apply the Jordan-Wigner transformation, which maps the spin operations onto Fermion creation and annihilation operators, and then simplify the spin-phonon coupling term by only considering first order inter-site spacing terms.

Applying the Jordan-Wigner transformation, one defines

$$\Psi_j = (-2)^{j-1} S_1^z S_2^z ... S_j^-, \tag{2.28}$$

where $S^{\pm} = S^x \pm iS^y$ and $S_j^z = \frac{1}{2}\Psi_j^\dagger \Psi_j$. Substituting this into Equation 2.27 gives

$$\mathbf{H} = \sum_j \mathbf{J}(j, j+1)\frac{1}{2}(\mathbf{\Psi}_j^\dagger \mathbf{\Psi}_{j+1} + \mathbf{\Psi}_{j+1}^\dagger \mathbf{\Psi}_j - 2\mathbf{\Psi}_j^\dagger \mathbf{\Psi}_j \mathbf{\Psi}_{j+1}^\dagger + \frac{1}{2}) + \sum_{\mathbf{q},\alpha} \omega_0(\mathbf{q}, \alpha) b_{q\alpha}^\dagger b_{q\alpha}. \tag{2.29}$$

Next, the spin-phonon coupling is taken as

$$\mathbf{J}(j+1) = J + \sum_j [\mathbf{u}(j) - \mathbf{u}(j+1) \cdot \nabla_j \mathbf{J}(j, j+1) + ...], \tag{2.30}$$

where $\mathbf{u}$ are the three dimensional lattice displacement operators. Taking the Fourier transform of $\mathbf{u}$ and substituting into Equation 2.29 ultimately leads to the expression

$$\begin{aligned} \mathbf{H} = & \sum \epsilon_k \mathbf{\Psi}_k^\dagger \mathbf{\Psi}_k + N^{-1} \sum_{k_1+k_2=k_3+k_4} \nu(k_2 - k_3) \mathbf{\Psi}_{k_1}^\dagger \mathbf{\Psi}_{k_2}^\dagger \mathbf{\Psi}_{k_3} \mathbf{\Psi}_{k_4} \\ & + N^{-\frac{1}{2}} \sum_{kq\alpha} g_1(k, \mathbf{q}, \alpha) \mathbf{\Psi}_k^\dagger \mathbf{\Psi}_{k-q} (b_{q\alpha} + b_{-q\alpha}^\dagger) \\ & + N^{-1} \sum_{k_1+k_2=k_3+k_4-q} g_2(k_2 - k_3, \mathbf{q}, \alpha) \mathbf{\Psi}_{k_1}^\dagger \mathbf{\Psi}_{k_2}^\dagger \mathbf{\Psi}_{k_3} \mathbf{\Psi}_{k_4} (b_{q\alpha} + b_{-q\alpha}^\dagger) \\ & + \sum_{\mathbf{q},\alpha} \omega_0(\mathbf{q}, \alpha) b_{q\alpha}^\dagger b_{q\alpha}, \end{aligned} \tag{2.31}$$

where $\epsilon_k = J(\cos(ka-1))$, N is the number of lattice sites, $v(k) = J\cos(ka)$, $g_1(k, \mathbf{q}, \alpha) = \frac{1}{2} g(\mathbf{q}, \alpha)(1-e^{-iqa})(e^{-ika}-1)(1-e^{-i(q-k)a})$, $g_2(k, \mathbf{q}, \alpha) = g(\mathbf{q}\alpha)e^{ika}(1-e^{-iqa})$, $g(\mathbf{q}, \alpha) = [2m\omega_0(\mathbf{q}\alpha)]^{-\frac{1}{2}} \mathbf{e}(\mathbf{q}, \alpha) \cdot \nabla \mathbf{J}(j, j+1)$, $\mathbf{e}(\mathbf{q}, \alpha)$ is the phonon polarisation vector and m is the mass of the magnetic lattice site.

An alternative approach is to begin with the Hamiltonian for an already dimerised AF chain. In this case the expression becomes

$$\mathbf{H} = \sum_{j=1}^{N-2} \mathbf{J}_1 \mathbf{S}_{j,1} \cdot \mathbf{S}_{j,2} + \mathbf{J}_2 \mathbf{S}_{j,1} \cdot \mathbf{S}_{j+1,2}) + \sum_{\mathbf{q},\alpha} \omega_0(\mathbf{q}, \alpha) b^\dagger_{q\alpha} b_{q\alpha}, \tag{2.32}$$

where j describes the dimer, and J_1 and J_2 represent the intra and inter-dimer exchange interactions. The subsequent treatment for this expression is essentially the same. Since both Equation 2.27 and 2.32 describe the same system, just above and below the transition temperature respectively, (at $T_c \mathbf{J}_1 = \mathbf{J} + 2 = \mathbf{J}(j, j+1)$) they should yield identical results. Unfortunately, the mean-field methods that are most commonly used lead to slightly different solutions. Which formulation is superior depends on the system and the nature of the approximations assumed.

2.5.2 Mean Field Treatments

The majority of SP treatments apply mean-field (MF) approximations. Generally, these methods work by approximating all interactions with one component, by considering the interactions between this component and a single approximate averaged interaction. [16]

In this particular case, the Hartree-Fock approximation is most commonly used. All four-fermion terms are converted to two-fermion terms:

$$\langle \mathbf{\Psi}^\dagger_k \mathbf{\Psi}_q \rangle = n_k \delta_{kq}, \tag{2.33}$$

where $n_k = \left(e^{\frac{E_k}{k_B T}} + 1 \right)^{-1}$. Here k_B is the Boltzmann Constant and $E_k \equiv p\mathbf{J} \cos(ka)$, where p is the re-normalisation factor equal to $\left(1 - 2N^{-1} \sum_k n_k \cos(ka)\right)$. For $T \ll J$ this is approximately constant, with a value of 1.64.

Equation 2.31 then becomes

$$\mathbf{H} = \sum_k E_k \mathbf{\Psi}^\dagger_k \mathbf{\Psi}_k + \sum g(\alpha, \mathbf{q}, k) \mathbf{\Psi}^\dagger_k \mathbf{\Psi}_{k-q} (b_{\alpha q} + B^\dagger_{\alpha - q}) + \sum_{\mathbf{q},\alpha} \omega_0(\mathbf{q}, \alpha) b^\dagger_{q\alpha} b_{q\alpha}, \tag{2.34}$$

where $g(\alpha, \mathbf{q}, k) \equiv ipg(\alpha, \mathbf{q}) \Big[\sin(ka) - \sin\left(\{k-q\}a\right) \Big]$. This equation is, in turn, most commonly solved by applying yet another MF approximation, known as the random

phase approximation (RPA), to the fermion-phonon coupling term.

This gives an expression for the re-normalised phonon frequency ω:

$$\omega^2 = \omega_0^2(\alpha, \mathbf{q}) + N^{-1} \sum g(\alpha, \mathbf{q}, k) \frac{g(\alpha, \mathbf{q}, k-q) n_k - g^*(\alpha, \mathbf{q}, k) n_{k-q}}{\omega - E_{k-q} + E_k}. \tag{2.35}$$

From this, it can be shown that $q = \frac{\pi}{a}$ and that near the transition temperature T_c

$$\omega^2 = \frac{\omega_0^2(\frac{T}{T_c} - 1)}{\ln(\frac{0.83pJ}{T_c})}, \tag{2.36}$$

and at the transition temperature itself $\omega(q = 2k_F) = 0$, where k_F is the Fermi wave vector, equal to $\frac{\pi}{2a}$. This leads to a gap equation equal to

$$\omega_0^2(\mathbf{q}, q = 2k_F) = \frac{g^2}{J^2} \frac{2}{\pi} \int_{-J_p}^{J_p} dE \frac{[(Jp)^2 - W^2]^{1/2}}{E} \tanh\left(\frac{1}{2}\beta_c E\right), \tag{2.37}$$

where $g \equiv g(\alpha, \mathbf{q}, q = 2k_f)$ and $\omega_0 \equiv \omega_0(\alpha, \mathbf{q}, q = 2k_f)$. Assuming that coupling is weak $T_c \ll J$ then the transition temperature is:

$$T_c = 0.83pJ \exp\left(\frac{-1}{\lambda}\right), \tag{2.38}$$

where $\lambda = \frac{4g^2 p}{\omega_0^2 \pi J}$ and $\Delta(T)$, the magnetic gap is

$$\Delta(T = 0) \equiv \Delta(0) = 1.754 T_c. \tag{2.39}$$

As expected, below T_c the lattice is dimerised, and the two values of J (c.f. equation 2.32) are

$$J_{1,2} \equiv J(1 \pm \delta(T)), \tag{2.40}$$

with the dimerisation parameter, $\delta(T)$, equal to $\frac{\Delta(T)}{pJ}$.

2.5.3 Alternative Treatments

As should be clear at this juncture, this result is based on a series of approximations that may not necessarily be valid for the system in question. This is particularly the case if there is any lattice anisotropy or strong spin-lattice coupling. As previously mentioned, starting from Equation 2.32 leads to slightly different solutions. No analytical expression is possible for the Heisenberg case, although for the XY case the transition temperature is

$$T_c = 0.83J \exp \lambda', \tag{2.41}$$

where $\lambda' \equiv \frac{4p}{\lambda}$. The magnetic gap is

$$\delta(T=0) = J\delta(0)\left(1 + \frac{4\ln(2)}{\pi} - \frac{2\ln(\delta)}{\pi}\right). \tag{2.42}$$

An alternative approach has been demonstrated by Cross and Fisher, which uses a boson algebra to avoid the HF approximation, although it does still use the RPA approximation for the spin-phonon coupling term and the weak-coupling approximation. [21] Applying this approach obtains a critical temperature of

$$T_c = 0.8J\lambda'', \tag{2.43}$$

where $\lambda'' \equiv \frac{\lambda}{p}$. They also find an increase in the rate of phonon softening (discussed in more detail in Subsection 2.5.4) above the transition temperature as

$$\omega^2(2k_F, T) = \omega_0^2\left(\frac{T}{T_c} - 1\right). \tag{2.44}$$

2.5.4 High Temperature Behaviour

The majority of materials that demonstrate a SP transition have also demonstrated distinctive high temperature behaviour in the form of phonon softening. The collective movement of atoms in a crystal lattice to transform it from a higher-symmetry structure into a lower-symmetry structure can be described in terms that are known as soft phonon modes. This phase transition is heralded by a reduction in the frequency of the soft phonon. [88]

In the case of these materials, at high temperatures the frequency of the phonon corresponding to the dimerization wave vector is reduced to about an order of magnitude below its normal value prior to a structural transition. This has been reported in tetrathiafulvalene copper-benzenedithiol (TTF-CuBDT), tetrathiafulvalene gold-benzenedithiol (TTF-AuBDT), N-methyl-N-ethylmorpholinium tetracyanoquinodimethane (MEM-$(TCNQ)_2$). [11, 46, 99]. This soft phonon mode also has the effect of slightly raising the temperature of the SP transition, as it enhances spin-phonon coupling.

Chapter 3

Experimental Methods

3.1 Introduction

In this chapter we review the various experimental techniques used in this work. We explore their theoretical underpinnings, their prior use in the field and the various strengths and weaknesses of each.

We first examine the range of techniques that can be used to grow CT complexes. We begin by exploring several techniques used for the pre-growth purification of the starting materials, including zone refinement and sublimation. We then look at several solution-based techniques. There are a large number of possible gas-based methods, but here we focus exclusively on physical vapour transport, the technique that was predominately used in this work. Finally, for completeness, we briefly comment on melt based growth techniques.

We next address the various ways of estimating the degree of charge transfer, ρ. We examine bond length based methods, including the Kistenmacher and HOSE methods, as well as spectroscopic methods, including IR, Raman and reflectance spectroscopy.

Finally, we consider three other analytic techniques used in this work. The first is Differential Scanning Calorimetry (DSC), which can be used to provide information on any endothermic or exothermic processes or changes in heat capacity. The second is X-ray crystallography, which is used to obtain structural information and unit cell determination. The third is Electron Paramagnetic Resonance, which is analogous to Nuclear Magnetic Resonance, and detects the transitions of unpaired electrons in an applied magnetic field rather than nuclear transitions.

3.2 Crystal Growth

One of the important requirements for reliable and accurate spectral data is the creation of sufficiently large single crystal samples, hence, proper crystal growth methods are vital. Charge transfer complexes can either be grown from melt, liquid or gas phase and in this section we examine several of the most commonly used techniques and methods for pre-growth purification of the materials.

3.2.1 Pregrowth Purification

Commercially available chemicals often have a purity in the range of 95-98%. The impurities are generally formed as a by-product of the, often multistep, chemical synthesis and can include unreacted reagents, the product of side-reactions or the product of decomposition processes. Further impurities can be produced during storage due to decomposition, or photoinduced reactions. Naturally these impurities need be removed prior to crystal growth, with the two main methods for this being zone refinement and sublimation. [58]

Zone Refinement

Zone refinement [83] is suitable for any material that can be melted without decomposition. However, as it requires large quantities (on the gram scale) and specialised non-commercial equipment, it is not commonly used for research purposes.

For zone refinement, a long ingot of the material to be purified is inserted into a tube furnace, held either vertically or horizontally, and under inert atmosphere, to prevent any unwanted reactions. One section of the ingot is then heated until it becomes molten; the heating zone is then slowly moved along the ingot (either with a fixed ingot and movable heater, or vice versa) so that the purified material melts at one end of the heating zone and crystallizes at the other (Figure 3-1).

Depending on the relative solubility of the impurities in the melt compared to the crystal, they will either accumulate at the molten interface or the crystallisation interface. By repeating this process several hundred times, this will eventually lead to the accumulation of pure material at the centre, with impurities at the ends, and this process can be further accelerated by having multiple heating zones along the length of the ingot.

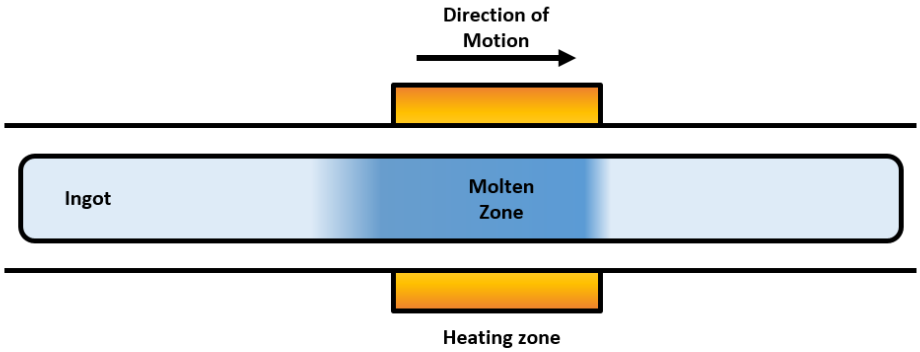

Figure 3-1: *The zone refinement process. In this configuration the heating element moves across a fixed ingot. As the heating element moves to the right, the material melts on the right of the molten zone, and crystallises on the left.*

Sublimation

There are a range of experimental techniques that can be used to purify materials through sublimation, but all of them are based on the same fundamental principles. The material to be purified is placed in a vacuum and then heated until it sublimes and is transported to a cooler deposition zone, where purified material is collected. An example is shown in Figure 3-2.

Volatile molecules, such as solvents, will simply evaporate into the vacuum and be removed, while heavier molecules will not sublime and will therefore remain in the source material zone. While vacuum sublimation is generally very efficient, and often faster than zone refinement, it is not necessarily selective.

Organic molecules in the condensed phase are typically bound together by weak intramolecular bonds. As such molecules with similar molecular mass also tend to have similar volatility and enthalpies of evaporation, so they cannot be effectively separated. To compensate for this, more sophisticated techniques can be used to try and enhance the sensitivity of this method.

One such method is step sublimation. (Figure 3-3) This process is designed to fractionate the starting material by slowly moving the work tube from the furnace as the temperature is increased stepwise so that the sublimated material is deposited at a different point along the tube each time. [58]

Another approach is to introduce a carrier gas while utilising an extremely long de-

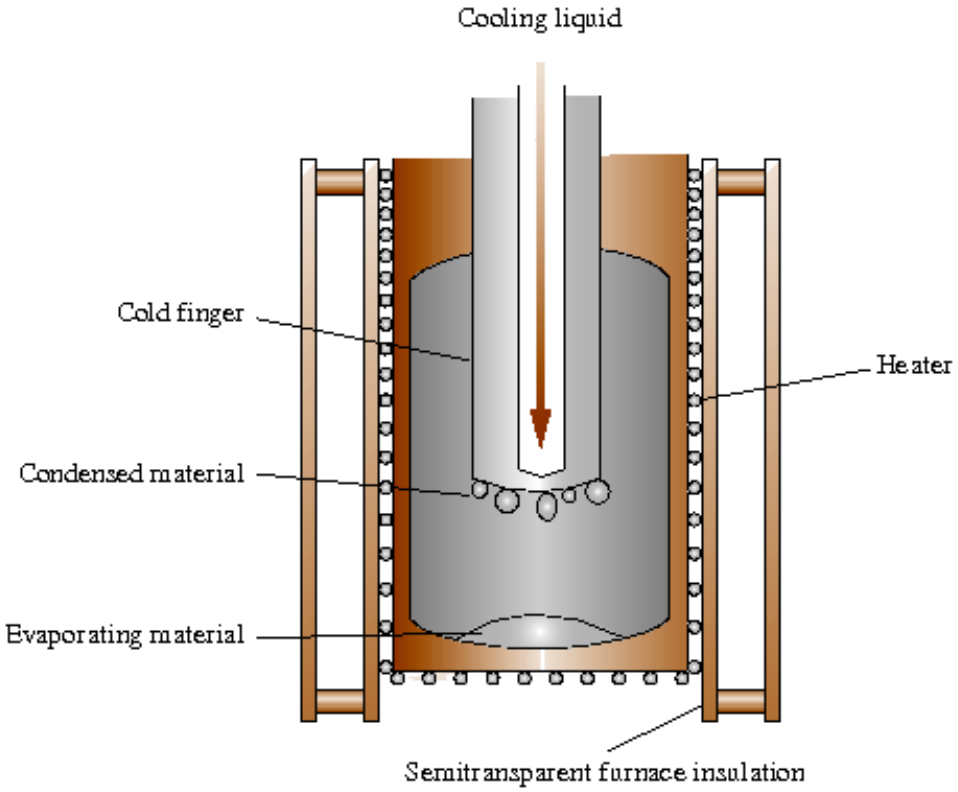

Figure 3-2: *An example of vacuum sublimation on a cold finger. Figure adapted from Kloc* et al.*[58]*

position zone and an extremely shallow temperature gradient. The distance a given molecule will be transported along the deposition zone will depend on the molecular mass, and in principle this technique is sensitive enough to separate individual structural isomers. [65, 57]

3.2.2 Liquid Phase Growth

Liquid based methods include saturation and liquid-liquid or interfacial techniques. The former, shown in Figure 3-4a involves taking a nearly saturated solution, and then letting it become supersaturated, either by cooling or by evaporation of the solvent. Regardless of the method it is important that this process is done slowly to limit the rate of nucleation, thus reducing the overall number of nucleation sites.

The more sophisticated liquid-liquid or interfacial diffusion method is shown in Figure 3-4b. This method relies on layering one solvent on top of another and ensuring that

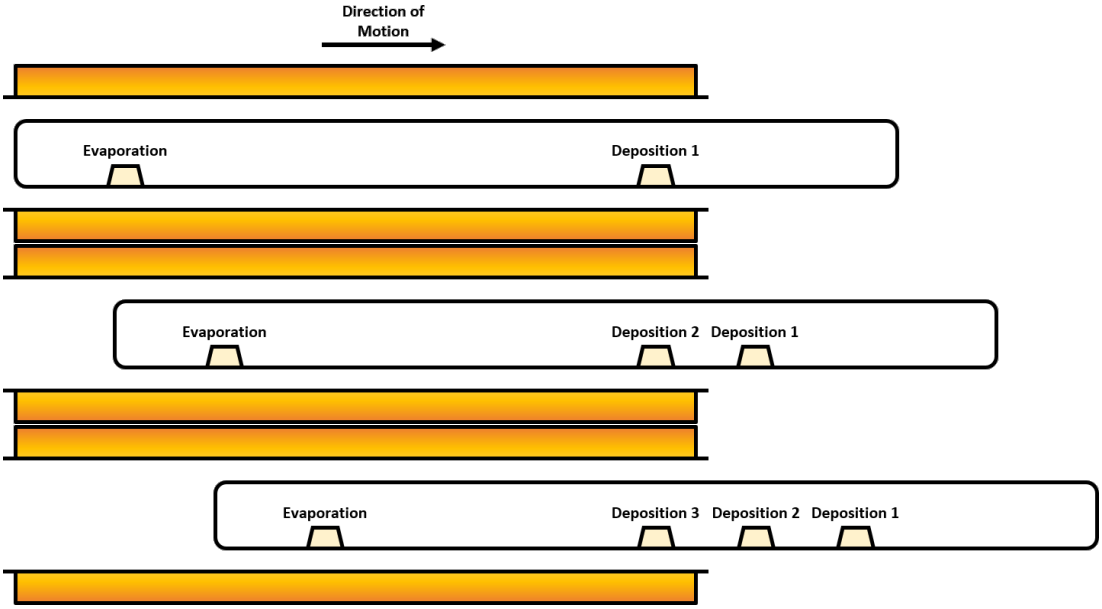

Figure 3-3: *The process of step sublimation. The work tube is pulled from the furnace so that the material is deposited at different points along the tube during each step.*

crystal growth only occurs the interface. This can be accomplished either by layering a solvent in which the starting materials can readily dissolve, over another, in which they cannot [50] or by layering a solvent in which only one material readily dissolves over another which only readily dissolves the second. [49] Over time the two solvents will mix and at this interface the solute will become increasingly insoluble until it reaches supersaturation. While slightly more difficult to set up, this has the advantage of limiting the region where nucleation can occur and thereby resulting in large crystals.

The nucleation process associated with crystal growth can be examined by considering this energy barrier via reaction kinetics. For liquid solutions, classic nucleation theory gives the rate of nucleation as: [84]

$$J_n = \Gamma\left(- \frac{B\sigma^3\Omega^2}{k_b^3 T^3 (ln(S))^2} \right), \tag{3.1}$$

where B is a shape factor, σ is the interfacial energy, Ω is the molecular volume, k_b is the Boltzmann constant, T is the temperature, and S is the supersaturation ratio, equal to the actual solution concentration divided by the equilibrium concentration. The pre-exponential factor Γ is a complex function incorporating solubility, the surface area of the nucleus and the energy barrier associated with volume diffusion of molecules

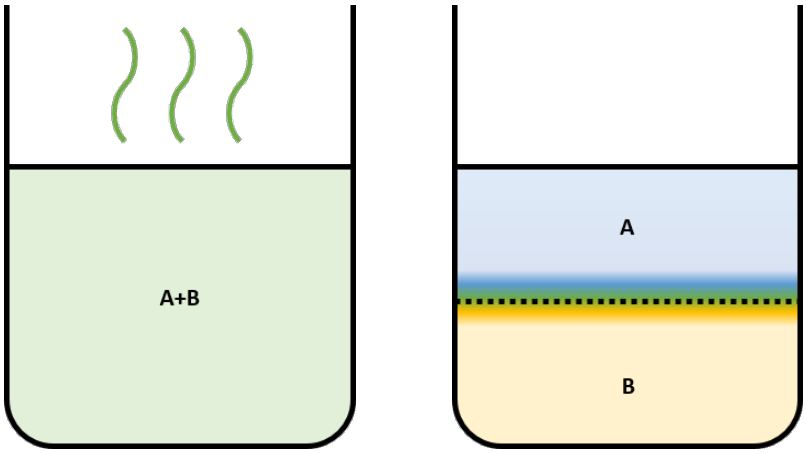

Figure 3-4: *Liquid based crystal growth methods. (a): The saturation method. Both precursors, A and B, are dissolved in a solvent, which is slowly either evaporated or cooled, causing both materials to drop out of solution and nucleate. (b): The interfacial method. Here one starting material, A, is dissolved in one solvent, which is layered above a second solvent which contains the other starting material, B. A membrane between the two layers allows intermixing at the interface and crystal growth.*

from bulk solution to the nucleus. The interfacial energy is dependent on the diffusion transport mechanism and the pre-exponential factor is dependent on the bonding interactions between surface molecules and the solvent, therefore both are strongly impacted by solvent choice.

While the free energy of the crystal phase is lower than in solution for bulk, this is not true at the surface of the crystal, as these molecules are less well bound. As such there is a critical size below which the crystals are unstable, known as the Gibbs-Tomson effect. [22] As a result of this, once nucleation sites have begun to form, additional molecules will preferentially bind to pre-existing crystallites rather than creating new sites. Thus, the crystal size distribution is easily controlled by the rate of nucleation, with a small number of nucleation sites leading to a small number of large crystals, and vice versa.

Both these methods have several disadvantages. Firstly there is risk of solvent molecules being incorporated into the final structure, [89, 113] but there is also the fact that the composition and crystal structure is heavily dependent on the choice of solvent used, and in some cases the target complex may simply be impossible or exceedingly difficult to produce. Hu *et al.* [41] reported that the final stoichiometry for Perylene-TCNQ crystal growth was dependent on the choice of solvent and not the initial stoichiometry

of the starting material. Furthermore, they reported that the 2:1 Perylene-TCNQ complex could not be grown in solution regardless of solvent choice, but could only be successfully obtained via gas phase methods. Likewise, Goetz *et al.* were unable to produce β-DBTTF-F_4TCNQ from solution. [32] Furthermore it is often not possible to grow even relatively similar CT complexes via the same solution based method, making cross-comparison difficult. For example, TCNQ dissolves in a wide range of solvents, such as dichloromethane, toluene or chloroform, but the fluorinated version, F_4TCNQ, does not.

3.2.3 Physical Vapour Transport

As with liquid based growth methods, there are a range of gas phase techniques. These can be categorised into several classes, depending whether the source material starts as a vapour or a solid which must be sublimed and whether the transport is purely physical or utilises an active catalytic chemical agent (a technique known as chemical vapour transport). [47]

Here we focus exclusively on physical vapour transport (PVT), whereby the source material is sublimated by heating and then transported to a colder region where the vapour condenses to form crystals and no active transport medium is used. These systems can either be closed, using a sealed ampoule, or open with a gas flow, as shown in Figure 3-5.

The exact transport mechanism is very complex and depends on a variety of factors. According to Brinkman and Carles [13] the fundamental driving process is the temperature difference between the source and the sink. The change in volume caused by vaporisation and condensation produces a Stefan Wind which helps transport material from source, the location of the starting material, to sink, the location of the crystal growth, by advection. Condensation then occurs at the sink due to local supersaturation as the hot vapour comes into contact with the cool crystal surface.

The dynamics of vapour flow is also important, and a factor the authors claim is often neglected in favour the temperature gradient as the sole mean of transport control. They further report that while diffusion also occurs it will generally not dominate in most systems. To make matters worse, the temperature gradient cannot even be easily estimated since any crystal growth must be highly exothermic, as it involves a considerable decrease in entropy to convert molecules in the gas phase into a highly ordered crystal structure.

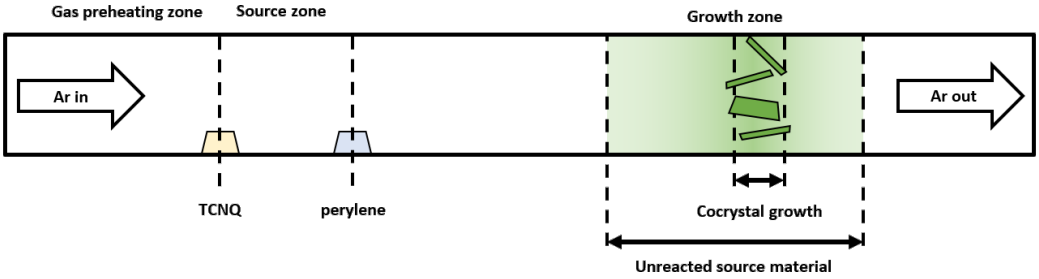

(a) Schematic overview. The starting material is placed at the source zone, sublimates and is then transported to the deposition zone, where it condenses to form crystals

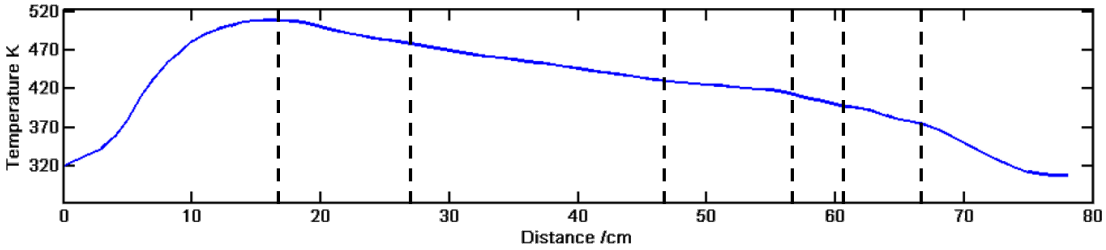

(b) Furnace temperature profile

Figure 3-5: *The physical vapour transport system.*

According to Laudise *et al.* [57] the main transport mechanism is not diffusion or forced convection from gas flow but formation of buoyancy driven convection cells due to the temperature gradient. These are somewhat analogous to atmospheric Hadley Cells, and are generated by the interplay between gravitational forces and the density difference caused by the temperature gradient. The hot gas near the source will rise and then move along the furnace to the colder region, where it will then fall back down as it loses temperature and is again driven back to the source. In a closed system this convection cell will reverse direction at the end of the ampoule, and in an open system it will reverse where the temperature gradient decays significantly.

By contrast Rosenberger *et al.* [86] suggest that diffusion-advection can in fact dominate in relatively large regions near vapour-solid interfaces, with the size of these regions dependant on a complex array of factors, including the momentum, mass, species and energy transfer. They claim that high fidelity 3D analysis is required to adequately analyse these systems as more simplistic 2D models typically ignore local temperature gradients and the interactions between the buoyancy driven convection and gas flow which can in fact dominate. As such, Rosenberger *et al.* claim it is difficult to make generalised statements regarding furnace growth; however they do note that it is often the case that multiple convection cells are likely to occur in systems that have a temperature peak as opposed to a uniformly decreasing temperature gradient, which is in

line with Laudise *et al.*'s analysis.

For successful growth of two component crystals it is important for the sublimation rate to be the same for both starting materials, which can be accomplished via pre-crystallisation or by placing them in different temperature regions inside the furnace.

Hu *et al.* [40] report a trade-off between surface diffusion and nucleation rate. For an open system very low super-saturation is sufficient for spontaneous nucleation so at low temperature a large number of crystals are produced. Increasing the temperature results in more surface diffusion and promotes growth of pre-existing crystallisation sites, however raising the temperature also increases the evaporation rate. This results in higher supersaturation, and therefore will increase the overall rate of nucleation, once again resulting in a larger number of small crystals.

To obtain large crystals, it is necessary to use a high temperature while also reducing the sublimation rate to compensate. This can be most easily accomplished by pre-crystallising the starting materials. This will reduce their surface area compared to a powder and therefore lower the rate of evaporation, resulting in a lower overall nucleation rate while still promoting growth of pre-existing crystallization sites. [40]

3.2.4 Melt Based Growth

Melt based growth methods have also been used to grow other organic materials, and, while less commonly used for CT complexes, Kim *et al.* [54, 53] have demonstrated a melting based growth method for producing a range of CT complexes, including TTF-F_4TCNQ. This technique may be difficult to expand to other systems, however, as it depends on both components to form a eutectic complex, meaning both components melt and solidify at a single temperature. This is a new area of development, and it remains to be seen if melt based techniques will become a viable way of growing CT complexes, and whether they will have any advantages over other methods.

3.3 Estimation of the Degree of Charge Transfer

The degree of charge transfer, ρ, is an important characteristic, as it is directly responsible for numerous physical characteristics, including charge transport properties, magnetic properties, lattice energy and the nature of any possible Peierls transition. [38] Broadly speaking there are two main methods of estimating this parameter, either

via bond length measurements, or via changes in the frequency of vibration. Interplanar spacing between donor and acceptor molecules is correlated, with a higher degree of charge transfer associated with smaller distances, but as there are many other factors that also contribute to the intermolecular distance it cannot be used as reliable estimator.

3.3.1 Bond Length Methods

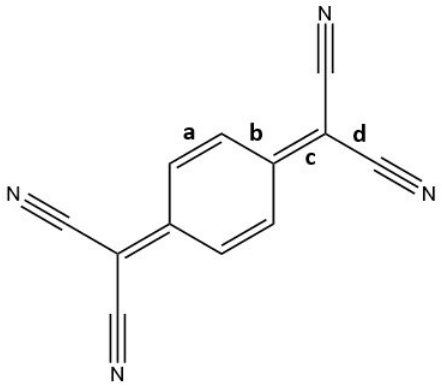

Figure 3-6: *Skeletal bond structure of TCNQ, with bonds a, b, c and d labelled.*

Tetracyanoquinodimethane (TCNQ) has been extensively studied in CT crystals, and as such various methods have been devised to estimate ρ based on bond lengths. The first method is a bond length ratio method by Flandrois, Chasseau and Kistenmacher. [56] In literature it is often referred to as the Kistenmacher Method. Their argument is as follows. As TCNQ becomes charged it becomes more benzenoid in character, thus bonds a and c shorten and b and d lengthen (see Figure 3-6). As there is much smaller unpaired electron density near the vicinity of bond a compared to c, the former does not significantly distort and so only bonds c, b and d are used as indicators.

ρ can be estimated by the relationship:

$$\rho = \frac{\alpha_{CT} - \alpha_0}{\alpha_{-1} - \alpha_0}, \tag{3.2}$$

where $\alpha = \frac{c}{b+d}$ with b, c and d being the respective bond lengths, and the subscripts, CT, -1 and 0 referring respectively to the charge transfer complex, the anion and the neutral TCNQ molecule. This approach can also be applied to the fluorinated derivative for F4TCNQ. [40, 114, 69] α_0 and α_{-1} are constant for a given molecule system, and

CSD Identifier	Structure	α_0	α_{-1}
Averaged		0.480	0.496
TCNQ Neat Crystal [66]	TCNQ	0.476	
OJIXOU	(dbbpy)Pd(dmid) TCNQ	0.485	
GIVZUG	(CH_3NHCS)-bis(CH_3S)-TTF TCNQ	0.492	
ROJSIS	diethyl-bi(pyridothiadiazolylidene) TCNQ	0.499	
JOBSOI	TSC_2-TTF TCNQ		0.479
SIRMUB	BMDMTF TCNQ		0.472
KTCYQM01	K^+TCNQ^-		0.501
MCFETC03	$[Fe(C_5Me_5)_2]^+TCNQ^-$		0.499

Table 3.1: *Kistenmacher parameters from the review by Herbstein and Kapon, [26] showing their averaged values, the values for neat TCNQ and the values for most extremal structures that met their criteria for inclusion.*

so this relationship can be expressed more simply as:

$$\rho = -A\frac{c}{b+d} + B, \tag{3.3}$$

where $A = \frac{1}{\alpha_0+\alpha_1}$ and $B = \frac{\alpha_0}{\alpha_0+\alpha_1}$.

From the above expression is it quite clear that the estimate depends significantly on values chosen for neutral and singularly charged TCNQ, and even relatively minor variations in bond length could lead to significant variation in the final estimation of ρ. A comprehensive review by Herbstein and Kapon [26] collated 66 reported bond length values for neutral TCNQ, and 39 for singularly charged TCNQ. Only error-free Cambridge Structural Database (CSD) entries without disorder and with the Rietveld error structure factor, $R_f \leq 5\%$, were considered. These were then checked against the original publications and any with doubtful features were discarded, as were any that did not display D_{2h} symmetry within 0.020 Å. The results of this is summarised in Table 3.1. Using the averaged bond lengths, as collated by Herbstein and Kapon, leads to an A value of -68.56 and a B value of 32.94.

Of the relevant bonds, Herbstein and Kapon note that for neutral TCNQ formal double bond c has a range of 0.058 Å, and formal single bonds b and d have a range of 0.014 Å and 0.016 Å respectively. For singly charged TCNQ the spread is even larger and their conclusion is that due to this wide discrepancy it is hazardous to try and estimate ρ from bond length based methods alone. Indeed it is notable that for some of the

measurements, the value of α_{-1} is actually smaller than α_0, which would, according to the Kistenmacher model, suggest the neutral molecule is more negatively charged than the anion.

One further issue with this approach is that this method is even more unreliable for near neutral complexes, with the reported literature value of perylene-TCNQ being 0.01±0.07. [107] The error in this case greatly surpasses the measured value.

3.3.2 Harmonic Oscillator Stabilisation Energy (HOSE)

A second method dependent on bond length is based on the Harmonic Oscillator Stabilisation Energy (HOSE) of the structure. [62] A real molecule with delocalised electrons can be treated as a combination of idealised resonance structures (also sometimes referred to as canonical structures), each of which contains only single or double bonds (Figure 3-7). HOSE is a measure of the value of the resonance energy, or stability, of a structure and is defined as the energy required to deform the geometry of the real molecule into the geometry of one of its resonance structures. The following argument is based on the derivation by Krygowski and Anulewicz. [62] HOSE can be derived from a simple harmonic oscillator relationship as:

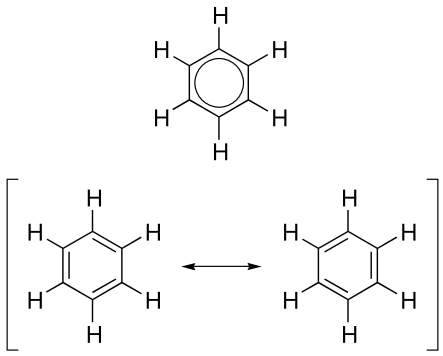

Figure 3-7: *The structure of benzene, top, can be considered as the combination of two contributing resonance structures, bottom. In the case of benzene, the contribution from both resonance structures is equal.*

$$HOSE = -\frac{1}{2}\left[\sum_{r=1}^{n}(R_r - R_0)^2 k_r\right], \tag{3.4}$$

Bond	R_0^s (Å)	R_0^d (Å)	a ($\times 10^4$ Pa)	b ($\times 10^4$ Pa)
CC	1.467(2)	1.349(1)	44.39	26.02
CN	1.373	1.274	43.18	25.73
CO	1.428	1.209	52.35	32.88

Table 3.2: *The constants used in the HOSE model. C-C and C=C data taken from electron diffraction (ED) data for 1,3-butadiene. [64] C-N taken from microwave data for methylamine. [85] C=N taken from ED data from 2-propene-1-imine. [79] C-O taken from ED data for methanol. [55] C=O taken from ED data for acrolein. [63]*

where R_r is the actual bond length and R_0 is the appropriate formal bond length (i.e. an idealised single or double bond) for all n bonds. k_r is the force constant, which can be assumed to be proportional to R_r as:

$$k_r = a + bR_r. \tag{3.5}$$

Substituting this expression into 3.4 and separating out the single and double bonds leads to the more useful expression:

$$HOSE = 301.15\left[\sum_{r=1}^{n_1}(R'_r - R_0^s)^2(a + bR'_r) + \sum_{r=1}^{n_2}(R''_r - R_0^d)^2(a + bR''_r)\right], \tag{3.6}$$

where R'_r and R''_r are the lengths of the π bonds in the real molecules, n_1 and n_2 are the number of single and double bonds in the structure, R_0^s and R_0^d are the canonical single and double bond lengths and a and b are constants, depending on the type of bond. These values are listed in Table 3.2. The factor 301.15 allows the HOSE values to be expressed in kJ mol^{-1}. Each resonance structure has its own HOSE value, with the total HOSE for the molecule equal to:

$$HOSE = \sum_{i=1}^{N} C_i HOSE_i, \tag{3.7}$$

where N is the total number of resonance structures and C_i is the contribution of the ith resonance structure, equal to:

$$C_i = \frac{(HOSE_i)^{-1}}{\sum_{j=1}^{N}(HOSE_j)^{-1}}. \tag{3.8}$$

The standard uncertainty for the HOSE increases about 2 to 4 times faster than the uncertainty for the bond lengths and geometries of molecules used to calculate it, due

to error propagation. For reliable calculations the uncertainties for bond lengths should be no greater than 0.004 Å if the HOSE is to have an uncertainty lower than 7%. Fortunately C_i, which is used to estimate ρ, is not as dependent on variations in geometry and experimental error when compared to the actual HOSE values themselves.

For TCNQ it is possible to estimate ρ by considering the contribution of the central aromatic ring molecular fragment. This fragment has three possible resonance structures, the normal quinoid form, 0, and two benzene-like structures, B_1 and B_2. Krygowski and Anulewicz [62] report that the contribution of the quinoid form is directly proportional to the fractional charge on TCNQ, $C_{Quinone}$, which they refer to as Q. (Figure 3-8)

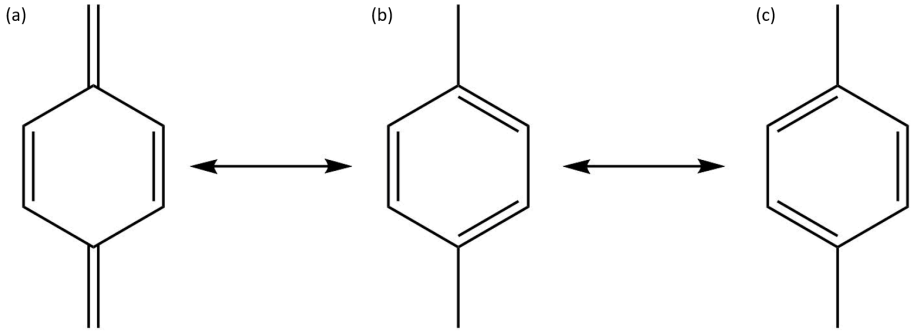

Figure 3-8: *The central fragment of TCNQ relevant to the HOSE model, showing the three resonance structures. ρ is proportional to the contribution of the quinoid form, (a).*

By using linear regression based on 11 TCNQ complexes taken from literature, they report a relationship of:

$$Q = -46.2\rho + 91.2, \tag{3.9}$$

with a correlation coefficient r = 0.992. This can be more usefully rearranged as:

$$\rho = 1.9740 - 0.0216Q. \tag{3.10}$$

However, in their follow up paper [109] they report a relationship of:

$$\rho = 2.243 - 0.0245Q, \tag{3.11}$$

based simply on the values for neutral and singly charged TCNQ. While this approach is similar to the previous method, the HOSE model does not assume that the lengths

Bond	$DBTTF^{0}$ (Å)	$DBTTF^{+0.25}$ (Å)	$DBTTF^{+1}$ (Å)
a	1.336(2)	1.358(6)	1.393(6)
b	1.759(2)	1.747(4)	1.718(4)
c	1.748(2)	1.751(4)	1.742(2)
d	1.399(2)	1.398(6)	1.396(8)
e	1.384(3)	1.386(7)	1.387(8)
f	1.379(3)	1.378(8)	1.378(8)
g	1.383(3)	1.368(8)	1.370(8)

Table 3.3: *Comparison of the average bond lengths of DBTTF. All values taken from [24]. Values are taken from neat DBTTF, DBTTF-TCNQ and DBTTF-F_4TCNQ respectively.*

of the *b*, *c* and *d* bonds in the radical anion must be equal. [109] This model is also in principle more generally applicable, and could be expanded to TCNQ derivatives and other molecular systems with aromatic rings.

3.3.3 Other Methods for Non-TCNQ Systems

Iwasaki et al. [45] report that for DBTTF it is possible to estimate ρ from the length of either the a or b bonds of the molecule. The relevent values are listed in Table 3.3. This is purely an empirical observation, and the authors provide no explanation as to why those particular bonds would change lengths. Furthermore, since this estimate depends on a single molecular bond length it is rather unreliable. It is both highly susceptible to measurement uncertainties and also to a variety of extrinsic factors such as the temperature at which the crystal structure has been determined.

3.3.4 Spectroscopic Methods

It is also possible to estimate ρ from various spectroscopic techniques. These methods all work by examining shifts in frequency of spectroscopic resonances, caused by the charge transfer, compared to a neutral molecule.

IR

The IR spectrum of charge transfer complexes undergo three major changes to their neutral constituent components. New low frequency peaks may appear in the far

infrared region due to the vibrations of one molecule in the complex against another, [112] the intensities of the peaks may change and the vibrational frequencies of the donor or acceptor may become shifted. [27] This last feature has diagnostic utility as the shift in frequency is linearly proportional to ρ as:

$$\rho = 2\frac{\Delta\nu}{\nu_0}\left(1 - \frac{\nu_1^2}{\nu_0^2}\right)^{-1}, \tag{3.12}$$

where $\Delta\nu = \nu_0 - \nu_{CT}$. [17, 51]

For TCNQ the asymmetric C=C stretching at 1543 cm^{-1}, which goes to 1509 cm^{-1} for singly charged TCNQ, is a suitable vibrational mode. This change in frequency is due to the molecule shifting from a more quinonoid structure to a more benzenoid one. The C≡N stretching modes about 2200 cm^{-1} could also potentially be used, as shown in Figure 3-9, but the C≡N bonds are particularly exposed to effective intermolecular interactions and are therefore highly sensitive to the environment.

For Perylene F_4TCNQ the C=C modes at 1500 cm^{-1} and 1536 cm^{-1} and the C≡N stretching modes at 2216 cm^{-1} are sensitive to changes in ρ. However, as with unfluorinated TCNQ, the C≡N mode is subject to extrinsic effects and therefore potentially less useful.

Raman

Vibrational IR spectra can often be quite complex, with overlapping modes from both the donor and acceptor. By contrast Raman traces are generally simpler; as they tend to lack resonances from free charge carriers and overtone, combination and difference bands are rare. As such it is often possible to isolate the TNCQ contributions. Unfortunately, Raman measurements are susceptible to perturbing effects due to coupling between totally symmetric intramolecular vibrations and charge carriers, known as electron-molecular vibration or e-mv coupling. [28, 71]

For mixed stack CT complexes the frequency of the totally symmetric Raman-active modes are lowered by e-mv coupling, with the exact relationship dependent on the geometry of the stack.

Assuming the isolated band approximation, and for dimerised complexes, defined as a complex where each molecule does not have the same CT integral with its nearest

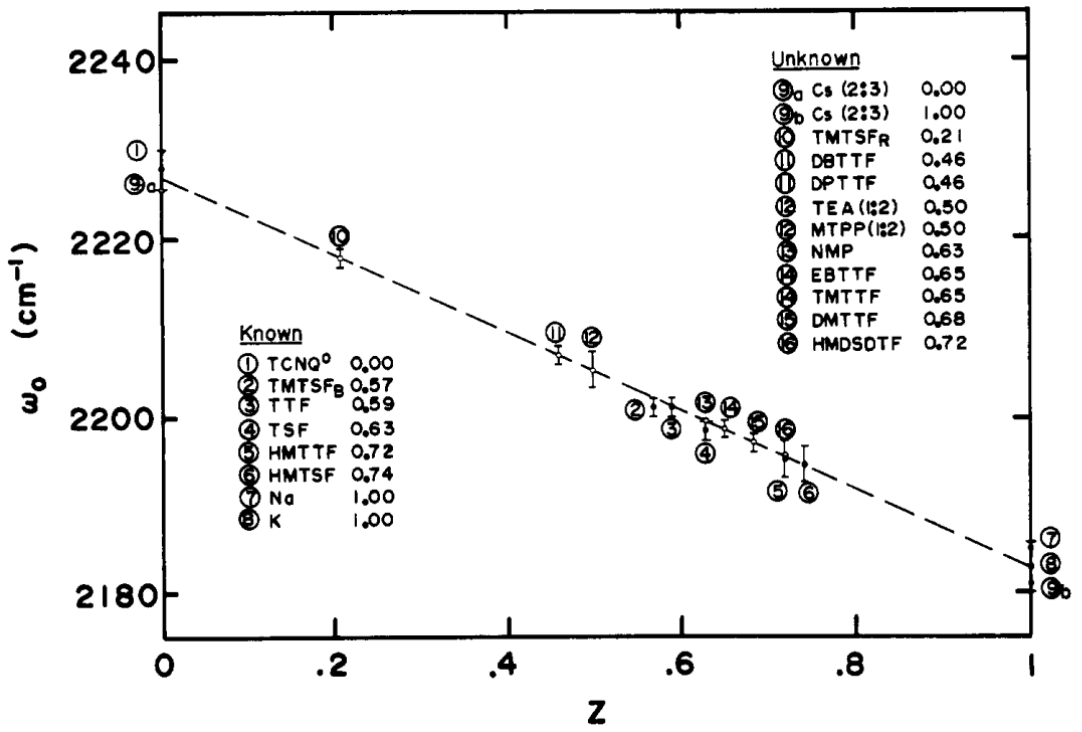

Figure 3-9: *Nitrile stretching frequency, ω_0 vs. degree of charge transfer, Z, for 19 TCNQ salts. A clear correlation can be seen between the frequency and the degree of charge transfer, indicating that this peak could be used for diagnostic purposes. Figure taken from Chappell* et al. *[17]*

neighbours, the relationship for the perturbed frequency, ν, is given by:

$$\nu = \nu_0\sqrt{1 - \frac{4g^2\rho(1-\rho)}{v_0 v_{CT}}} \approx v_0 - \frac{2g^2\rho(1-\rho)}{\nu_{CT}}, \tag{3.13}$$

where ν_0 is the frequency for the neutral molecule, ν_{CT} is the frequency for the complex and g is the e-mv coupling constant. [29]

For non-dimerised mixed stack complexes, where each molecule has the same CT integral with its nearest neighbour, the result is analogous, but instead of ν_{CT}, it is dependent on ν_E, the energy difference between the ground and symmetric excited state. This is given by

$$\nu_E = \begin{cases} \frac{\nu_C T}{1-\rho}, \rho < 0.5 \\ \frac{\nu_C T}{\rho}, \rho > 0.5 \end{cases}. \tag{3.14}$$

Resonant Raman

Resonant Raman (RR) spectroscopy is a technique where the energy of the incident photon is close in energy to an electronic transition for the material under study, which can potentially greatly enhance signal strength for vibrational modes that undergo a change in bond length or force constant during electronic excitation. Jeanmaire and Van Duyne [48] demonstrated that it was possible to use RR to distinguish different TCNQ moieties in solution. The C=C ν_4 stretching mode goes from 1454 cm^{-1} for neutral TCNQ to 1385 for singly charged TCNQ.

3.3.5 Reflectance Spectroscopy

Reflectance spectroscopy is a way of probing samples that are otherwise difficult to analyse by transmission spectroscopy, such as highly absorbing media. While it cannot directly provide information about ρ, it is possible to derive the transmission and absorption response by applying Kramers-Kronig transforms to the spectrum. These can be used to determine the energy of the charge transfer bands, and also the orientation of the crystals by using polarised light.

There are two broad categories of reflectance spectroscopy: internal and external reflectance. Internal reflectance examines the interaction between the surface of a sample and a medium with a higher refractive index, while external reflection measurements use light that is reflected off the sample surface.

External reflectance measurements can be classified as either specular or diffuse depending the roughness of the surface sample. Specular reflection is mirror like with the angle of incidence equal to the angle of reflectance, whereas diffuse reflection occurs where there is significant scattering through multiple angles. For good quality single crystal CT complex samples specular reflection will typically dominate.

When light moves from a medium with a refractive index n_1 to a medium with refractive index n_2 it will undergo reflection and refraction as governed by the Fresnel equations. [35]

$$r(\omega) = \frac{N(\omega) - 1}{N(\omega) + 1} = \frac{n(\omega) + i\kappa(\omega) + 1}{n(\omega) + i\kappa(\omega) - 1} = |r(\omega)|e^{i\theta(\omega)}|, \tag{3.15}$$

where $r(\omega)$ is the complex reflectivity, $N(\omega)$ is the complex refractive index, comprising of a real component $n(\omega)$ and the imaginary component $\kappa(\omega)$, also known as the

extinction coefficient. $\theta(\omega)$ is the phase of the complex reflectivity. Reflectance measurements will typically measure the amplitude of the reflected beam, R, which is equal to $|r(\omega)^2|$.

Internal reflectance spectroscopy is often termed attenuated total reflection (ATR). For this method the sample is mounted onto a suitable ATR crystal (such as diamond, zinc selenide or germanium) and a beam of infrared light is passed through it so that it reflects off the internal surface via total internal reflection; this creates an evanescent wave that penetrates into the sample and can couple with surface waves (i.e. plasmons, polaritons, excitons etc.) that are present. This will cause the evanescence wave to be absorbed by the sample (hence, attenuation) at certain wavelengths. [52]

Kramers-Kronig Relations

Kramers-Kronig relations link the real and imaginary part of analytic complex functions. They are a powerful tool that can be applied to a wide range of linear complex optical functions, such as the dielectric function, refractive index and reflectivity. More formally, following the derivation described by Lucarini *et al.* [67], for any linear susceptibility function:

$$a(\omega) = a_1(\omega) + ia_2(\omega), \tag{3.16}$$

where a_1 and a_2 are real, then:

$$a_1(\omega) = \frac{1}{\pi}\mathcal{P}\int_{-\infty}^{+\infty} \frac{a_2(\omega')}{\omega' - \omega} d\omega' \tag{3.17}$$

$$a_2(\omega) = -\frac{1}{\pi}\mathcal{P}\int_{-\infty}^{+\infty} \frac{a_1(\omega')}{\omega' - \omega} d\omega', \tag{3.18}$$

where $\mathcal{P}$ is the Cauchy principal value. For systems where $a(-\omega) = a^*(\omega)$ we can write these relations in the somewhat more useful form of:

$$a_1(\omega) = \frac{2}{\pi}\mathcal{P}\int_{0}^{+\infty} \frac{a_2(\omega')}{\omega'^2 - \omega^2} d\omega' \tag{3.19}$$

$$a_2(\omega) = -\frac{2\omega}{\pi}\mathcal{P}\int_{0}^{+\infty} \frac{\omega' a_1(\omega')}{\omega'^2 - \omega^2} d\omega'. \tag{3.20}$$

This allows the determination of dispersive relationships from absorptive relationships (and vice versa). From this, it is possible to derive from equation 3.15 the relationship:

$$\ln r(\omega) = \ln |r(\omega)| + i\theta(\omega). \tag{3.21}$$

Unfortunately this function diverges logarithmically for the limit $|\omega| \to \infty$ and is therefore not square integrable, which is a requirement for Kramers-Kornig relations to hold. However, it is still possible to derive a valid Kramers-Kronig relation from first principles by using a function involving $\ln r(\omega)$ that approaches 0 at infinity. Such a function:

$$F(\omega) = \frac{\ln r(\omega)}{\omega^2 - \omega'^2} \tag{3.22}$$

can be used, as in the case for a dielectric function with usual asymptotic behaviour:

$$\lim_{x\to\infty}[\epsilon(\omega)] = 1 - \frac{\omega_p^2}{\omega^2}. \tag{3.23}$$

$F(\omega) \sim \omega^{-2}$ for the limit $|\omega| \to \infty$, where $\epsilon(\omega) = \epsilon_1(\omega) + i\epsilon_2(\omega)$ is the complex dielectric constant and ω_p is the plasma frequency. [96]

This then yields the relationship:

$$\theta(\omega) = -\frac{2\omega}{\pi}\mathcal{P}\int_0^{+\infty} \frac{\ln r(\omega')}{\omega'^2 - \omega^2} d\omega', \tag{3.24}$$

which allows for the real and imaginary components of the refractive index to be determined from:

$$n(\omega) = \frac{1 - |r|^2}{1 + |r|^2 - 2|r|\cos\theta} \tag{3.25}$$

$$\kappa(\omega) = \frac{-2|r|\sin\theta}{1 + |r|^2 - 2|r|\cos\theta}. \tag{3.26}$$

For real measurements it is obviously not possible to measure reflectance across all frequencies from 0 to infinity and so existing spectral data must be extrapolated. Care must be taken to select an appropriate method, as there are several possible commonly used techniques. One approach is to record data between a range ω_a and ω_b and then divide the integral into three parts:

$$\int_0^{+\infty} = \int_0^{+\omega_a} + \int_{\omega_a}^{+\omega_b} + \int_{\omega_b}^{+\infty}. \tag{3.27}$$

For $0 \leq \omega \leq \omega_a$ it can then be assumed that $r(\omega) = r(\omega_a)$ and for $\omega > \omega_b$ the electrons in the material can be treated as a free gas. [59] As alluded to previously (equation 3.23) the high frequency dielectric constant is given by:

$$\epsilon(\omega) = 1 - \frac{\omega_p^2}{\omega^2}. \tag{3.28}$$

From this relationship it is possible to determine the high frequency behaviour of ϵ_1, ϵ_2 and hence R by using the generalised form of the Fresnel equation (equation 3.15). This yields an extrapolation function of:

$$R(\omega) = R(\omega_b)\left(\frac{\omega_b}{\omega}\right)^4, \tag{3.29}$$

which then leads to an integral of:

$$\int_{\omega_b}^{+\infty} = \frac{1}{2}\int_{\omega_b}^{+\infty} \frac{\ln R(\omega_b) + 4\ln(\frac{\omega_b}{\omega})}{\omega'^2 - \omega^2} d\omega', \tag{3.30}$$

which can be then be evaluated using a geometric series.

Hulthén [42] developed a method where the Kramers-Kronig relations are generalised for finite frequency intervals provided that the imaginary and real parts are known for at least partially overlapping frequency intervals. Milton *et al.* [72] also proposed using finite frequency relationships, but which rely on information measured independently at known reference points.

Altarelli and Smith [1] proposed an alternative set of Kramers-Kronig relationships by considering the relationships $[N(\omega) - 1]^m$ and $\omega^m[N(\omega) - 1]^m$ that converge strictly faster that the previous relation for $m >$. Smith and Manogue [97] derived similar results using the functions $[r(\omega)]^m$ and $\omega^m[r(\omega)]^m$.

Bachrach and Brown [6] suggested singularly subtractive Kramers-Kronig relationships that rely on a single reference point $\eta(\omega_1)$:

$$n(\omega_1) - 1 = -\frac{2}{\pi}\mathcal{P}\int_0^{+\infty} \frac{\omega'\kappa(\omega')}{\omega'^2 - \omega_1^2} d\omega'. \tag{3.31}$$

Subtracting equation 3.29 from the conventional Kramers-Kronig relationships for the real and imaginary components of the refractive index:

$$n(\omega) = -\frac{2}{\pi}\mathcal{P}\int_0^{+\infty} \frac{\omega'\kappa(\omega')}{\omega'^2 - \omega^2} d\omega', \tag{3.32}$$

leads to the following relationship:

$$n(\omega) - n(\omega_1) = \frac{2(\omega_2 - \omega_1^2)}{\pi} \mathcal{P} \int_0^{+\infty} \frac{\omega' \kappa(\omega')}{(\omega'^2 - \omega^2)(\omega'^2 - \omega_1^2)} d\omega', \tag{3.33}$$

which again converges more rapidly than the conventional forms. This approach can be extended to yield multiply subtracted relationships which require multiple reference points and have an even more rapid rate of convergence.

3.4 Structural and Thermodynamic Analytic Techniques

3.4.1 Differential Scanning Calorimetry

Differential scanning calorimetry (DSC) is a thermoanalytic technique which can be used to measure the heat flow into or out of a sample as it is heated or cooled. This provides both qualitative and quantitative information about any endothermic or exothermic processes or changes in heat capacity.

A differential scanning calorimeter consists of a sample pan and a reference pan, both connected to heating elements. The reference consists of an inert material that will not undergo any thermal events over the given temperature range. Typically alumina or aluminium is used. Both the sample and the reference undergo a linear temperature sweep. Both the sample and the reference are maintained at the same temperature, and so the difference in the heat flow to the sample and reference is measured as a function of time.

Since the DSC is at constant pressure, the heat flow is equivalent to enthalpy changes:

$$\left(\frac{dq}{dt}\right)_p = \frac{dH}{dt}, \tag{3.34}$$

where t is time. The heat flow difference between the sample, s, and the reference, *ref*, is:

$$\Delta \frac{dH}{dt} = \frac{dH_S}{dt} - \frac{dH_{ref}}{dt}. \tag{3.35}$$

For example, if the sample material melts during the temperature sweep, this is an endothermic process. Therefore, in order to maintain the same temperature as the reference material, additional energy will need to be supplied to the sample heating element. This change in heat flow will then appear as a peak on the DSC trace. [95]

3.4.2 X-Ray Crystallography

X-ray crystallography is a technique used to determine the position of atoms and molecules in a given crystal structure. There are several different x-ray based methods, but in this work we exclusively use single-crystal x-ray diffraction. Here a monochromatic beam of x-rays is fired at a single crystal which will produce a diffraction pattern of spots. The sample is then rotated and the pattern measured for all angles. Each single diffraction spot is called a reflection, as it corresponds to the x-ray reflecting off one set of planes within the crystal via Bragg diffraction.

These data describe the amplitude of the Fourier transform of the crystal's electron density, but lack phase information. In order to determine the real electron density, the phase must be reconstructed. This is known as the Phase Problem, and there are several possible ways of producing an initial phase estimate.

For relatively small (fewer than 1000 atoms) structures it is possible to use direct methods, which exploit statistical correlations between phases and the magnitude of the structure factor. If phase information for a similar structure is known, it can be used as a starting point, which is then modified by a process known as molecular replacement. As this work only looks at small organic molecules, direct methods were used to determine their structure.

For larger structures, another possible technique is Multiple Isomorphous Replacement (MIR). Here heavy ions are introduced into the structure without altering the crystal lattice. By comparing the data obtained with and without these heavy ions it is possible to determine the amplitude and phase of the heavy ion contribution. At minimum two such derivatives are required, as a single one will give two possible phase solutions. It is also possible to use a process known as Multiwavelength Anomalous Dispersion (MAD), which exploits the anomalous scattering behaviour of some atoms near their x-ray absorption edge.

Regardless, the resultant model then undergoes a process of structural refinement, where the parameters of the trial structure are varied until the best fit is achieved between the observed diffraction pattern and that predicted by the model. The quality of the solution can be quantified by the values of the R indices, R_1 and wR_2, and the overall goodness of fit (GooF).

R_1, often called the R-value or discrepancy index, is the agreement between the calcu-

lated model and the observed one. [77] It is equal to

$$R_1 = \frac{\sum |F_{obs}| - |F_{calc}|}{\sum |F_{obs}|}, \tag{3.36}$$

where F is the structure factor, a mathematical function describing the amplitude and phase of waves diffracted by the crystal lattice planes, and the sum extends over all reflections. If there is a perfect match between the observed and calculated structures, R would have a value of 0. In practice random errors will mean that even the best models will have a non-zero R-value. Generally speaking a value of less than 5% is considered a good solution, but it is important to note that this is a measure of precision, and not accuracy. wR_2 is similar to R_1, but instead takes the squares of the structure factors and applies a weighting factor, w, according to estimates of the precision of each structure factor $\sum w(F^2_{obs} - F^2_{calc})^2$.

$$wR_2 = \frac{\sum |w|F^2_{obs} - F^2_{calc}|^2|}{\sum |wF^2_{obs}|^2}. \tag{3.37}$$

Finally, there is the overall goodness of fit, which, in addition to the difference in structure factors also takes into account the number of observed reflections and the parameters used. In an ideal case, this value would be exactly 1.

$$GooF = \left(\frac{\sum w(|F^{obs}|^2 - |F^{calc}|^2)^2}{n - p} \right), \tag{3.38}$$

where n is the number of reflections and p is the number of parameters in the model used.

Caution must be taken regarding the reported accuracy and precision of x-ray crystallographic measurements. These techniques involve taking thousands of reflection measurements, which would superficially appear to offer an extremely high degree of precision. Indeed, in the literature, precisions are often reported as high as one part in 10^4. However, as a 1989 report by the International Union of Crystallography (IUCr) Subcommitte on Statistical Descriptors reminds us, "Precise estimates are not necessarily accurate", [90] and this high degree of reported precision may be quite misleading. Despite this, a 2000 paper by Herbstein highlights the inadequacies of crystallographic data reporting, particularly when it comes to unit-cell parameters, and the fact that there has been improvement in precision reporting in the past 40-60 years. [37] While random errors can be reduced by taking an increasing number of observations, these rapidly become insignificant compared to potentially unaddressed sources of systemic errors, including, but not limited to, sample and instrument misalignment and vari-

ations in temperature and chemical composition across samples. These problems are perhaps exemplified in the wide range of "high precision" bond lengths for neutral and singularly charged TNCQ reported in the literature, summarised in Table 3.1.

3.4.3 Electron Paramagnetic Resonance

Electron Paramagnetic Resonance (EPR), also called Electron Spin Resonance (ESR), is a technique used to study material with unpaired electrons. It has many similarities to Nuclear Magnetic Resonance (NMR), but probes electron spins rather than nuclear spins. It has a range applications, including probing radical intermediate species in chemical reactions and the properties of semiconductors.

Theory

The magnetic moment of an electron in the z direction can only assume two values:

$$M_{S_Z} = m_s \cdot \hbar. \tag{3.39}$$

For a single unpaired electron m_s is equal to $\pm\frac{1}{2}$. The magnetic moment, μ_e, is then equal to

$$\mu_e = -g_e \mu_b M_S, \tag{3.40}$$

where $g_e\mu_b$ is the magnetogyric ratio, comprising of the Landé g-factor and the Bohr magneton respectively. In the presence of an external electric field, B, this electron will have an energy equal to

$$E = -\mu_e \cdot B = g_e m_s \mu_b B. \tag{3.41}$$

It is important to note here that the electron will experience not only the effect of the externally applied magnetic field, but any local magnetic fields from neighbouring atoms or molecules. This is analogous to shielding in NMR. For the case that the local field is induced by the applied field, the effective field strength will be

$$B = B_0 + B_{local} = B_0(1 - \sigma), \tag{3.42}$$

where B_0 is the external field, B_{local} is the induced local field and σ is a shielding factor.

Hence, instead of considering the Landé g-factor, we must refer to the effective g-factor, equal to

$$g = g_e(1 - \sigma). \tag{3.43}$$

This factor is roughly comparable to chemical shift in NMR, and provides information about the local electronic environment, namely the interaction between the electron and the electronic structure of the molecule.

Returning to equation 3.41, we can state that for a single unpaired electron there will be two possible energy states for any non-zero field. This is known as Zeeman splitting.

$$E_{+\frac{1}{2}} = \frac{1}{2} g \mu_b B, \tag{3.44}$$

$$E_{-\frac{1}{2}} = -\frac{1}{2} g \mu_b B. \tag{3.45}$$

The difference between these two energy states is simply equal to

$$\Delta E = h\nu = g_e \mu_B B. \tag{3.46}$$

Then by holding the external magnetic field constant and sweeping incident radiation over the sample (or vice versa) it is possible to excite electrons from one state to another. This will appear as an absorbance peak.

By rearranging equation 3.46 we obtain the value of g in terms of the peak frequency and the strength of the external field

$$g = 71.448 \frac{\nu}{B}, \tag{3.47}$$

where the frequency, ν, is measured in GHz and the magnetic field strength, B, is in mT. As the orbitals are anisotropic, the orientation of the molecule within a magnetic field will influence the g-factor, and hence the position of any peaks. In a powder sample the molecules will be randomly orientated, and so the spectrum will display broad peaks incorporating all possible g-factors.

Hyperfine Structure

Based on the above analysis, we would expect to see a single absorbance peak for a given electron with a given g-factor. However, as with J-coupling in NMR leading to split, or multiplet, peaks, hyperfine interactions lead to an analogous effect here. There

are two primary coupling mechanisms, the first is due to dipole interactions from the electron spin magnetic moment and the nuclei magnetic moment. This is an anisotropic effect (as it is contingent on sample orientation in the magnetic field) that is dependant on the distance between the electron and the nucleus in question, as well as the shape of the electronic orbital. The second is known as the Fermi contact interaction.

Isotropic coupling can be expressed as an additional contribution to electron energy level as:

$$E = gm_b B_0 M_s + am_I M_s, \tag{3.48}$$

where a is the hyperfine coupling constant and m_I is the nuclear spin quantum number. Hence, for isotopes which have a zero ground nuclear spin state (which is the case if the atomic number and mass number are both even) there will be no EPR spectra. If this is not the case, then there will be 2NI+1 lines, where N is the number of equivalent nuclei. For $I = \frac{1}{2}$, the intensity pattern will follow Pascal's triangle. For example, if we consider the CH_3 radical, it has three equivalent hydrogen nuclei with $I = \frac{1}{2}$, and hence there will be 4 lines, an intensity pattern of 1:3:3:1.

There are several other factors that may contribute to the energy of the system and introduce additional splitting. Firstly, there are nuclear Zeeman interactions, which are analogous to the previously discussed electronic Zeeman splitting effect but for nuclear spin states.

In systems with more than one electron spin ($S > \frac{1}{2}$) there are Zero Field interactions, so called because their energy level demonstrates splitting even in the absence of a magnetic field. This occurs due to dipole-dipole interactions between the electrons.

Furthermore, if the nuclei have a spin quantum number $I > \frac{1}{2}$ then there will be an electric quadrupole moment that interacts with the electric field gradient. This interaction is often very small relative to the others, and so can sometimes be neglected.

Chapter 4

Materials

4.1 Introduction

In this chapter we explore the various chemical compounds and molecular complexes studied in this work. We begin by describing the properties of the three molecules under study. The electron acceptor, TCNQ (and its fluorinated derivatives), and the two electron donors, DBTTF and perylene.

We then look at the CT complexes, examining both their physical properties and the current state of the literature regarding them.

4.2 Individual Molecules

4.2.1 TCNQ

Tetracyanoquinodimethane (TCNQ) is a cyanocarbon relative of para-quinone. (Figure 4-1a) It is an exemplar electron acceptor with a high electron affinity (3.0 eV). [20] TCNQ is a commonly used electron acceptor, and has been studied extensively since the initial wave of interest in the 1970s, as it forms charge transfer complexes with high conductivity with many other organic and inorganic compounds.

While TCNQ alone is highly electronegative due to the four cyano groups it can be further functionised by replacing the hydrogen atoms with fluorine atoms (Figure 4-1b). This significantly increases the electron affinity (by as much as 0.4 eV in the case of

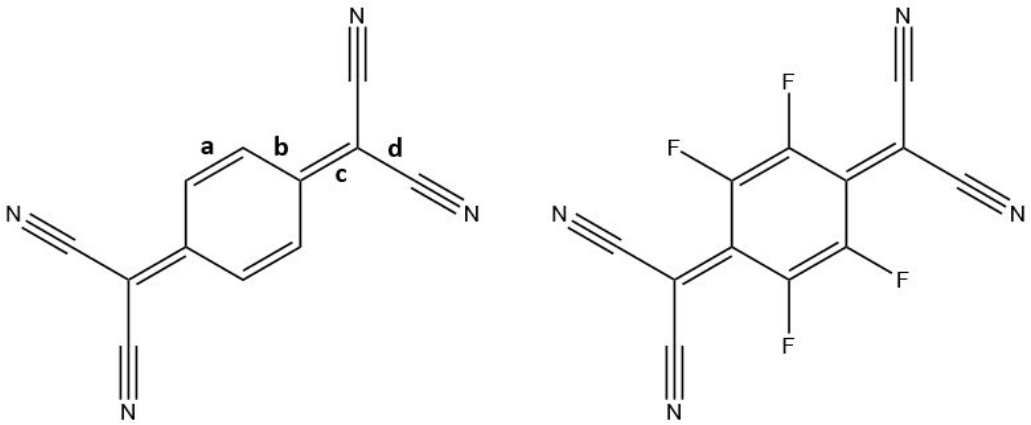

(a) *A TCNQ molecule. Bonds a, b, c and d are labelled*

(b) *An F_4-TCNQ molecule*

Figure 4-1: *The structure TCNQ and its fluorinated derivative.*

F_4TCNQ) without significantly changing the size or geometry of the molecule, allowing for the investigation of the effects of changing the ionicity of any charge complex while minimising other confounding factors.

4.2.2 DBTTF

Dibenzotetrathiafulvalene (DBTTF) (Figure 4-2) is a derivative of the commonly studied donor tetrathiafulvalene (TTF). As such, it is important to briefly comment on TTF itself before then discussing DBTTF.

TTF has garnered significant interest for its use in charge transfer complexes and organic salts as it is capable of readily forming highly conductive compounds. Structurally, it consists of fulvalene, $(C_5H_5)_2$, but with four of the CH groups replaced by sulphur atoms. In 1972 the salt TTF^+Cl^- was shown to be a semiconductor [111] and a year later TTF-TCNQ was reported as the first first highly conductive CT complex. [18, 25]. The high degree of conductivity is primarily due to the fact that TTF and its derivatives typically form CT complexes with a segregated stack geometry. A variety of related compounds have also been studied, including Me_4TTF and tetraselenafulvalene (TSF), where the sulphur atoms are replaced with selenium.

DBTTF is another such derivative, that replaces the terminal carbon double bonds with aromatic rings. This has the effect of raising the ionization potential from 0.3 in the case of TTF to almost 0.5 for DBTTF. In 2005 it was reported that DBTTF-TCNQ had an electron mobility of 1 $cm^2\ V^{-1}\ s^{-1}$ when connected to TTF-TCNQ based metallic

contacts. When connected via gold contacts, the complex has an electron mobility of 13 cm^2 V^{-1} s^{-1} and a hole mobility of 0.04 cm^2 V^{-1} s^{-1}. [110]

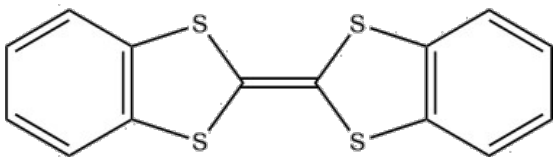

Figure 4-2: *Skeletal structure of a DBTTF molecule.*

4.2.3 Perylene

Perylene ($C_{20}H_{12}$) is a polycyclic aromatic hydrocarbon consisting of two naphthalene molecules connected by a carbon-carbon bond at the 1 and 8 positions on both molecules.

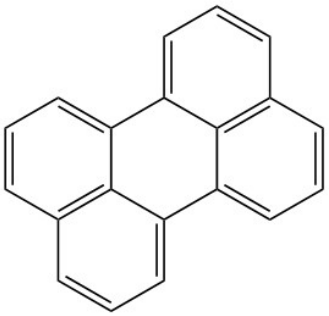

Figure 4-3: *Skeletal structure of a perylene molecule.*

Perylene and its derivatives have a long history of use in thin film organic solar cells as an electron donor with a high ionization energy (6.96 eV) [92] and as an n-type semiconductor. In 1986 Tang [101] reported a bilayer heterojunction with a, then unprecedented, 1% power conversion efficiency comprised of a phtalocyanine derivative (an n-type semiconductor) and a perylene derivative sandwiched between a transparent conducting oxide and a semi-transparent metal oxide. For many years this result was considered a benchmark, and it was not until the turn of the millennium that it was finally surpassed. [87, 81] Perylene, and derivatives like N,N-dimethylperylene-3,4,9,10-dicarboximid (Me-PTCDI), are still in use and studied in small molecule solar cells and they are among the highest performing organic semiconductors. [78]

4.3 Perylene-TCNQ Complexes

4.3.1 Physical Properties

Perylene-TCNQ complexes form a range of different crystal structures, making it possible to establish the effect of the degree of charge transfer and molecule arrangement on charge transfer excitons. Unfortunately it is highly difficult to predict the reaction conditions necessary to favour the growth of specific polymorphs to the exclusion of others, nor is it even known what possible polymorphs can be formed.

While crystals with both a 1:1 and 3:1 stoichiometry have been known and studied for decades, in 2015 an entirely new 1:2 complex was discovered by Vermeulen *et al.*, [107] part of the same group that then went on to report that "Unfortunately, it is still difficult to predict or calculate the stoichiometry and structure of new organic binary compounds." [40] In 2016 further novel polymorphs were reported by Salzillo *et al.* [89]; a 1:1 and 3:2 polymorph of the fluorinated perylene-F_2TCNQ complex.

Perylene-TCNQ most readily forms a charge complex with a 1:1 alternating stack or a 3:1 configuration. In the latter there are additional arrays of perylene molecules that lie between, and almost perpendicular to, the mixed stacks which are of the form (ADDADDA...) along the [001] direction. Both crystals are a dark blue with a metallic lustre, but the 1:1 complex forms extremely thin needles along [001] direction, while the 3:1 complex crystallises as wider block-like parallelograms (often referred to as platelets) which grow along [010] and [001] directions in the bc crystal plane. (Figure 4-4) Crystallographic data is summarised in Table 4.1.

The recently discovered 2:1 polymorph forms platelets visually indistinguishable from the 3:1 form, although they can be distinguished by X-ray diffraction or Raman spectroscopy. Structurally this polymorph is very similar to the 3:1 version and consists of mixed stack arrays with interstitial perylene molecules, except that the stacks are of the form ADADA.

Perylene-F_1TCNQ and Perylene-F_4TCNQ display a mixed stack 1:1 stoichiometry, comparable to the unfluorinated complex, as well as an additional 3:2 configuration. Perylene-F_2TCNQ can produce 1:1, 3:2 and 3:1 configurations. (Figure 4-5) Crystallographic data is summarised in Table 4.1. Fluorination of TCNQ serves to increase its electron affinity, therefore decreasing the energy gap between the LUMO and the HOMO of perylene. (Figure 4-6)

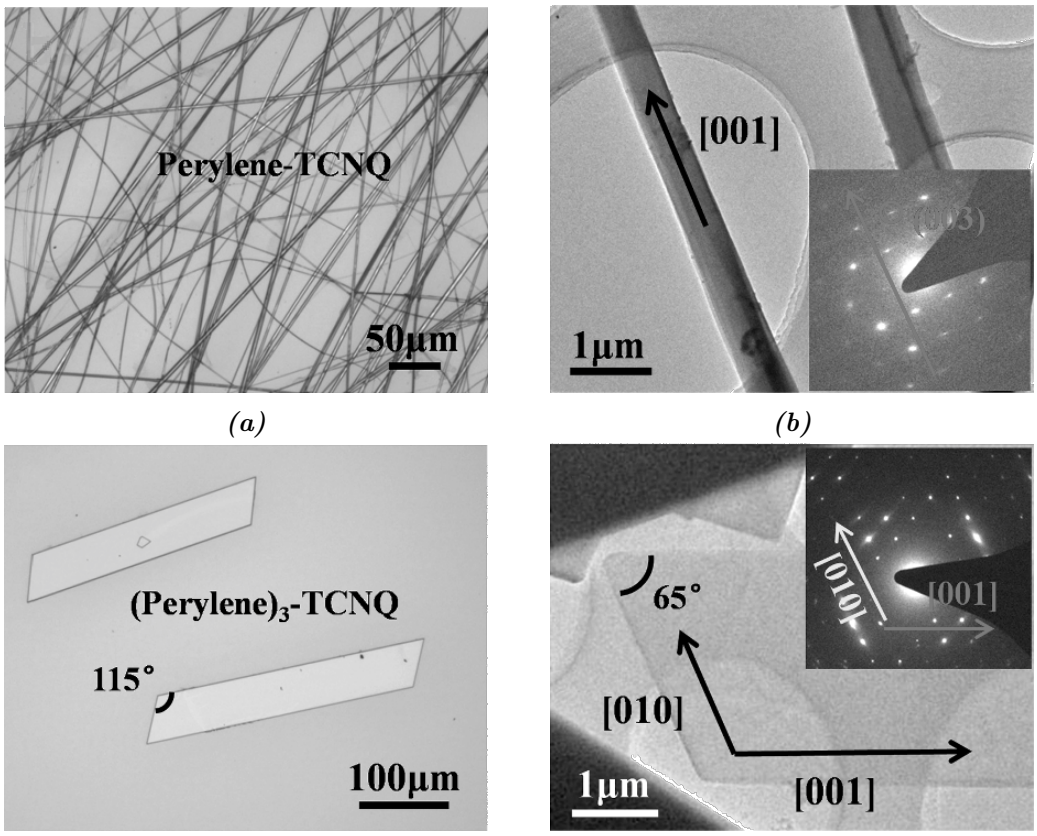

Figure 4-4: *The structure of 1:1 and 3:1 perylene-TCNQ crystals. Figures adapted from Zhu* et al. *[115]. (a): Optical images of 1:1 perylene-TCNQ needles. (b) Transmission electron microscope images of 1:1 perylene-TCNQ needles and selected area diffraction results. (c): Optical images of 3:1 perylene-TCNQ platelets. (d): Transmission electron microscope images of 3:1 perylene-TCNQ platelets and selected area diffraction results.*

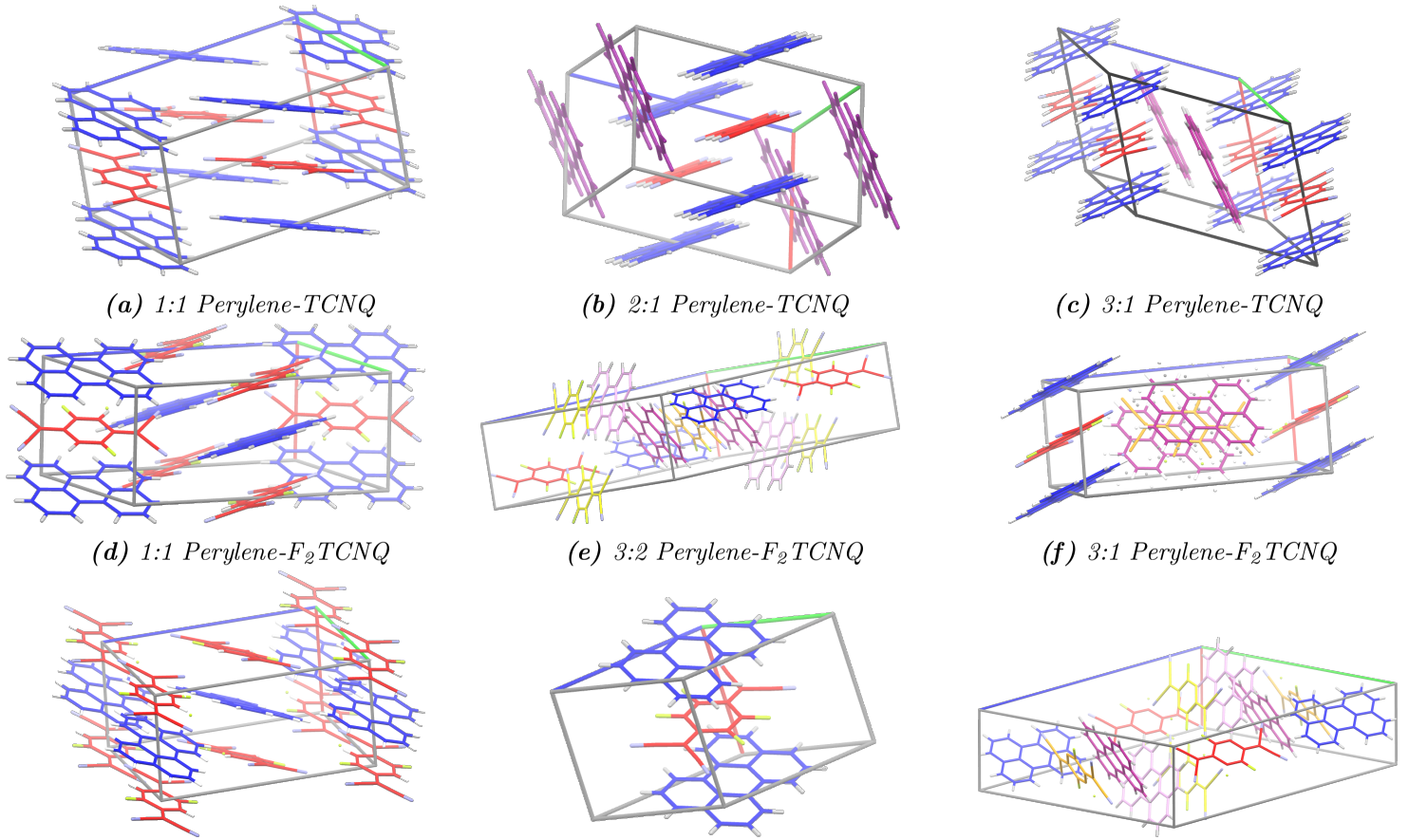

(a) *1:1 Perylene-TCNQ* ***(b)*** *2:1 Perylene-TCNQ* ***(c)*** *3:1 Perylene-TCNQ*

(d) *1:1 Perylene-F_2TCNQ* ***(e)*** *3:2 Perylene-F_2TCNQ* ***(f)*** *3:1 Perylene-F_2TCNQ*

(g) *1:1 Perylene-F_1TCNQ* ***(h)*** *1:1 Perylene-F_4TCNQ* ***(i)*** *3:2 Perylene-F_4TCNQ*

Figure 4-5: *Structures of perylene-F_xTCNQ complexes. Symmetrically equivalent molecules share a colour. Perylene: blue/purple/pink, F_xTCNQ: red/orange/yellow. The unit cells are shown, with the a-axis in red, b in green, and c in blue. (a): PERCTQ02, (b): [107] supporting info, (c): TCQPER02, (d): ELIMET, (e): AKIGEI01, (f): AJUGEU91,(g): AKIGIM, (h): AKIGAE01, (i): NUSZUY01*

The 1:1 perylene-F_2TCNQ crystal consists of alternating stacks along the a axis; however, compared to the unfluorinated crystal the stacks are slipped by one molecular unit with respect to one another and the relative orientation of perylene in the two stacks is different. (Figure 4-5d) The 3:2 perylene-F_2TCNQ polymorph consists of DADA trimers arranged in a quasi one dimensional stack parallel to the c axis. (Figure 4-5e) ρ is estimated to be between 0.10 and 0.22 based on IR spectroscopy. [89]

The 3:2 perylene F_4TCNQ complex is also comprised of DAD trimers with additional DA stacks orientated perpendicularly. ρ correlates to the distance between donor and acceptor, with a shorter distance corresponding to a higher degree of charge transfer, as might be expected due to the better orbital overlap.

There is a decrease in interplanar distance with fluorination, which confirms the theoretical prediction that higher electron affinity should result in a greater degree of charge transfer and matches the results of the spectral data. (Table 4.2)

Table 4.1: *Crystallographic data for Perylene-TCNQ charge transfer complexes.*

	Perylene-TCNQ			Perylene	Perylene F_2TCNQ			Perylene F_4TCNQ [40]	
	1:1 [103]	2:1 [107]	3:1 [34]	F_1TCNQ[40]	1:1 [40]	3:2 [89]	3:1 [89]	1:1 [40]	3:2 [40]
Crystal system	Monoclinic	Triclinic	Triclinic	Monolinic	Monoclinic	Triclinic	Triclinic	Triclinic	Triclinic
Space group	$p2_1/b$	$p_{\bar{1}}$	$p_{\bar{1}}$	$p12_1/c1$	$p2_1/n$	$p_{\bar{1}}$	p	p_1	$p_{\bar{1}}$
a (Å)	7.32	7.18	10.88	7.16	7.02	7.23	7.22	7.00	7.21
b (Å)	14.55	11.08	12.70	10.89	19.20	22.27	11.69	7.28	19.10
c (Å)	10.88	11.90	10.42	14.45	8.37	19.13	18.22	11.27	22.41
α (°)	90	103.81	114.91	90	90	112.28	76.93	104.14	111.80
β (°)	90	102.91	90.8	90.31	90	93.75	82.69	101.96	90.05
γ (°)	90.4	101.32	112.62	90	90.32	90.19	72.14	90.29	94.13

Table 4.2: *Bond lengths and angles for a range of perylene and F_xTCNQ crystals.*

Compound [Ref.]	DA inter-planar distance between perylene and F_xTCNQ molecules (Å)	Angles between perylene and F_xTCNQ mean planes (°)
1:1 Perylene-TCNQ [40]	a axis 3.35	4.15
2:1 Perylene-TNCQ [107]	a axis 3.59	1.44
3:1 Perylene-TCNQ [89]	Not reported	2.99
1:1 Perylene-F_1TCNQ [40]	a axs 3.27	2.91
3:2 Perylene-F_2TCNQ [40]	a axis 3.29 b axis 3.21	0.66
1:1 Perylene-F_4TCNQ [40]	a axis 3.22	2.47
3:2 Perylene-F_4TCNQ [89]	a axis 3.27 trimers 3.21	3.28

Using the bond length method, 1:1 perylene-TCNQ complex gives an estimated ρ value of 0.01±0.07, the 2:1 and 3:1 complexes have values of 0.12±0.07 and 0.23±0.07 respectively. [107] The 1:1 perylene-F_1TNCQ, 3:2 perylene-F_2TCNQ and 1:1 peryelne-F_4TNCQ complexes have values of 0.021±0.061, 0.174±0.01 and 0.303±0.02. [40]. The HOMO and LUMO energy levels for these complexes are summarised in Figure 4-6.

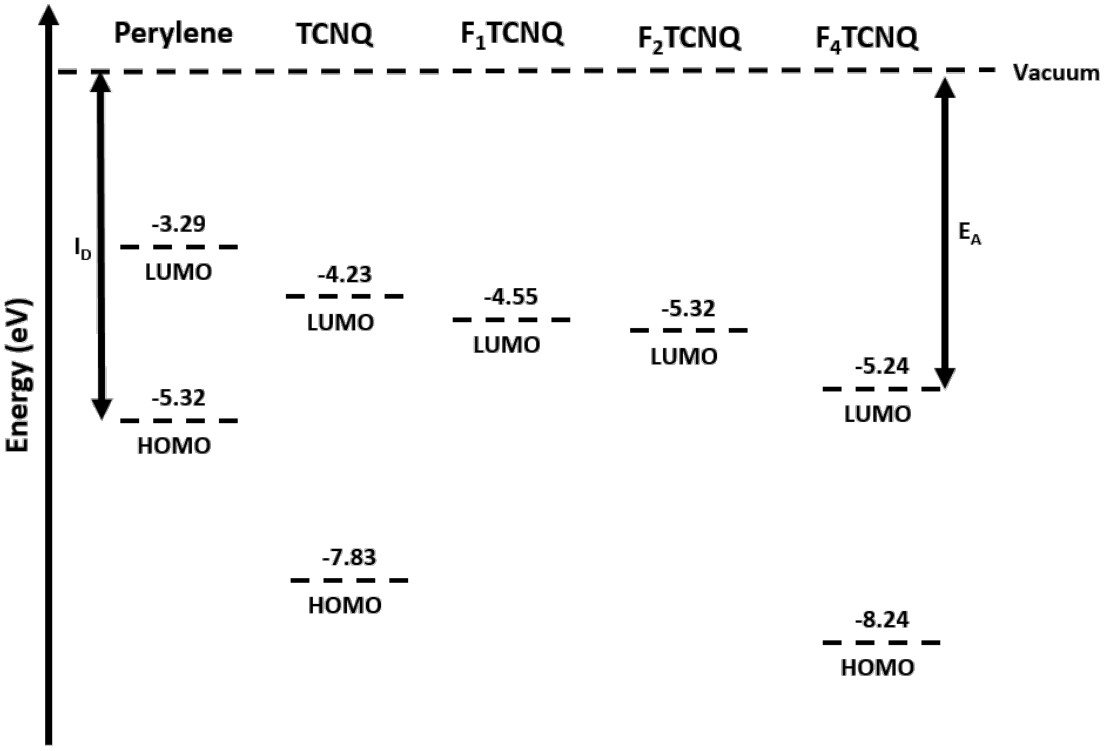

Figure 4-6: *Energy level diagram for perylene and F_xTCNQ. In this case the values for the 3:2 F_2 and 1:1 F_4 complexes are displayed. Data from Hu* et al. *[40]*

Overall increasing fluorination leads to increased electronegativity; however it is also strongly dependent on the structure of the charge transfer complex. The DAD trimers have a much higher degree of charge transfer than DA dimer structures. This is simply due to the fact that the F_xTCNQ molecules are able to interact with two perylene molecules in the trimer, but only one in the dimer.

4.3.2 Optical Excitation

1:1 and 3:1 perylene-TCNQ complexes have been extensively studied, and their conduction properties, optical, Raman and reflection photoconduction spectra have been determined. [7, 44] In 2008 the electronic band structure was finally determined. [93]

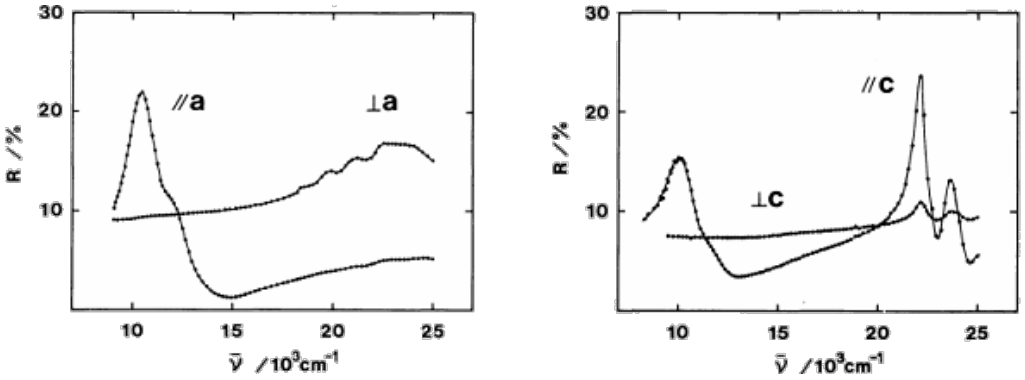

Figure 4-7: *Reflectance spectra for perylene-TCNQ complexes. Figure adapted from Ishii* et al. *[44] (a):* [01$\bar{1}$] *face 1:1 perylene-TCNQ for light parallel and perpendicular to the a axis. (b): Reflectance spectra of* [100] *face of 3:1 perylene-TCNQ for light parallel and perpendicular to the c axis.*

The reflection and absorption spectra of TCNQ have also been reported along with the spectra of its monovalent anion. This is useful as charge transfer interactions can cause a shift in the frequency of spectral features compared to the neutral molecule, making it closer to that of the anion. It is possible to use this to estimate the degree of charge transfer. [80]

For both the 1:1 and 3:1 polymorphs the nearest neighbour electronic overlap is similar but longer range interactions are different due to the presence of the extra interstitial perylene molecules which inhibit any interaction between the stacks. This results in both polymorphs having broadly similar optical spectra as the lowest charge transfer states are similar, but there are differences in the higher order states. In this case there is an extremely low degree of charge transfer and so the 1:1 spectra appears almost identical to the superposition of the spectra of neutral perylene and TCNQ (excluding the additional features caused by the charge transfer). The main charge transfer band is located between 10,500 cm^{-1} and 12,000 cm^{-1} with additional absorption present in the 15,000 cm^{-1} to 20,000 cm^{-1} region, which is associated with higher order states. (Figure 4-7a)

The 3:1 complex also exhibits a band at 10,500 cm^{-1} with a shoulder at 12,000 cm^{-1}. The band at 15,000 cm^{-1} to 20,000 cm^{-1} is still present but much weaker. Additional peaks at 22,200 cm^{-1} and 23,700 cm^{-1} in the 3:1 spectrum are due to the interstitial perylene molecules and can also be seen in perylene in solution and alpha-perylene crystals. (Figure 4-7b)

For 1:1 F_2-TCNQ the degree of charge transfer is estimated to be approximately 0.14 based on spectral shifts in the IR spectroscopy data. [40] For the 1:1 F_4-TCNQ complex the lowest electronic transition has an onset at 5000 cm^{-1} which corresponds to an optical gap of 0.68 eV, and the degree of charge transfer is estimated to be 0.25, 0.25 and 0.28 based on the IR active vibrational modes at 1395, 1550 and 1599 cm^{-1}. For the 3:2 F_4-TCNQ complex, shift analysis gives the degree of charge transfer as 0.29, 0.22 and 0.28 in the DA stack and 0.30 and 0.28 in the trimers.

4.3.3 Electrical Transport Properties

The 1:1 complex demonstrates n-type behaviour in FETs, with an electron mobility as high as 0.3 cm^2 V^{-1} s^{-1} having been reported from single crystal field effect transistors created from physical vapour transport grown samples. Crystals grown from solution have had lower values reported, typically around 0.02-0.05 cm^2 V^{-1} s^{-1}. [113, 115]

The electron mobility for the complex is lower than that of pure TCNQ, which has been measured as 1.6 cm^2 V^{-1} s^{-1}, but the effective electron mass is two times smaller (0.94 vs. 1.88) along the stacking direction, suggesting that in principle the complex could demonstrate superior mobility assuming comparable phonon scattering. [14]

In principle hole transport should also be possible because the valence and conduction bands are almost equally dispersive, but this is more difficult to achieve due to the presence of deep and shallow trap states where the holes cannot participate in charge transport. [14]

By contrast, the 3:1 complex readily demonstrates ambipolar transport, albeit with significantly lower hole mobility. For crystals grown in solution electron mobility was reported as 0.03 cm^2 V^{-1} s^{-1} with hole mobility of 1.2 $\times 10^{-5}$ cm^2 V^{-1} s^{-1}. [115]

4.4 DBTTF-TCNQ Complexes

4.4.1 Physical Properties

As previously mentioned, TTF based CT complexes typically display a segregated stack structure. However, this is not the case for several DBTTF based complexes. There are two reported polymorphs of DBTTF-TCNQ, which will be referred to as the α and β polymorph, both of which demonstrate a mixed stack structure. While the α

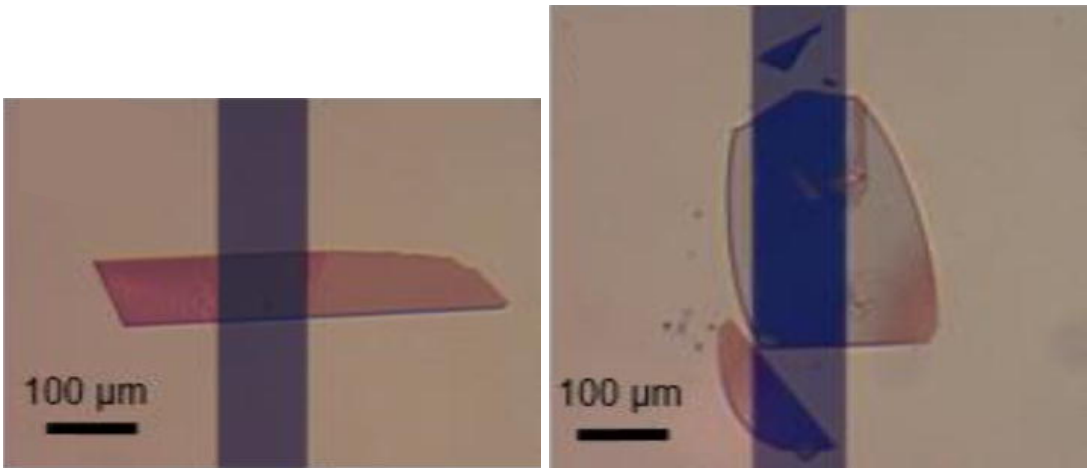

(a) *A crystal of α-DBTTF-TCNQ* ***(b)*** *A crystal of β-DBTTF-TCNQ*

Figure 4-8: *Crystals of both of the known polymorphs of DBTTF-TCNQ. Figure adapted from Goetz* et al. *[32]*

polymorph has been known for some time, the β polymorph was only discovered in 2016 by Goetz *et al.* [32]

The α polymorph has a triclinic structure, with stack of alternative DBTTF and TCNQ along the [001] direction. The structure of β appears to be broadly similar, although it has not yet been fully characterised. Both polymorphs are blue, but the α polymorph forms rectangular or needle-like crystals, and the β polymorph forms oval shapes. [32] (Figure 4-8)

Curiously, there is one paper that reports red DBTTF-TNCQ crystals. It is worth noting that these crystals were produced via an interfacial solvent method using chlorobenzene and acetonirile for the DBTTF and TNCQ respectively. [24] Black crystals have also been reported when grown using aceotnitrile. [60] The blue crystals were grown using physical vapour transport in argon, and therefore are presumably the purest. The black and blue crystals have the same unit cell parameters. This suggests that the "black" crystals may have simply been very dark blue, or that trace solvent impurities led to a slight colour change. By contrast, the reported unit cell for the "red" crystals is markably different, even taking into account different labelling choices for the lattice constants. All the unit cell parameters for DBTTF complexes (as well as pure DBTTF for comparison), including the "red" crystals, are summarised in Table 4.3.

DBTTF-F_2TCNQ also demonstrates a mixed stack structure quite similar to that of α. The largest different is that for DBTTF-F_2TCNQ the layers of each stack are displaced

by approximately half a molecule compared to the layers above and below. [24] It forms black rhomboid crystals. By contrast DBTTF-F_4TCNQ displays a segregated stack structure. It consists of alternating chains of DBTTF and F_4TCNQ. At room temperature both doner and acceptor stacks are dimerised. Along each stack, there are pairs of adjacent molecules stacked almost directly on top of each other when looking down the plane of the stack. Each pair, however, is off-set from one another. [23] Figure 4-9 shows the crystal packing along the (100) and (001) direction for DBTTF-F_4TCNQ while Figure 4-10 shows the view looking down the molecular plane, where the offset nature of the pairs is clearly visible. It forms blue rhomboid crystals.

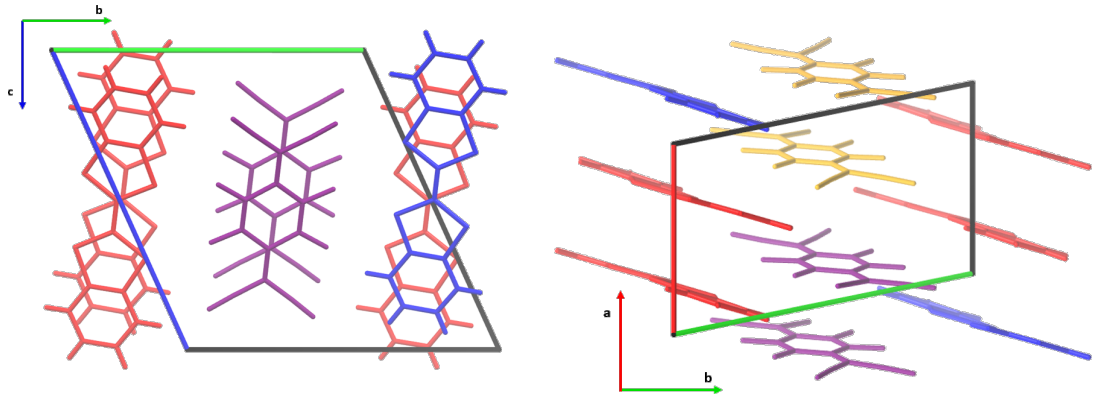

(a) *Unit cell along the (100) direction* ***(b)*** *Unit cell along the (001) direction*

Figure 4-9: *Crystal packing of DBTTF-F_4TNCQ charge transfer crystals along the (100). DBTTF is in red and blue, with one colour for each molecular pair, while F_4TNCQ is in orange and purple.*

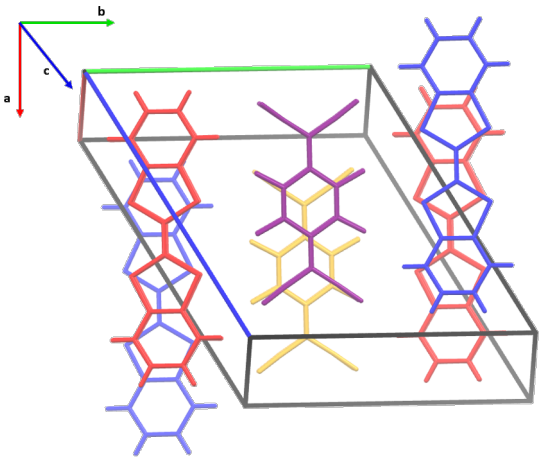

Figure 4-10: *DBTTF-F_4TNCQ viewed down the molecular plane. The paired nature of the unit stacks is clearly visible. DBTTF is in red and blue, while F_4TNCQ is in orange and purple.*

The degree of charge transfer varies, but most complexes demonstrate partial ionicity. For TTF-TCNQ ρ is approximately 0.59. This is somewhat noteworthy, since, as mentioned in Section 2.2.1, many CT complexes are typically either nearly neutral, or close to singly charged. The fact that these complexes are partially charged indicates the influence of the kind of electrical and magnetic excitations reincorporated in the more comprehensive treatment of CT complexes by Strebel *et al.*, [98] alluded to in 2.2.3. In the case of α-DBTTF-TCNQ ρ is 0.46, although the β polymoprh is nearly neutral. [32] For F_2TNCQ ρ increases to 0.65, but by contrast the F_4TCNQ complex is singly charged with ρ=1.0. [24, 23]

Table 4.3: *Crystallographic Data for DBTTF and DBTTF-F_XTCNQ crystals obtained from single crystal x-ray diffraction at room temperature. Data for DBTTF-F_4TCNQ from [23], data for α and β-DBTTF-TCNQ from [32]. All other data from [24].*

.

	DBTTF	"red" DBTTF-TCNQ	α-DBTTF-TCNQ	β-DBTTF-TCNQ	DBTTF-F_2TCNQ	DBTTF-F_4TCNQ
space group	$p2_1/c$	$P\bar{1}$	$P\bar{1}$	Not reported	$P\bar{1}$	$P\bar{1}$
a (Å)	12.08(2)	9.215(3)	7.7576	8.83	8.838(2)	13.159(3)
b (Å)	3.955(1)	10.644(4)	8.3622	9.57	9.276(2)	13.703(4)
c (Å)	14.553(2)	7.734(2)	10.400	6.83	7.794(1)	7.533(2)
α (Å)	90	113.32(3)	83.59	72.14	101.29(2)	102.89(2)
β (Å)	114.36(1)	122.28(2)	109.77	94.99	100.89(1)	105.98(2)
γ (Å)	90	67.66(3)	110.19	88.54	107.42(2)	63.47(2)

4.4.2 Electronic and Spin Behaviour

TTF-TCNQ was the first reported highly conductive CT complex, displaying metallic behaviour over a large temperature range and a maximum conductivity of 1.46×10^4 S cm^{-1} at 66 K [25], almost 20 times higher than the room temperature value of 7×10^4 S cm^{-1}. At around 53 K the complex undergoes a transition to a semi-conducting state and the conductivity falls off rapidly. Shortly after discovery, it was reported by Coleman *et al.* [19] that a small fraction of crystals displayed extremely high conductivity peaks, $\sigma > 10^6$ S cm^{-1}, which they believed to be due to possible high temperature superconductive behaviour. This led to a brief period of research interest, but the results could not be replicated. [9] The behaviour in both states is slightly more complex than either a traditional metal or small gap semi-conductor, and is described in more detail in Section 2.3.

Unsurprisingly, the mixed stack α-DBTTF-TCNQ complex is insulating. At room temperature $\sigma \approx 10^{-6}$ S cm^{-1} for DBTTF-F_2TCNQ.

Despite the segregated stack structure, DBTTF-F_4TCNQ is a Mott-Hubbard insulator, and appears to demonstrate spin-Peierls behaviour. In 1982 Emge *et al.* [23] first reported the structure of DBTTF-F_4TCNQ. They identified that the nature of the structure at low temperatures was due to a spin-Peierls transition. They also tentatively identified the possibility of a high temperature structural transition, believed to be due to Peierls instability. They report, "We have, in fact, evidence from high-temperature, single-crystal x-ray diffraction data for a phase transition near 390 K based on the temperature dependence of the unit volume expansion coefficient [...] [w]e do not, however, have any definitive information as to the structure of the high temperature phase." Ultimately no follow-up studies were carried out and this was never definitively confirmed.

Chapter 5

Experimental Work

5.1 Introduction

In this chapter we look at the specifics of the experiments performed. Unlike Chapter 3, which provided background details and the theoretical underpinnings of the techniques used, this chapter describes the exact equipment and procedures that were carried out and how the precise experimental protocols were developed over time as various improvements and refinements were made.

5.2 Crystal Growth

5.2.1 Materials

Perylene (>99% purity) and DBTTF (97% purity) was obtained from Sigma-Aldrich and TCNQ and its fluorinated derivatives (>98% purity) were obtained from Tokyo Chemical Industry (TCI). These chemicals were then stored in an inert nitrogen atmosphere and protected from direct light.

5.2.2 Furnaces

Preliminary work utilised a Leybold model 12/38/250E two zone furnace under argon atmosphere. Inside the work tube, the starting materials were placed inside 10 cm long glass boats, along with additional empty boats which filled out the rest of the length

of the furnace. This allowed more precise placement of the material inside the furnace and made harvesting of the resultant crystals easier.

While the two zone furnace led to some moderate success, this furnace had an extremely short working length (only 250 mm) and offered relatively little control over the internal temperature profile. Due to the short distance between the two heating elements, it was not possible to achieve a total temperature difference greater than 60° and, by necessity, the temperature gradient was extremely sharp, approximately 9.5° per cm.

Because perylene, DBTTF and TCNQ sublimate at different temperatures, it is important they be placed at different points along the temperature profile to ensure that both starting materials sublimate at the same rate, and the short working length and limited control over the temperature gradient made this difficult to achieve.

The two-zone furnace was replaced by a Carbolite EHC 12/600B three zone furnace, which has a length of 700 mm with an additional 4 mm on either side due to the end cap insulation. This furnace was also equipped with proportional-integral-derivative (PID) controller with a programmable timer and variable ramp rate. The substantially greater length, and the fact it has three heating elements, not two, allowed for much shallower temperature gradients, of around 1° per cm, to be achieved.

Further, the controllable heating rate minimised the risk of the furnace overshooting the set point temperature in the pre-heating stage and the timing controls meant the furnace could automatically deactivate at fixed periods of time after reaching the set point temperature, ensuring consistent and repeatable growth periods, as it did not require human intervention during overnight growths. In order to ensure a stable temperature the furnace was allowed to run under argon for at least 12 hours at the set point temperature before samples were inserted, which also had the benefit of removing any residual moisture and other volatiles. In particular it is extremely important to remove moisture, otherwise it would readily hydrolyse with the cyanonitrile groups on TCNQ.

5.2.3 Pregrowth Preparations

The glass boats were prepared by ultrasonic cleaning in acetone, 2-isoproponal and deionized water to ensure there were no contaminants nor any residue that might serve as unwanted nucleation sites. Initially only a relatively small number of work tubes were available, and so they were also rinsed through between growths to try and remove any chemical residue that might contaminate future growths using different starting

materials. Effective cleaning was somewhat impractical due to the length of the tube, and as more work tubes became available, it instead became common practice to have specific labelled work tubes for each set of starting materials, i.e. one tube dedicated to Perylene-TCNQ and another for DBTTF-F_4TCNQ etc.

Initially, prior to growth, the starting materials were purified by vacuum sublimation in a silicon oil bath at 190° Celsius and then pre-crystallised in the furnace individually before then being combined to grow the charge transfer complex. As described in Subsection 3.2.1, this relatively simple purification step is sufficient to remove any residual low-vapour-pressure molecules, solvent or extremely heavy molecules. It would not be able to separate out organic molecules with extremely similar molecular masses, however, the pre-crystallisation step and actual crystal growth were capable of separating out any such impurities based on the same principles as the more sophisticated carrier gas based sublimation technique.

Further, it was discovered that by lowering the sublimation temperature and increasing the duration it was possible to grow acceptably large crystals on the cold finger itself, eliminating the need for an initial separate pre-crystallisation growth process using the furnace. Using vacuum sublimation it was possible to directly obtain TCNQ crystals of maximum size $3 \times 3 \times 1mm^3$. This did marginally increase the risk of impurities being introduced into the actual crystal growth, however the risk of these impurities being incorporated into the final crystals remained minimal for the reasons mentioned above.

5.2.4 Growth Conditions

Growths were performed under argon, obtained from BOC_UK with a purity of 6 N. Prior to inserting the material, but after placing the work tube and majority of the boats, before inserting the small tubes with the starting materials, the tube in the furnace was subjected to three gas/vacuum purge cycles to further remove any unwanted impurities.

Unfortunately, during initial growths, the TCNQ kept collecting at the start of the furnace. It is believed that this is due to formation of a convection cell that took the starting material to the gas inlet where cold argon was injected. The cold argon would then cause the material to drop out of the gas stream before it could continue to circulate.

Some time was spent adjusting the growth parameters by moving the perylene further

inside the furnace, and then adjusting the heating profile to compensate for the change in position. Ultimately it did become possible to grow adequate crystals, but with an extremely slow sublimation rate. Previous growths had typically taken 48 hours, but after 48 hours with this method, while some crystals had been deposited, the vast majority of the starting material would remain unmoved, and it became clear that a new approach was needed.

The solution was to create a jacketed tube that would constrict gas flow at the start of the furnace. Not only would this prevent the formation of any convection cells in this region, but it would also give time for the incoming argon to heat up. Even if the starting material did move backwards, it would never reach a part of the furnace cool enough to cause it to be deposited. After this jacketed tube was created, growth using the three zone furnace was extremely successful.

5.2.5 Temperature Profiling

A complete temperature profile for the furnace was measured in 1 cm increments using a type K thermocouple with a ceramic insulation tube. (Figure 5-1) The temperature profile was noticeably more stable when the far end of the tube was closed. With both ends of the furnace open it would take at least 10 minutes for the temperature reading to stabilise; with the far end sealed, it would take only five. This suggests that even a relatively minor gas flow is enough to alter the internal temperature distribution of the furnace. Unfortunately, taking temperature measurements while the furnace was in operation under argon was not practical.

The two end heating zones are slaved to the central one, and in principle can only deviate by $\pm 50^{\circ}$. In carrying out the temperature profiling it became apparent that the maximum possible temperature differential was approximately -50° for temperatures below the central heating zone, but closer to $+65^{\circ}$ for temperatures above it.

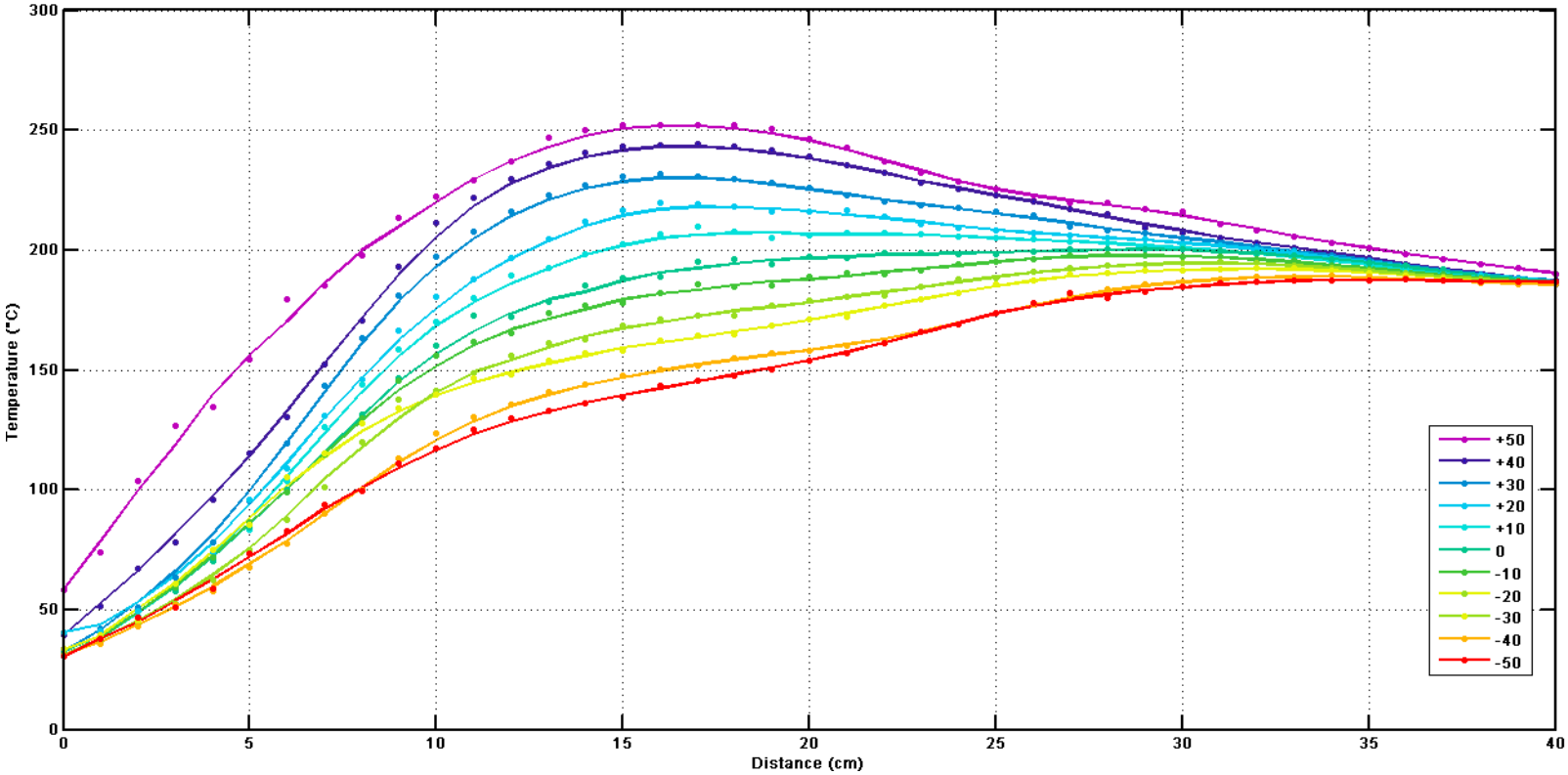

Figure 5-1: *Temperature profile for the three zone furnace, with the endpoint temperature set between -50° and +50°. The central temperature is 185° C degrees throughout. While setting the outer zone to -50° leads to the expected temperature, setting it to +50° in fact leads to a peak approximately +65°.*

5.2.6 Final Growth Parameters

For the pre-crystalisation of perylene, the sublimed perylene powder was placed 2 cm from the gas inlet, with the hot zone at 490 K, the centre of the furnace at 420 K and the cold zone at 380 K. The charge transfer complex was grown using a temperature profile of 480/430/390 K, with the TCNQ placed 15 cm in, and perylene at 25 cm. CT complex growth occurred 30 to 40 cm from the position of the starting materials and formed thin needles with a maximum length of 15 mm after 48 h at constant (1 K) temperature settings. The growth resulted in crystals with different structures, typically α, β, and 3:1 stoichiometry. The abundance of each structure was not assessed and may change with temperature and gas flow settings.

DBTTF-F_4TCNQ were grown using similar conditions. F_4TCNQ was inserted 20-25 cm in, and DBTTF 30-35 centimeters in. The temperature profile was 410/460/510 K. Crystals were deposited from 50 cm onwards.

5.2.7 Crystal Harvesting

The produced crystals were generally extremely fragile and generally extremely small along one or more dimensions (either a needle or a platelet) making direct handling and manipulation difficult. Furthermore, they often came out of the furnace with a high degree of electrostatic charge, causing them not only to clump together, but also to jump onto nearby surfaces.

With care it was possible to extract individual crystals with either a wooden toothpick or glass needle by simply brushing the implement against the crystal and relying on electrostatics to cause the crystal to temporarily adhere to the surface. Using this technique it is also possible to gently manoeuvre the crystals about, but even a minor application of force is enough to break a crystal.

To recover crystals after growth it was possible to use the above method, but a considerably more effective technique involved rinsing the glass boats with solvent using filter paper and a Büchner funnel. This equipment consists of a cylinder with a perforated base that can be connected to a vacuum flask, a thick walled Erlenmeyer flask with a side arm that can be attached to a vacuum pump. This allows for extremely rapid filtering compared so simply letting the liquid drain through the filter through force of gravity and causes the filtride to dry much quicker.

Each boat could then be gently rinsed out by holding it vertically and then applying

solvent to the very top, allowing the solvent to flow down the inner walls, taking the crystals with it. Methanol could be used as neither the starting materials nor the co-crystals readily dissolve in it. Once the crystals had been deposited on the filter paper acetone could also be used as the starting materials dissolve readily in it, but the co-crystals do not. As such, this step could be carried out to remove any residual unreacted starting material. This process also generally had the effect of removing much of the eletrostatic build up, making the crystals easier to subsequently manipulate.

5.3 Data Collection

X-ray data was collected at 150 K using an Agilent SuperNova-E Dual diffractometer equipped with an Oxford Crysosystem using CuKα radiation (λ = 1.5418 Å). Data were processed using the CryAlisPro software (CrysAlisPro 1.171.38.46, Rigaku Oxford Diffraction, 2015). A symmetry-related (multi-scan) absorption correction was applied. This was used to provide unambiguous unit cell determination. The resulting structures were analysed using Mercury [68] and Diamond [43]. Further measurements for DBTTF-F_4TCNQ were carried out by the Advanced Light Source (ALS) at the Lawrence Berkeley National Laboratory.

Infrared spectra of the crystals were recorded with a Bruker ifs66 FTIR spectrometer, equipped with a liquid nitrogen cooled mercury cadmium telluride (MCT) detector and coupled to an Hyperion 1000 IR microscope. This instrument setup allows for both reflection and transmission measurements with polarised light.

Reflectance measurements were obtained using a Cary 5000 spectrophotometer which had been modified by the inclusion of a custom optics array to allow for specular reflectance measurements to be taken. The Cary 5000 has two detectors, a photomultiplier for UV and visible light (down to 175 nm) and InGaAs detector for near IR (up to 3300 nm), with a recommended change-over region of 750-800 nm.

EPR data was recorded using a 9.5 GHz X-band spectrometer as a function of temperature in 5 K intervals up to 300 K. This work was carried out by the Department of Chemical Research Support at the Faculty of Chemistry of the Weizmann Institute of Science.

5.4 Photospectroscopy

Prior to obtaining the IR measurements an attempt was made to carry out reflectance measurements using a Cary 5000 spectrophotometer. Most of the crystals produced had a surface area considerably smaller than that of the default beam spot, 4 mm by 11 mm, meaning that only an extremely small fraction of crystal was contained within the beam path. This resulted in weak signal strength, often near the limits of the detectors' ability to measure.

Masking could be used to compensate for this by reducing the beam width, but this also had the effect of reducing the overall throughput of incident light, resulting in a poor signal to noise ratio since it was typically necessary to cut out 90% of the incident light.

Hence, in order to obtain useful optical data it was necessary to decrease the size of the beam spot by focusing the incident light onto a smaller area. A custom lens and mirror array was created (figure 5-2), which was capable of reducing the beam size to 2 mm wide. Unfortunately this custom reflectance array used silver coated mirrors, which have poor reflectivity below 300 nm due to absorption by bound electrons in what is known as the fundamental absorption edge. As a result it was not possible to collect meaningful data below this wavelength. This is problematic as there should be spectral features below this wavelength associated with perylene and it is preferable to have as broad a spectral range as possible for Kramers-Kronig analysis. [5]

5.5 IR Spectroscopy

In order to probe the high temperature DBTTF-F_4TCNQ transition a series of temperature dependant IR measurements were carried out. This required developing a way of controllably heating the sample holder. The sample holder itself consisted of a flat metal plate with a central hole which housed a removable disc that was designed to hold the actual sample material. (Figure 5-3a) Several bonding agents were tried, but most effective was silver conductive paste obtained from RS Components. The paste was applied to the face of the disc, which was then turned over and pressed gently over the sample crystal. This alleviated the need to directly manipulate the crystals themselves, which were extremely fragile.

The first attempt consisted of a 50 Ω Resistor mounted onto the sample holder that

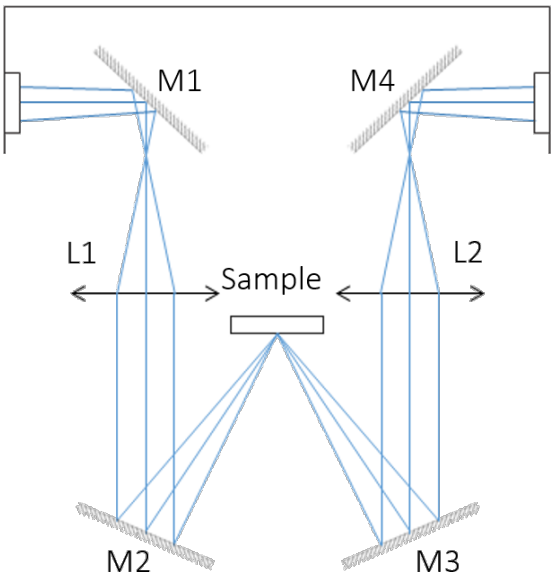

Figure 5-2: *A schematic overview of the custom reflectance array, showing the mirrors M1-4 and lenses L1-2.*

could be connected to an external 30 V 2 A bench power supply using a six pin DIN connector. A thermocouple was then connected to the other side of the sample holder. (Figure 5-4) Unfortunately the set up was only able to archive a maximum temperature of 376 K, far below the expected transition point near 400 K. Switching to a 5 Ω resistor did allow temperatures of 400 K to be reached, but caused the resistor to break after prolonged use. The first resistor began to suffer performance degradation during testing before failing completely and the second exploded during initial heating. Likewise, the standard cable connecting to the resistor failed and so was replaced with fibreglass insulated cabling. Finally a more heavy duty heating element was installed instead of the standard resistors, which was able to sustainably take the sample holder up to 400 K.

A temperature/current profile was obtained for the maximum temperature obtained for a given input current in 0.05 A steps up to 400 K. Ideally it would have been preferable to record several temperatures above this point, but in vacuum the DBTTF-F_4TCNQ crystals sublimated at temperatures just above 400 K. (Figure 5-5) Temperature measurements were recorded every five minutes and it was determined that the maximum temperature had been reached after at least 25 minutes had passed and the temperature increase was less than 0.5°.

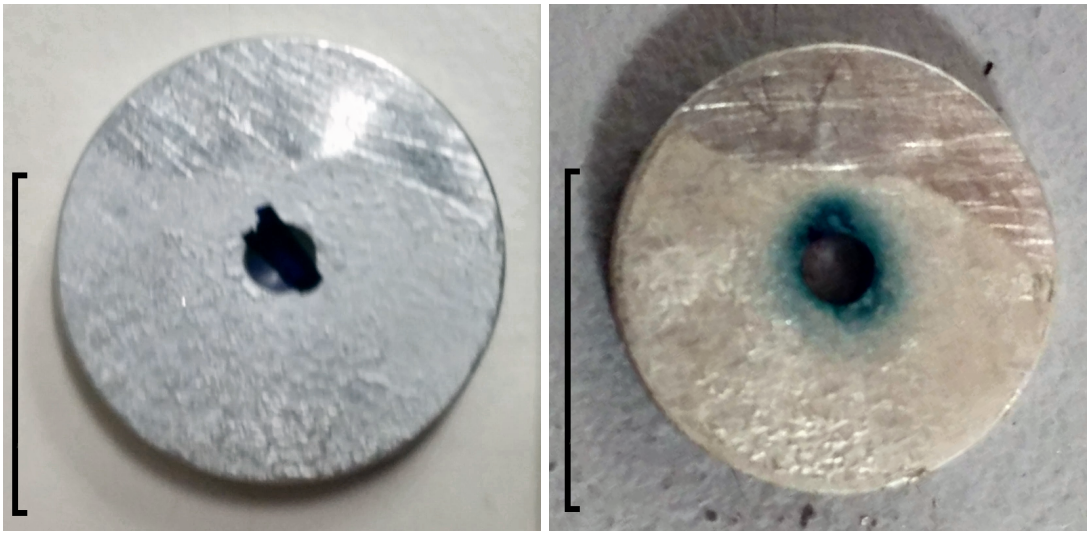

(a) *A DBTTF-F_4TCNQ Crystal mounted onto the sample holder disc with silver paste* ***(b)*** *The same sample disc after being heated to 400 K while under vacuum*

Figure 5-3: *The central disc of the sample holder. The textured area on the lower half of the disc shows the dried silver paste used to mount the sample. The scale bar is 1 cm long.*

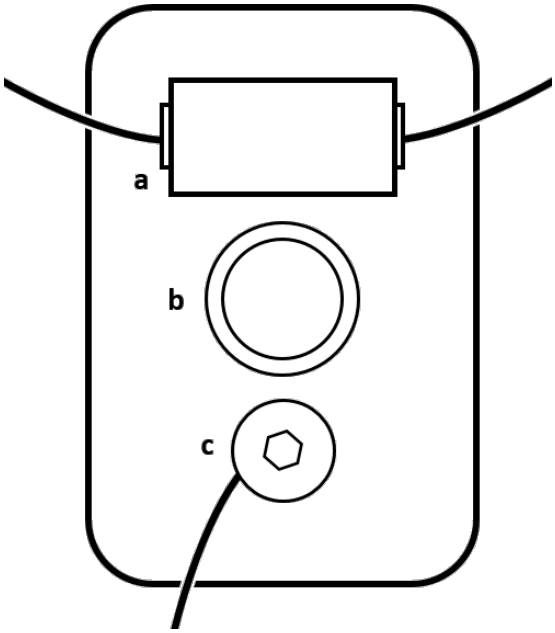

Figure 5-4: *A schematic of the modified sample holder. (a) the heating element (b) sample disk holder (c) thermocouple.*

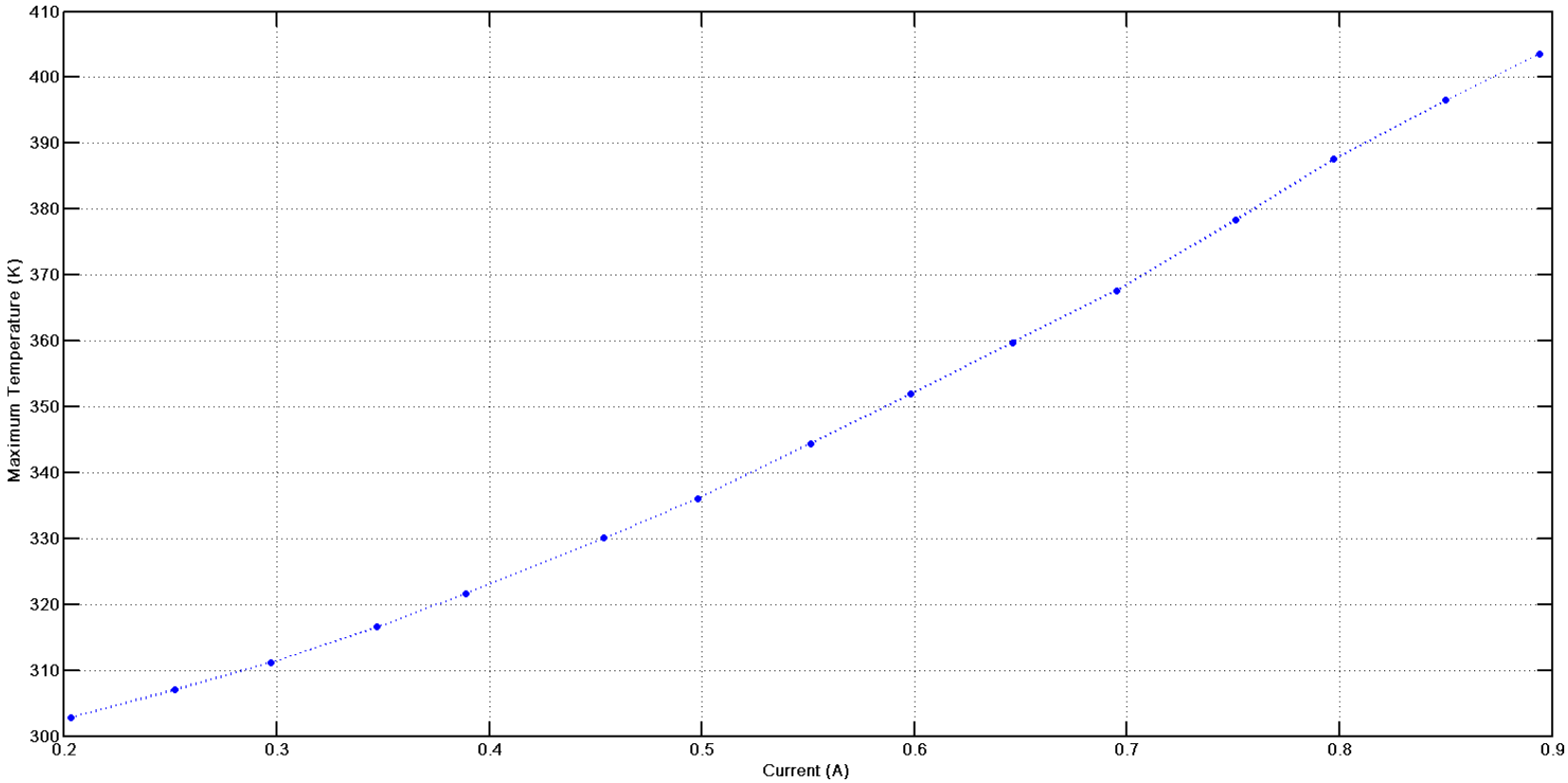

Figure 5-5: *The final heating profile obtained.*

Once the maximum temperature/current relationship had been obtained, it was then used to calculate the current required to perform IR measurements from 300 K to 400 K in 5° intervals.

Chapter 6

Discovery of a Novel Polymorph of Perylene-TCNQ

6.1 Introduction

In this chapter we describe the first set of experimental results obtained. During growth of perylene-TCNQ in the three zone furnace, two new polymorphs with a 1:1 stoichiometry were discovered in addition to the previously reported monoclinic structure, [89, 41, 103, 44, 7] which we designate as α. (CCDC: PERTCQ) The two novel structures, which we designate β and γ and their properties were reported in *Crystal Growth & Design.* [36]

6.2 Structural Properties

Before describing these novel structures, it is first instructional to describe α. Table 6.1 summarizes the crystallographic parameters for the previously reported polymorph and the two new structures.

α is monoclinic, with a space group $P2_1/c$, and with two molecules per unit cell. The molecules in the stacks are not parallel, but offset by an angle of 4.26°. As such it is not possible to quote a direct distance between the molecular planes, but the distance between the perylene plane and the centroid on TCNQ is 3.334 Å, following the convention used by Salzillo *et al.* [89] While this value is representative of the inter-planar spacing it is also a fairly arbitrary convention (it would be just as valid to measure the

distance between the TCNQ plane and the centroid for perylene, which would result in a slightly different value). As such, uncertainties for these measurements are not reported as they would be misleading. The molecules themselves are not aligned directly over each other, but have a centroid to centroid offset of approximately 1.36 Å. This offset is measured by the distance between the centroid of the perylene molecule to the perpendicular projection of the centroid of TCNQ onto the mean plane of the perylene molecule. These measurement conventions are used for all subsequent structures.

β is also monoclinic with space group C2/c. Compared to α the unit cell is substantially larger and contains eight molecular pairs per unit cell. At around 280 K this polymorph undergoes a symmetry-breaking phase transition, losing the C-centering and transforming to its primitive reduced cell. This polymorph, γ, is triclinic with $P\bar{1}$ symmetry and four molecular pairs per unit cell. Structurally, both new polymorphs consist of two different types of alternating stacks, which, for convenience, we refer to as S-I and S-II, as shown in Figure 6-1.

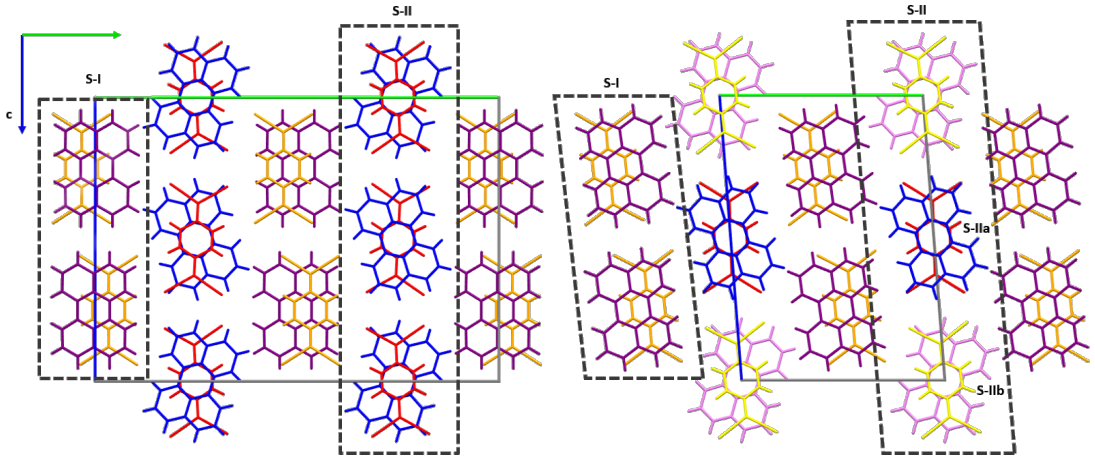

(a) *β* ***(b)*** *γ*

Figure 6-1: *Crystal packing of Perylene-TNCQ charge transfer crystals along the (100) direction. The two different stacks, S-I and S-II, are indicated by the dashed outlines. The unit cell is identified by the solid coloured lines.*

In the case of the β polymorph the S-I stack consists of perylene and TCNQ molecules that are offset by approximately 1.95 Å. By contrast the molecules in S-II are almost directly on top of each other, with an offset of less than 0.5 Å. Likewise, while in S-II adjacent stacks are slipped by one molecule along the a-axis, similar to the structure of the F_2TCNQ complex, the S-I stacks are not. This feature is most obvious when viewed along the c axis, shown in Figure 6-2.

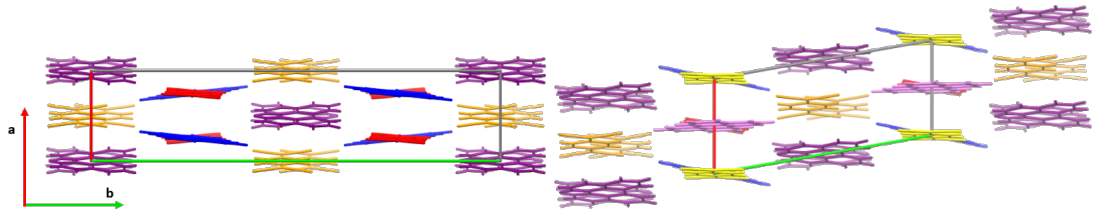

(a) β *(b)* γ

Figure 6-2: *Crystal packing of Perylene-TNCQ charge transfer crystals along the (001) direction. The unit cell is identified by the solid coloured lines.*

As with the previously reported structure, α, the molecules in the stacks are not perfectly parallel, but are offset by an angle of 0.15(3)° and approximately 2.15(4)° respectively. The inter-planar spacing is 3.409 Å and 3.383 Å. One of the most unusual features of this system is the presence of highly distorted perylene molecules. In both gas phase and in other crystalline structures, perylene is highly planar. However, for the S-I stacks the angle between the two naphthalene moieties of the molecule is 6.24(5)°. This may in part explain why the inter-planar spacing for S-I is larger than for S-II, and has an impact on ρ.

The structure of γ is, perhaps unsurprisingly, superficially similar to β. It too possesses S-I and S-II stacks, with the S-I stack exhibiting a large centroid to centroid offset and distorted perylene molecules. The S-II stacks, by contract, now consist of two symmetrically non-equivalent molecular chains, S-IIa and S-IIb. The largest difference can be seen when the structure is viewed along the c-axis, as the unit cell is now triclinic.

The two S-II stacks display a slightly different alignment of the TCNQ and perylene long molecular axis (C_2 symmetry). For the β polymorph, this angle is 20.26(4)°. For S-IIa this angle has decreased to 18.22(4)°, but for S-IIb it has increased to 21.88(5)°. The interplanar spacing has also diverged to 3.352 and 3.389 Å respectively, as well as the angles between molecular planes, which is now is 2.06(4)° and 2.31(5)°. For both β and γ the smaller the deviation from parallelism, the smaller the misalignment along the long C_2 molecular axes. This suggests that the deviation from perfect parallelism between the molecular planes is related to the misalignment of the long C_2 molecular axes.

For the S-I stacks the spacing between perylene and TCNQ has increased slightly to 3.410 Å, and the angle between the molecular planes has also increased to 0.53(4)°. The perylene molecules in the S-I stacks demonstrate a slight shift parallel to the short

C_2 molecular symmetry axis and the angle between the napthalene component of the distorted perylene molecule is now only 6.14(6)°.

Further cooling of the γ polymorph to 150 K does not result in any further phase transitions, but only smaller changes in intermolecular differences and an even greater divergence between the S-IIa and S-IIb stacks. The unit cell parameters together with other relevant crystallographic data, such as cell volume, are reported in Table 6.1. The interplaner distance is now 3.287 Å for S-IIa, and 3.367 Å for S-IIb. As expected, both of these values are smaller than at 270 K. Interestingly, the angle between the molecular planes increases to 2.17(3)° and 2.65(4)°. For S-II, the interplanar distance has decreased to 3.375 Å, the angle between molecular planes has increased to 1.03(4)° and the perylene distortion has increased to 6.24(5)°. From this, it would appear that shorter donor acceptor distances lead to a greater deviation from parallelism, likely due to steric hindrance.

Table 6.1: *Crystallographic Data for Perylene-TCNQ crystals obtained from single crystal x-ray diffraction. Z indicates the number of molecular pairs per unit cell.*

	α	β	γ	γ
Temperature (K)	290(2)	290(2)	270.01(10)	150.00(10)
crystal system	monoclinic	monoclinic	triclinic	triclinic
space group	$p2_1/c$	$C2/c$	$P\bar{1}$	$P\bar{1}$
a (Å)	7.29888(2)	6.8315(11)	6.8315(11)	6.7477(3)
b (Å)	10.8741(2)	30.944(5)	15.7910(12)	15.6571(9)
c (Å)	14.5519(3)	21.932(5)	21.9339(13)	21.8347(12)
α (Å)	90	90	86.135(5)	84.268(4)
β (Å)	90.254(2)	97.913(19)	82.172(5)	82.234(4)
γ (Å)	90	90	78.283(6)	79.390(4)
cell volume (Å^3)	1153.94(4)	4592.1(15)	2287.7(3)	2239.9(2)
Z	2	8	4	4
reflections collected	7288	13845	15633	13081
independent reflections	2281	4556	8922	8149
R indices	$R_1 = 0.0423$	$R_1 = 0.0660$	$R_1 = 0.0614$	$R_1 = 0.0663$
($I > \sigma(I)$)	$wR_2 = 0.1178$	$wR_2 = 0.1457$	$wR_2 = 0.1519$	$wR_2 = 0.1583$
R indices	$R_1 = 0.0476$	$R_1 = 0.1200$	$R_1 = 0.1011$	$R_1 = 0.1167$
(all data)	$wR_2 = 0.1228$	$wR_2 = 0.1853$	$wR_2 = 0.1821$	$wR_2 = 0.2078$
GooF	1.033	1.024	1.017	1.025
CCDC no.	1576698	1576699	1576700	1576701

6.3 Reflectance Measurements

The spectrophotometer was successfully modified to allow for specular reflection measurements to be taken. A sample of tetracene was used as a known trial candidate to test the functionality of the new lens array. Spectral features were clearly visible, notably the major peak at 520 nm, and the smaller peaks at 480 and 450 nm which correspond to the ground exciton transition and the transition to the first and second vibrational excited states respectively. These features could not be resolved using the default reflectance configuration. Once the modifications had proved effective, a spectrum of the

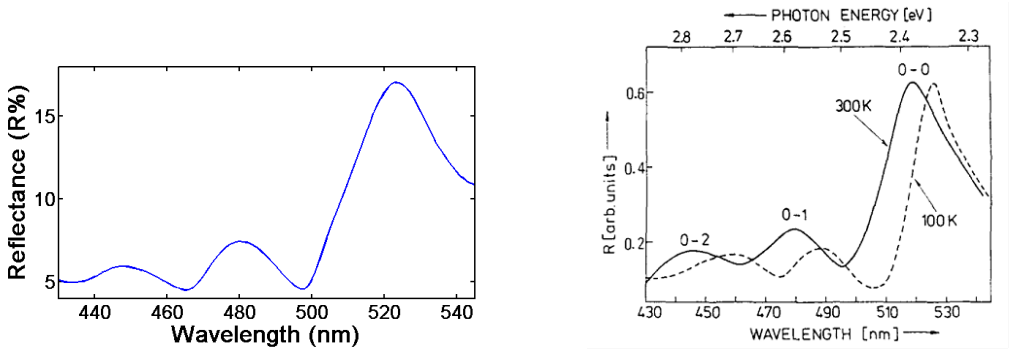

(a) *Reflectance spectrum for a test sample at 300 K. The 0-2, 0-1 and 0-0 peaks are clearly visible.*

(b) *Literature spectrum, as reported by Gliński and Kalinowski. [30]*

Figure 6-3: *Reflectance spectrum for a test sample of tetracene, compared to literature values.*

[100] face of the 3:1 single crystal sample was taken and Kramers-Kronig transforms were applied to extract refractive index data. This reflection spectrum matches literature values, displaying the presence of a charge transfer band at 1000 nm with a weak shoulder at 800 nm and the neutral perylene band at 450 nm.

6.4 Inter-molecular Interactions

In addition to the CT interaction, there are several other noteworthy inter-molecular interactions. Figures 6-4 and 6-5 show all short contacts for which the sum of the vDW radii is less than 0.1 Å. These atoms are close enough to each other to directly interact via dispersion, dipole-dipole and various other inter-molecular forces. It would be wrong to generally refer to these as bonding interactions, as they are not necessarily energetically favourable.

Notably, for both polymorphs these interactions are between S-I and S-II molecules and not intrastack and the S-II short contacts are only between TCNQ molecules, while the S-I stacks also display interactions with perylene. For β there are two C-H$\cdots$N short contacts between each peryelene and the TCNQ molecules of both adjacent S-II stacks. Since the two TCNQ molecules are staggered, with one lying below the peryelene, and one above, these short contacts may go some way to explain deviation from planarity. For γ the interactions between S-I perylene molecules and the adjacent TCNQ molecules are weaker, and instead there are short contacts with other S-I peryelene molecules. This may explain why the distorted perylene molecule is more planar for γ when compared to β.

There are further C-H$\cdots$N short contacts between the cynao group of the S-I TCNQ molecules and one of the aromatic C-H on S-II TCNQ. This may compete with the S-I intrastack $\pi - \pi$ interactions between perylene and TCNQ.

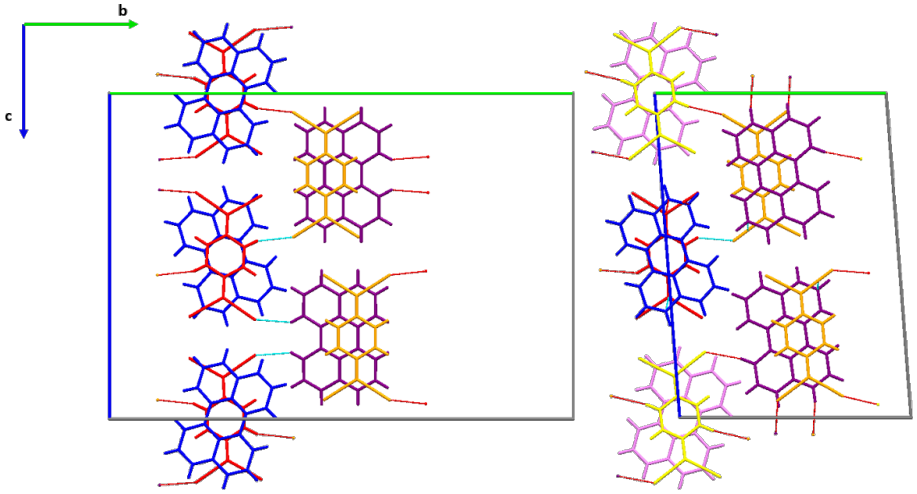

(a) β ***(b)*** γ

Figure 6-4: *Crystal packing of Perylene-TNCQ charge transfer crystals showing short contacts where the sum of vDV radii is at 0.1 Å, along the (001) direction. Hanging contacts are in red, expanded contacts in cyan.*

6.5 Evidence of a Phase Transition

To confirm that reconfiguration from β to γ was in fact a proper phase transition and not simply an irreversible structural change a variable temperature parametric study was carried out. The crystals cooled in situ inside a diffractometer, with cooling

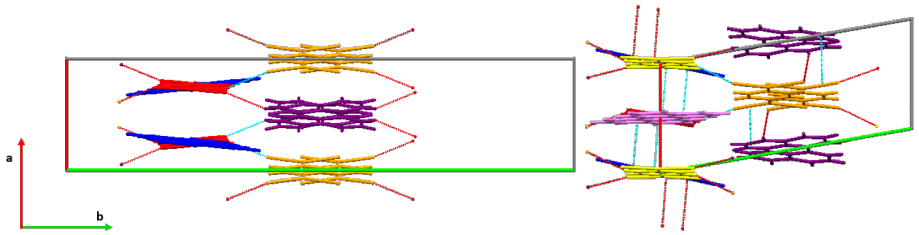

(a) *β* ***(b)*** *γ*

Figure 6-5: *Crystal packing of Perylene-TNCQ charge transfer crystals showing short contacts where the sum of vDV radii is at 0.1 Å, along the (100) direction. Hanging contacts are in red, expanded contacts in teal.*

paused at regular intervals to allow unit cell determinations. The sample was then heated again, to determine whether the changes were reversible.

During the transition the crystal converts from a monoclinic structure to a triclinic, which can radically alter the unit cell parameters, even if the actual change in crystal structure is relatively minor. Therefore, to enable direct comparison, the data was indexed using the triclinic primitive unit cell for all temperatures. The results, shown in Figure 6-6, show a clear change at 280 ± 10 K. Most notable is the abrupt discontinuity in the b axis and the sudden gradient change (representing an abrupt change in temperature dependence) in the c axis and α angle.

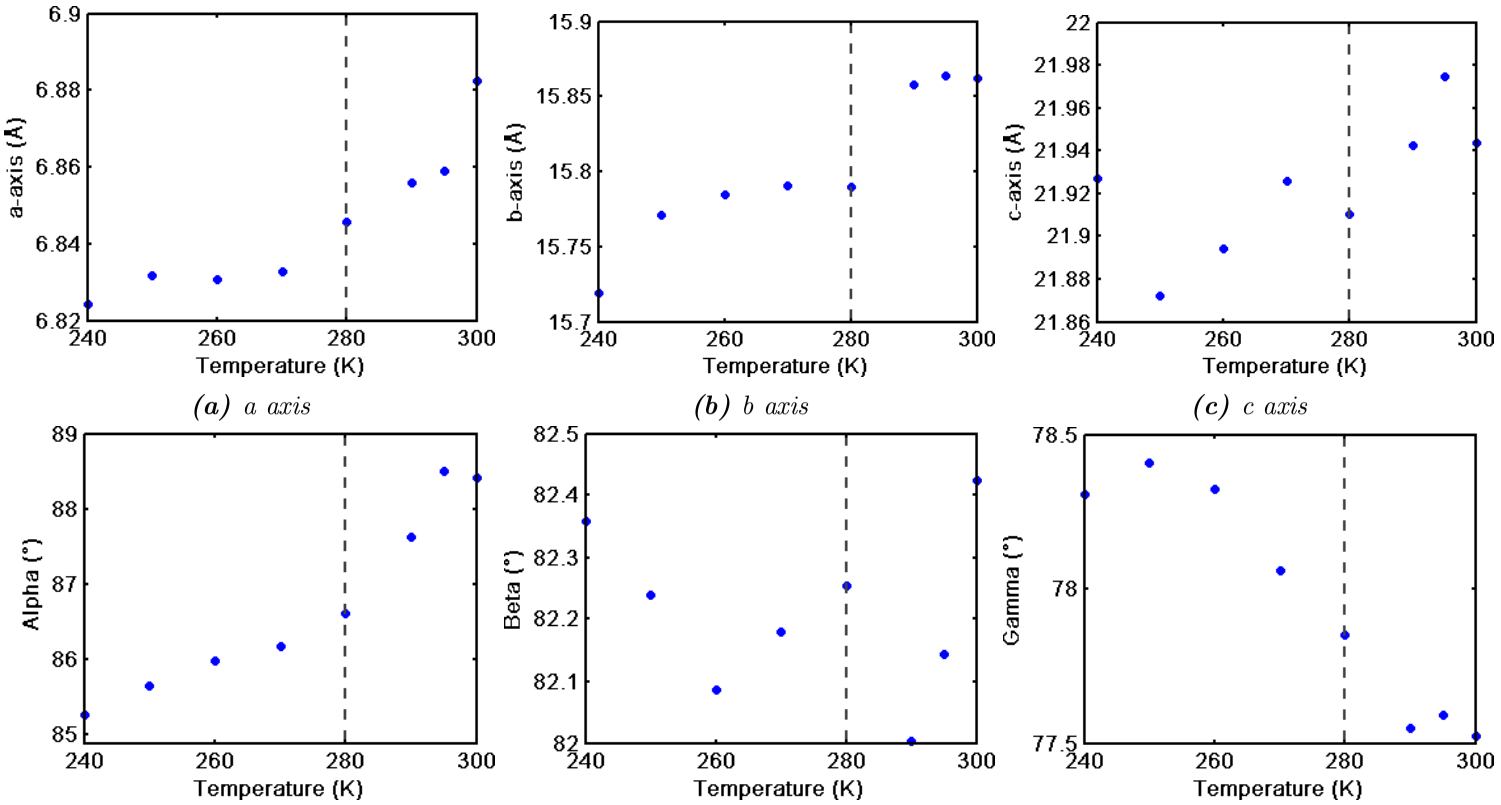

(a) *a axis* ***(b)*** *b axis* ***(c)*** *c axis*

(d) *α angle* ***(e)*** *β angle* ***(f)*** *γ angle*

Figure 6-6: *Unit cell parameters as a function of temperature for a γ single crystal. The structure has been refined with a* $P\bar{1}$ *space group in the whole temperature range.*

A differential scanning calorimetry (DSC) study was also carried out in order to better probe the phase transition, but, as shown in Figure 6-7, the sweep did not show any discernible features indicative of a phase transition. One possibility is that the DSC sample, which requires a substantial amount of material, was a hetrogeneous mixture, including α and 3:1 polymorph crystals. Since these do not undergo a phase transition, they would swamp any signal. Furthermore, while there are distinct structural differences between the β and γ polymorphs, the changes are relatively small, and may not result in an appreciable variation in thermodynamic properties.

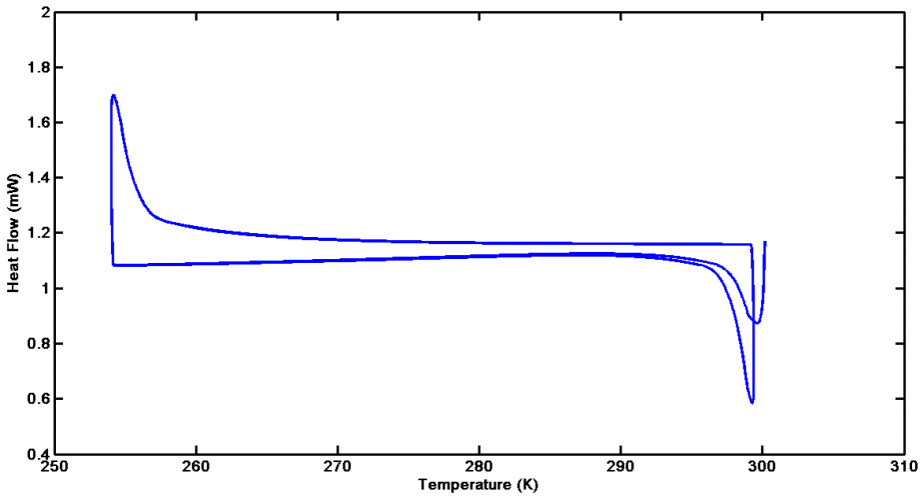

Figure 6-7: *A differential scanning calorimetry sweep across the phase transition between β and γ for Perylene-TCNQ single crystals.*

Complete diffraction data for a [h,0,l] slice through a single crystal was taken at 280 K and 300 K, which further confirms the presence of a symmetry breaking phase transition. For a C-centered cell we would only expect to see reflections where the Miller indices satisfy the condition h + k = n2, and therefore it should contain half as many reflections as a P-cell. As shown in Figure 6-8 this is the case, and confirms that the crystal system is changing from C2/c to p$\bar{1}$.

6.6 Degree of Charge Transfer

Using the HOSE method, α has an estimated ρ of 0.09, and using the constants reported by Herbstein and Kapon [39] gives a value of 0.11. This is somewhat larger than the reported literature value of 0.01±0.07. By contrast, using the constants reported by

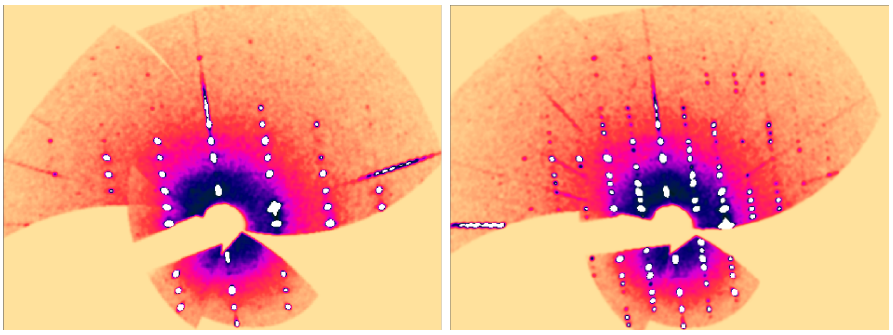

(a) *300 K* ***(b)*** *280 K*

Figure 6-8: *Diffraction pattern of a [h,0,l] layer perylene-TCNQ*

Graja [3] yields a value of 0.03. These values, and those of β and γ, are summarised in Table 6.2.

Two of the ρ calculations yield positive values when calculated using HOSE, which superficially indicates that there is a positive charge present on TCNQ. This is unlikely given TCNQ's extreme electronegativity and the respective HOMO and LUMO energy levels. These calculations also yield extremely high values using the bond length method. It is far more likely that the TCNQ molecule in question is being distorted due to some other process which is confounding both sets of calculations. There is a single instance where the bond length method, using the constants from Graja, also yields a positive value, but this is more likely due to the inherently large uncertainties in ρ estimates for near neutral CT complexes.

Overall, as with α, both the β and γ polymorph appear to be near neutral CT complexes. As such is it more difficult to accurately estimate ρ and it would therefore be unwise to read too much into the exact calculated values. However it is noteworthy that once again the structure of β and γ appear to be dominated by the interplay between CT interactions and other intramolecular forces, that, in this case, are distorting the bond lengths of TCNQ molecules.

Table 6.2: *Charge transfer calculations for Perylene-TCNQ polymorphs. ρ is a scalar property, however, values that indicate a net positive charge on TCNQ have been indicated with a *.*

		HOSE	Herbstein & Kapon [39]	Graja [3]
α		0.09	0.11	0.03
β (290 K)	S-I	0.09	0.23	0.13
	S-II	0.04*	0.43	0.33
γ (270 K)	S-I	0.19	0.01	0.06*
	S-IIa	0.05	0.19	0.10
	S-IIb	0.11	0.10	0.02
γ (150 K)	S-I	0.02	0.29	0.19
	S-IIa	0.04	0.22	0.13
	S-IIb	0.03*	0.36	0.25

Chapter 7

Discovery of a High Temperature Spin Transition in DBTTF-F_4TCNQ

7.1 Introduction

In this chapter we describe the second set of experimental results, the investigation of a structural transition in DBTTF-TCNQ. We first examine the high temperature changes that occur close to 400 K, as determined by both x-ray crystallography and IR spectroscopy. We then briefly explore the phenomena that occur at low temperature, based on Electron Paramagnetic Resonance (EPR), x-ray crystallography and reflectance spectroscopy.

7.2 Structural Properties

It is once again instructional to describe the structure of DBTTF-F_4TCNQ before discussing any structural transitions. The CT complex is a segregated stack system, comprising of parallel chains of DBTTF molecules and of -F_4TCNQ molecules. Within each chain, the F_4TCNQ molecules are "paired up" or dimerised. For any given three sequential molecules, two of them will have a much smaller centroid to centroid overlap (defined below), while the third molecule will be shifted sideways with respect to stack direction. Figure 7-1 shows the crystal structure along the (100) and (001) directions

while Figure 7-2 shows these molecular pairs quite clearly.

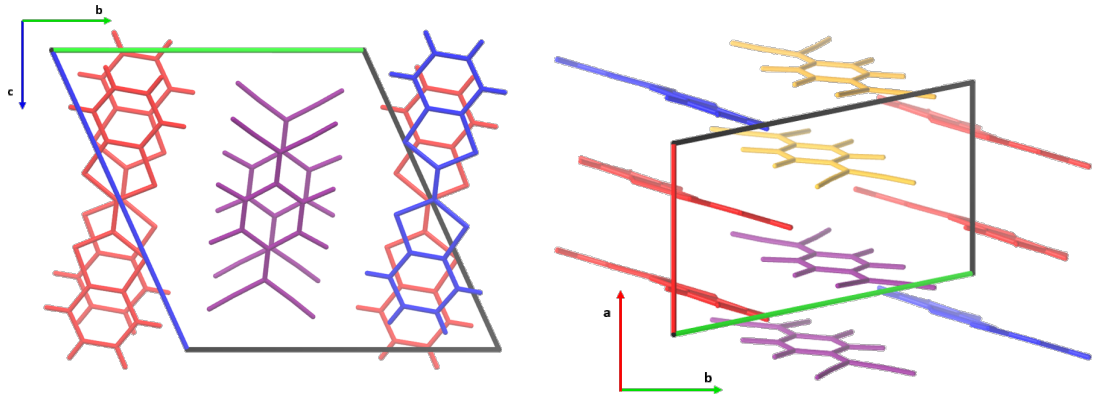

(a) *Unit cell along the (100) direction* ***(b)*** *Unit cell along the (001) direction*

Figure 7-1: *Crystal packing of DBTTF-F_4TNCQ charge transfer crystals along the (100) axis. DBTTF is in red and blue, with one colour for each molecular pair, while F_4TNCQ is in orange and purple.*

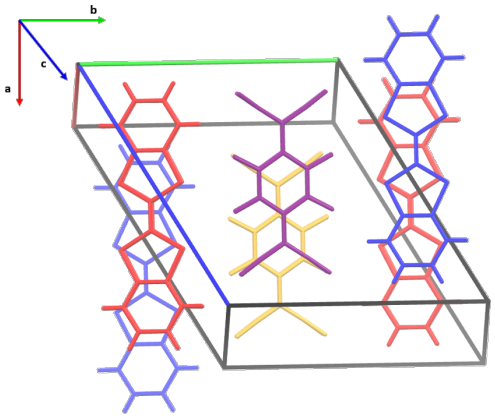

Figure 7-2: *DBTTF-F_4TNCQ viewed down the molecular plane. The paired nature of the unit stacks is clearly visible. DBTTF is in red and blue, while F_4TNCQ is in orange and purple.*

For the F_4TNCQ pairs, they have a greater centroid-centroid overlap, as defined, and are also closer together. At room temperature, the distance between the dimerised molecules is 3.283 Å (the intra-pair distance), and 3.454 Å to their nearest neighbour (the inter-pair distance). The molecules are parallel to one another, so these values are calculated by simply measuring the distances between the two molecular planes. The intra-pair centroid-centroid overlap is 0.638 Å and the inter-pair overlap is 3.167 Å. This value is calculated as the distance between the centroid of the first molecule, as projected onto the plane of the second molecule, to the centroid of the second. For

DBTT, the intra-pair and inter-pair distances are 3.526 Å and 3.475 Å respectively. The intra-plane centroid-centroid distance is 0.659 Å and the intra-plane distance is 2.83 Å. Thus we can clearly see that each molecular pair has a very high overlap.

It is worth noting that the choice of which two molecules comprise a "pair" is somewhat arbitrary. In fact, due to the nature of $\pi - \pi$ interactions described in Subsection 2.2.4 the interpair interactions are stronger than the intrapair interactions. Here the choice of pairing is simply for visual clarity. It is easier to show the offset nature of the molecular stacks of both the molecules if the molecular pairs are defined in terms of the greatest centroid-centroid overlap.

7.3 The High Temperature Regime

7.3.1 X-ray Crystallography

An initial set of x-ray measurements were carried out at 300, 370, 390 and 400 K, which suggested a possible change in ρ near 400 K, as demonstrated by both HOSE and the Kistenmacher method, as shown in Figure 7-5a. A second more detailed set of x-ray measurements were then carried out between 300 K and 425 K at 10 K intervals to better probe any structural changes. Near the proposed transition point measurements were taken at 5 K intervals.

The x-ray measurements also confirmed the presence of a structural transition at around 395 K. In absolute terms, the shift is rather subtle compared to structural changes demonstrated by peryelene-TCNQ in Chapter 6, which resulted in the complex shifting between a monoclinic and tri-clinic unit cell. The shift can primarily be seen as a discontinuity in the unit cell parameters as well as the distance and angle between dimer pairs as temperature is increased. Figure 7-1 shows the unit cell parameters. The suspected structural shift can most clearly be seen in the change in "gradient".

Figure 7-4 shows the inter and intrastack planar distances for both DBTTF and F_4TNCQ as a function of temperature. For clarity, it also shows the relative interplanar distance. This is simply an expression of the ratio of the two distances, expressed in percentage form. As temperature increases, the relative difference in intrastack and interstack distances decreases, almost approaching a even ratio of 50%. A "jump" at around 390 K can clearly be seen.

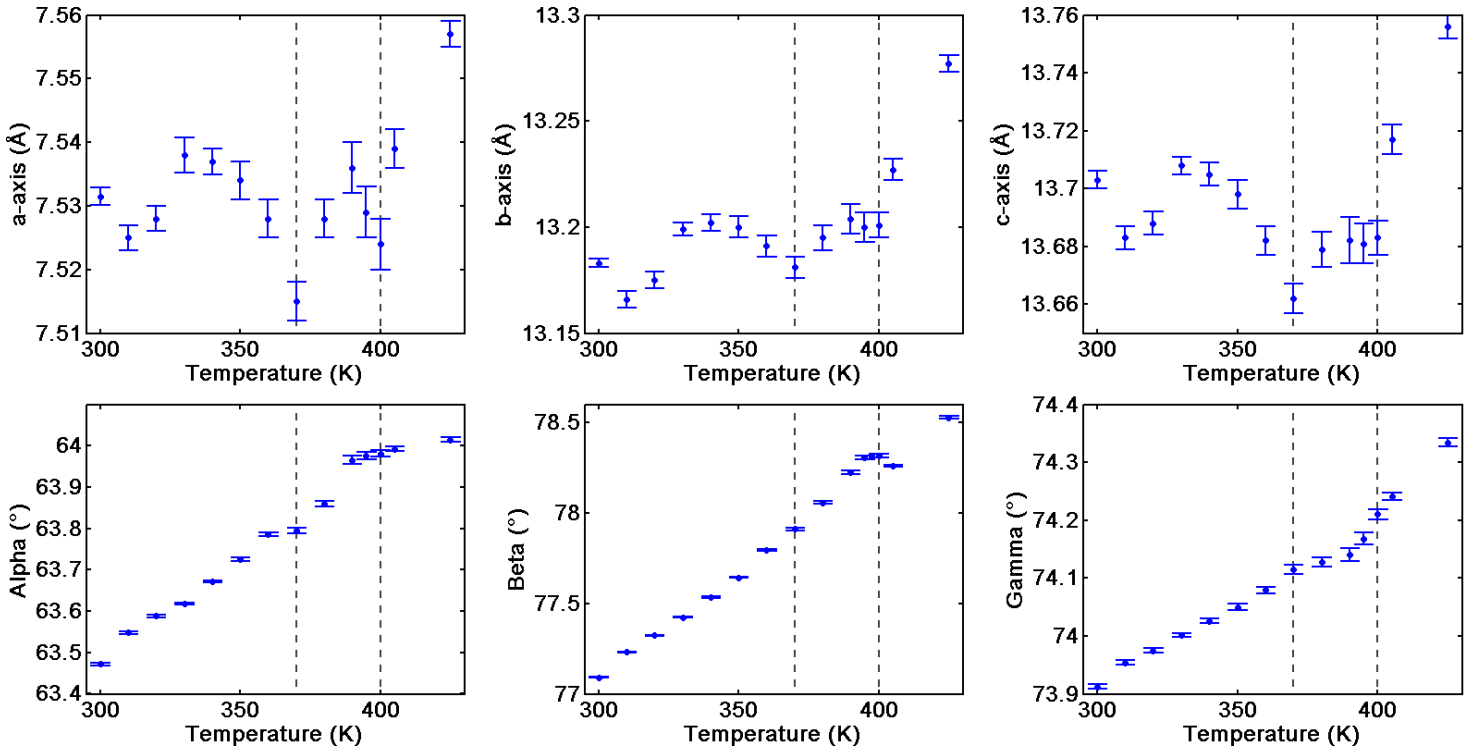

Figure 7-3: *The unit cell parameters for DBTTF-F_4 TCNQ. There appears to be a structural shift just below 400 K and another possible shift at 370 K.*

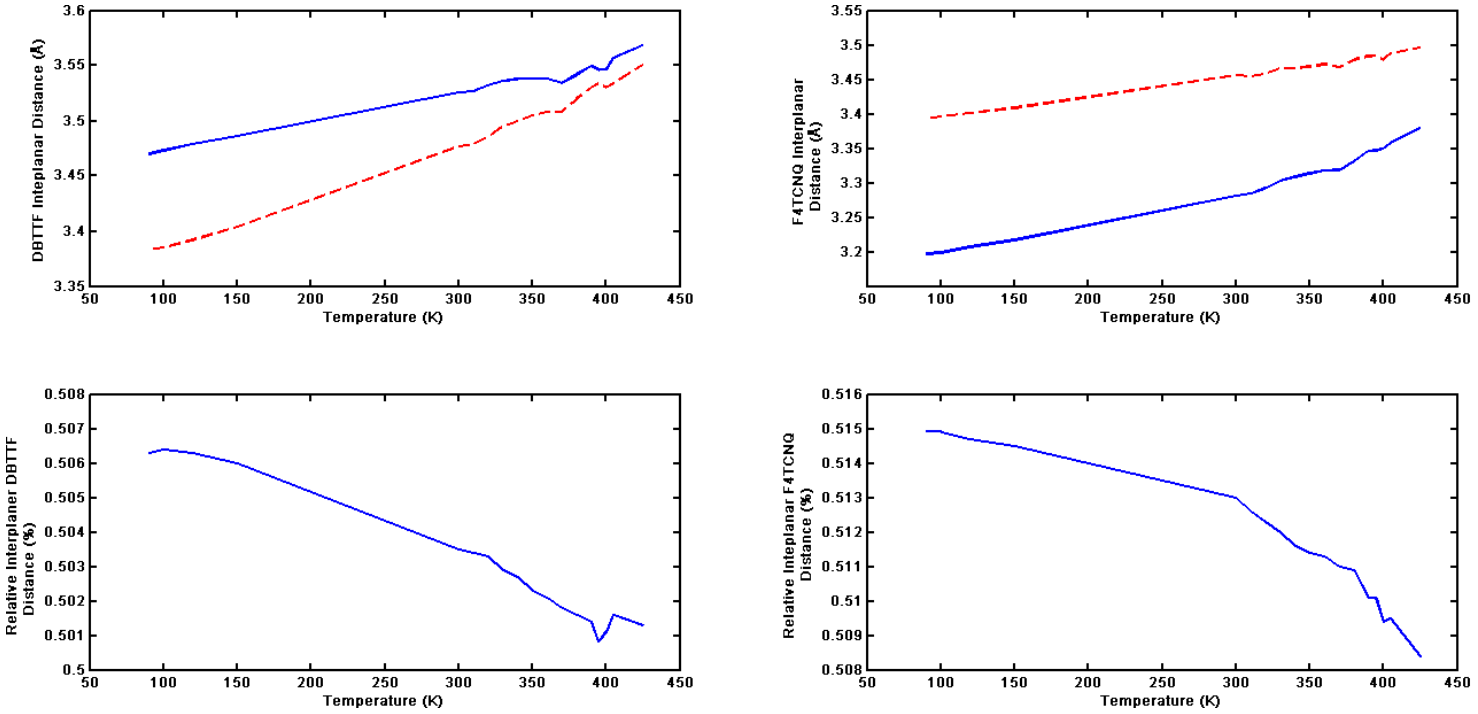

Figure 7-4: *Top: The interstack (blue) and intrastack (red) distance for DBTTF and F_4TCNQ. Bottom: The ratio of these two distances, represented as a percentage of the combined total. If the structure were completely undimerised, the relative distance would be 50%.*

Perhaps ironically, while the additional and more detailed set of measurements confirmed that there was a high temperature structural shift, it cast doubt on the presence of a corresponding change in ρ. Both the HOSE and Kistenmacher method were used again, as well as the proposed method for estimating the degree of charge in the DBTTF molecule described in Subsection 3.3.3. The results from HOSE and Kistenmacher were extremely noisy. Broadly, they showed that ρ was quite close to one, as expected, but the precise values fluctuated randomly over the temperature range. This can be seen in Figure 7-5a. The estimation methods based on DBTTF bond lengths were even worse, with ρ seemingly varying between 1.30 and 0.9, with no correlation with temperature.

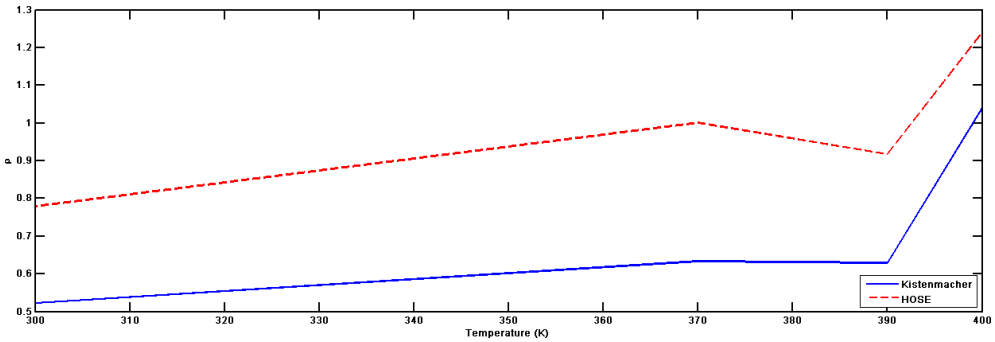

(a) *The initial ρ estimates for DBTTF-F_4TCNQ, with both the Kistenmacher and HOSE method. There appears to be a possible transition near to 390 K.*

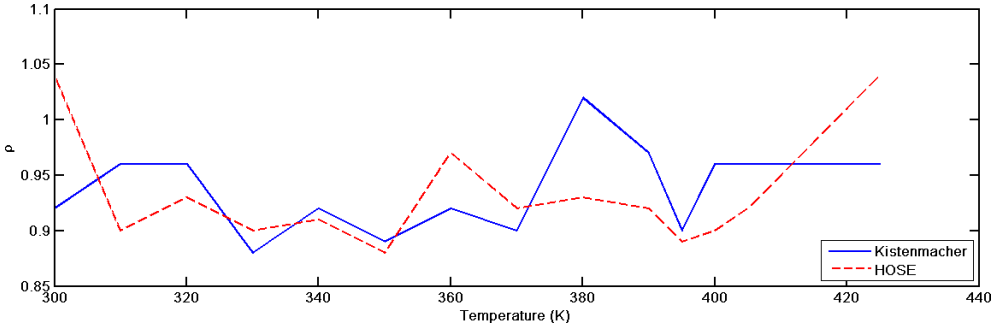

(b) *ρ estimates for DBTTF-F_4TCNQ, with both the Kistenmacher and HOSE method, after a more detailed set of measurements. There is no discernible transition.*

Figure 7-5

As discussed in previous sections, these bond-length based methods are unreliable at the best of times. As such, these results tell us very little; the uncertainties are simply too high. From this data there does not appear to be any temperature dependant changes, although it is impossible to rule out the possibility that there is a slight change in ρ that accompanies the structural shift. These techniques are simply not precise enough. As such, we turned to infra-red spectroscopy in an attempt to better estimate ρ.

7.3.2 IR Measurements

As with perylene-TCNQ it is possible to estimate ρ by examining the frequencies of the C=C stretching modes compared to neutral F_4TCNQ. A series of measurements were carried out between 300 K and 400 K to determine whether there was any noticeable change in ρ around the transition point. (Figure 7-8) The relevant peaks were then fitted to Gaussian functions to determine how they varied with temperature. Four terms were used, corresponding to the peak and shoulder at around 1526 and 1535 cm^{-1}, the peak at 1630 cm^{-1} and a final term to account for baseline features. Figure 7-6 shows an example fitting, and figure 7-7 a plot of the centre, Full Width at Half Maximum (FWHM) and amplitude of the resultant fittings as a function of temperature.

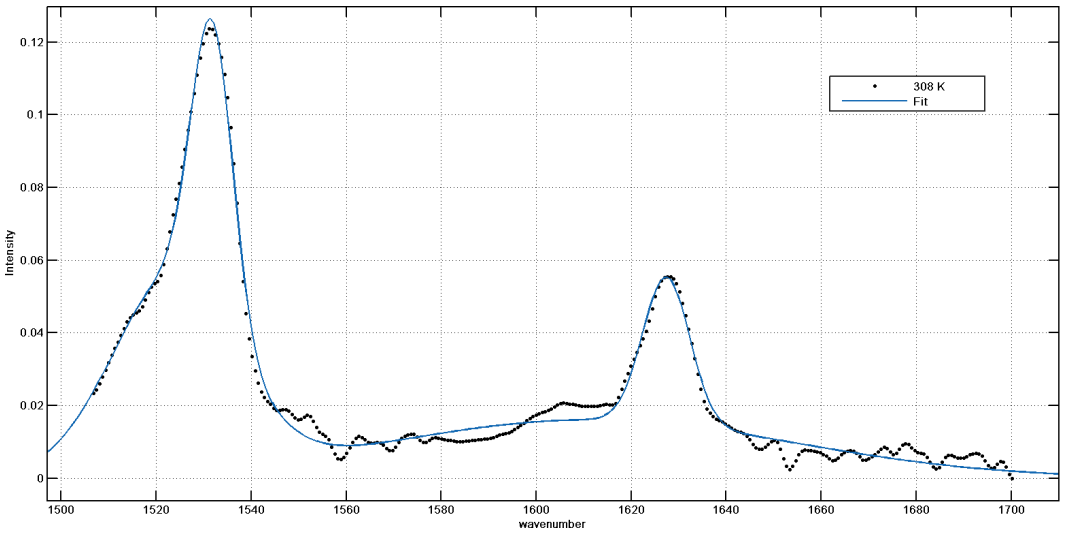

Figure 7-6: *The resultant four term Gaussian fitting for IR spectra of F_4TCNQ-DBTTF. The R-square value is 0.9901.*

While these peaks show a sudden decrease in amplitude from 380 K, there is no sudden jump or discontinuity in the centre of the peaks that would indicate a change in ρ. Instead, as temperature increases the spectrum gradually and smoothly shifts down to lower wave-numbers. This is to be expected, because higher temperature means a higher energy ground state, and thus less energy is required enter an excited state. Therefore, while a superficial interpretation of these data might suggest that ρ does appear to show a gradual smooth increase with temperature, we can conclude that there is indeed no significant change in ρ, and no change that corresponds to the structural shift.

At this point ρ can be ruled out as a possible factor in the structural transition. It does

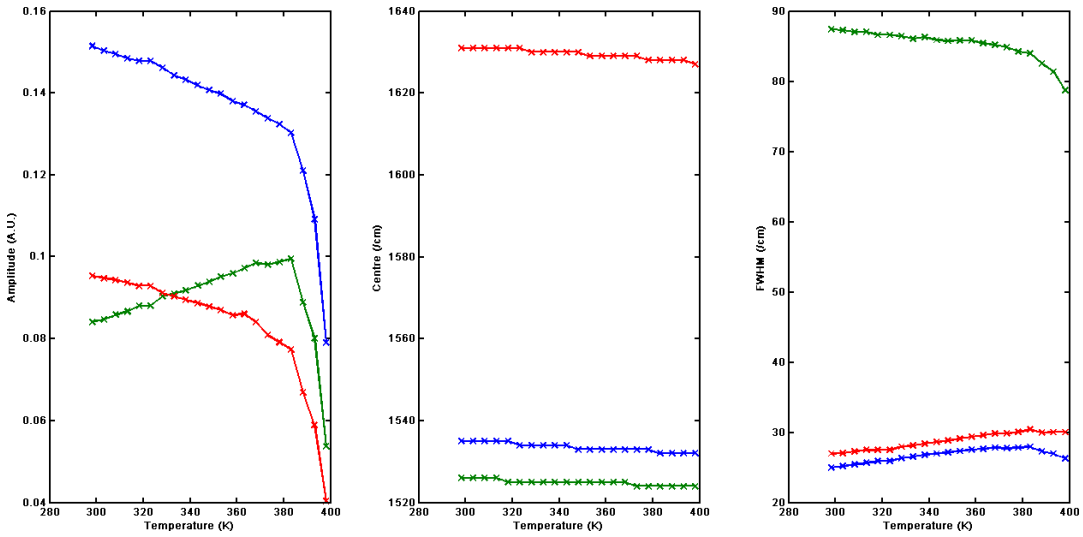

Figure 7-7: *The amplitudes, centres and Full Width at Half Maximum (FWHM) values for the Gaussian fittings of the IR spectra of F_4TCNQ-DBTTF.*

not appear to be heralded by, or cause, any significant shift in charge distribution. We we can turn to the work by Emge *et al.* discussed in 4.4.2. [23] The authors predicted that the room temperature structure of the system may represent the low temperature phase of a system affected by a Peierls instability. They speculated (although did not confirm) that at around 390 K there was a structural transition and that it would consist of uniform stacks.

We have demonstrated that this prediction is broadly correct, as the temperature increases the degree of dimerisation, as measured by the relative interplanar distances, decreases rapidly, and there does appear to be an abrupt distortion of the crystal structure at around 390 K.

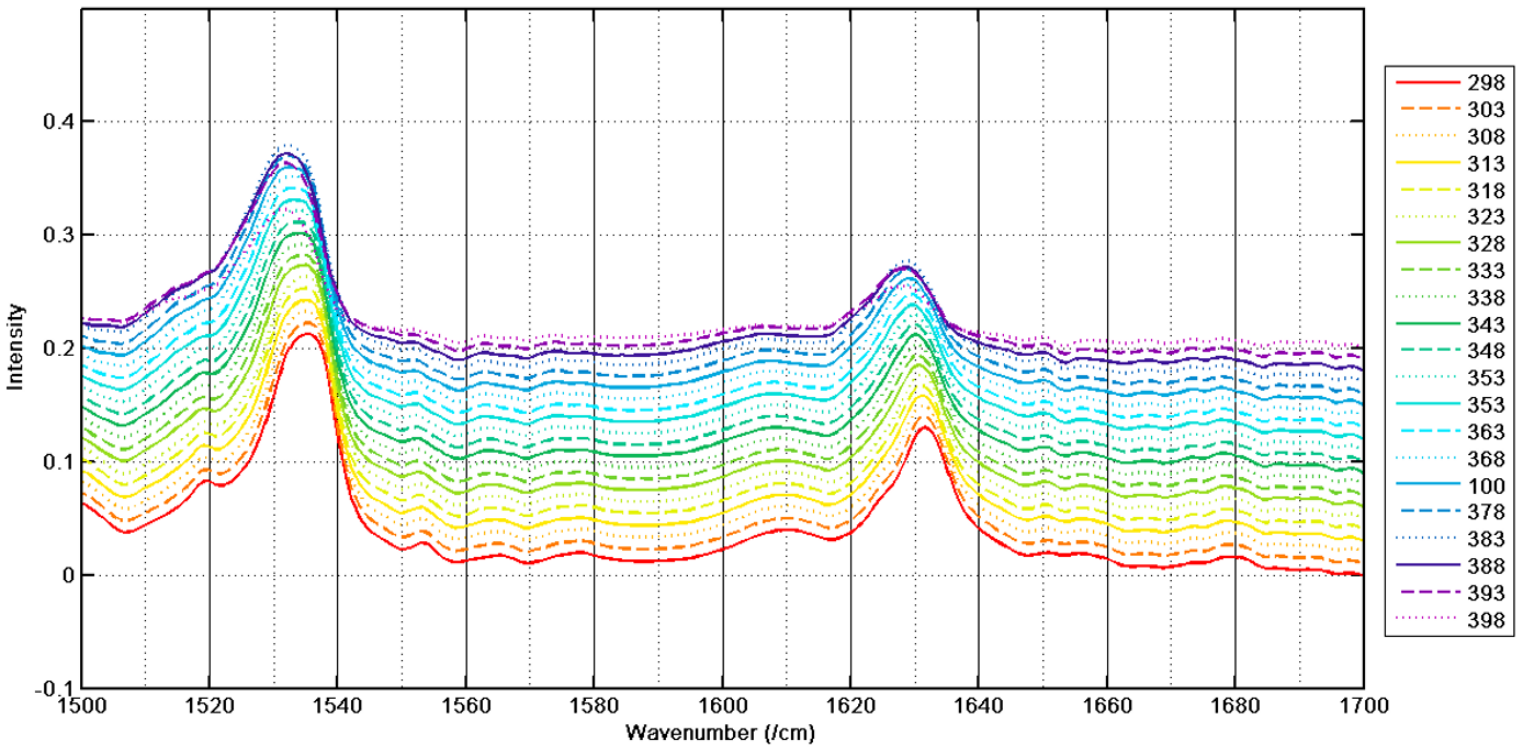

Figure 7-8: *Temperature dependent IR Spectra of the ρ sensitive C=C stretching modes for F_4TCNQ-DBTTF. While ρ does show a gradual increase with temperature, there is no sudden change at the transition point.*

7.4 The Low Temperature Regime

7.4.1 EPR Measurements

A set of EPR measurements were carried out in 5 K intervals between 5 K and 300 K at 9.5 GHz and at 50 K intervals at 35 GHz. At higher temperatures there is a single large peak, which is consistent with the presence of an organic free radial (the electron on the acceptor, and the hole on the donor) as expected. Both sets of measurements appear to show a transition occurring at around 150 K. Over the transition itself, there is almost no response, suggesting a significant reduction in the number of unpaired spins. Below the transition point the spectra becomes incredibly complex and multiple additional peaks form. In depth modelling will be necessary to fully probe this low temperature behaviour. Even so, there is no clear evidence of the hyperfine splitting patterns that would correspond to triplets. This can be seen in 7-9.

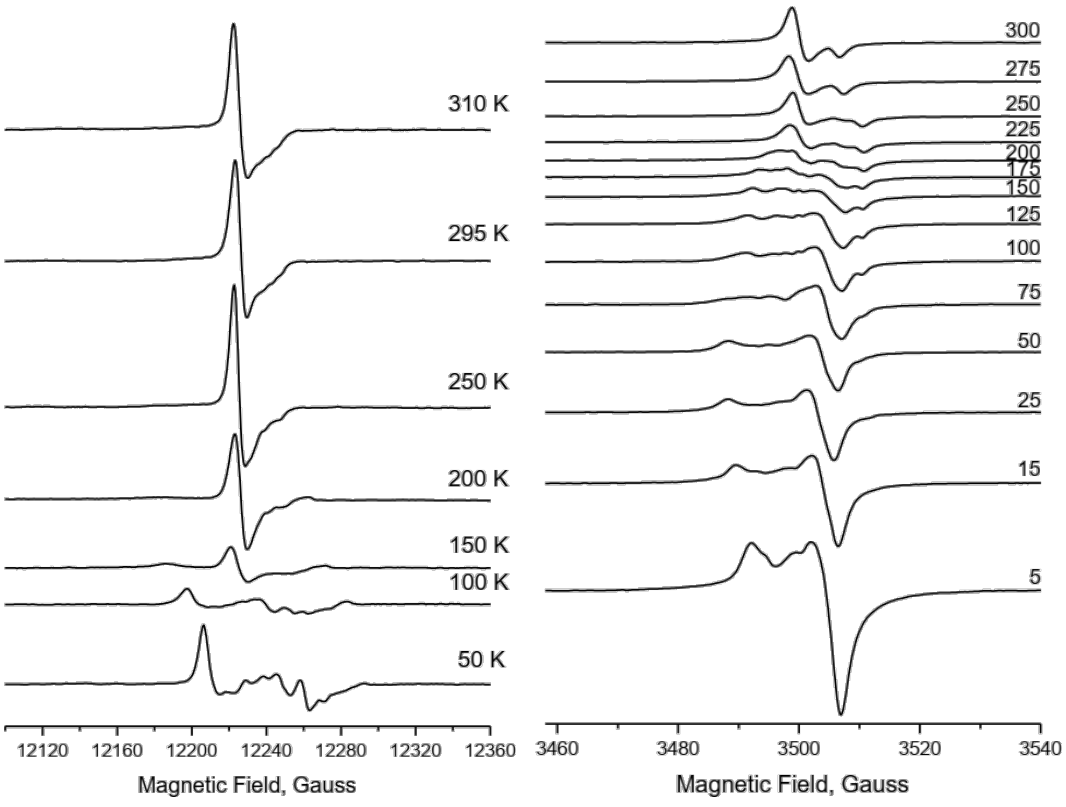

(a) *Q-band (35 GHz)* ***(b)*** *X-band (35 GHz)*

Figure 7-9: *EPR data for DBTTF-F_4TNCQ.*

7.4.2 X-ray Crystallography

Further x-ray measurements were taken at lower temperatures to determine whether there were any structural changes corresponding to the sharp transition in the EPR spectrum. Ultimately two sets of measurements were carried out; an initial set of exploratory measurements were carried out at 90, 120, 100, 150 K, and, after the EPR data was obtained, a subsequent set of measurements were taken at 110, 130, 160 and 170 K to provide a comprehensive temperature sweep from 90 K to 170 K.

Unfortunately, these two sets of measurements are inconsistent, as shown in Figure 7-10 and so no definitive conclusion can be drawn as to the nature of any low temperature structural transition at this time.

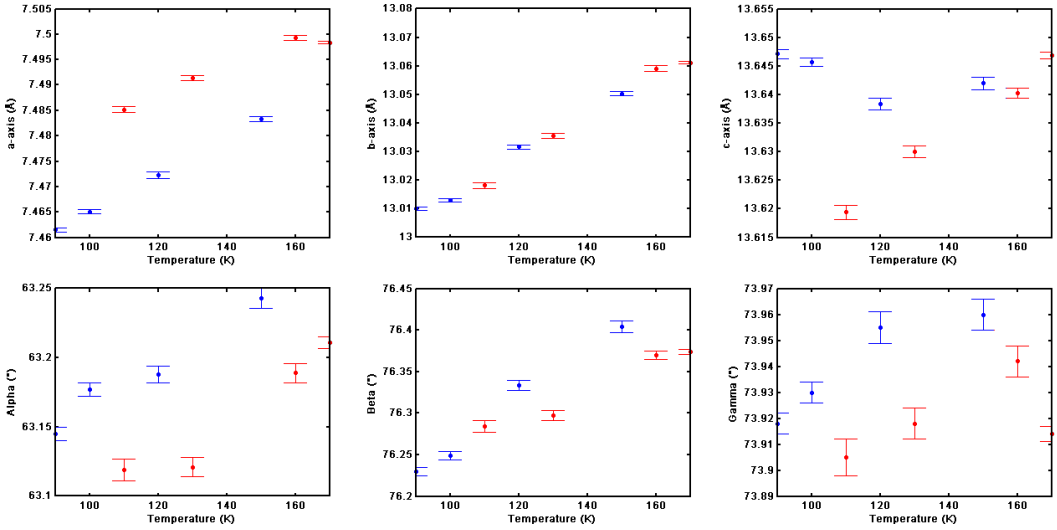

Figure 7-10: *Low temperature unit cell parameters for F_4TCNQ-DBTTF. Two sets of x-ray measurements were taken, labelled in blue and red.*

7.4.3 Reflectance Measurements

Finally, a set of low temperature reflectance measurements were also carried out between 600 and 1400 nm and at temperatures between 80 and 180 K in 5 degree increments, with additional measurements at 77 and 78 K, at the limits of temperature obtainable via liquid nitrogen cooling. These measurements could provide information about the energy band structure of the material. Unfortunately the data was supplied too late for any quantitative analysis at time of writing.

Chapter 8

Conclusions and Outlook

8.1 Introduction

The topic of this thesis is not entirely new. As was noted, during the 70s and 80s there was considerable research interest in charge transfer (CT) complexes after some preliminary studies appeared to demonstrate high temperature superconductive behaviour. [19] However these results could not be replicated and flaws in the original methodology were discovered. [9] Interest waned.

Recently, interest has returned, as these complexes have demonstrated the potential for efficient photo-current generation needed for organic photo-voltaic cells,[4] and ambipolar conductivity needed for organic semi-conductors. [110] The inherent nature of CT complexes means that in principle their properties are highly tune-able. Not only can individual constituents be varied by adding functional groups, but the constituents are capable of being assembled in multiple different supra-molecular configurations - different possible polymorphs which demonstrate different behaviours.

In many ways the field is still young. Unfortunately, at present there are few reliable systemic ways to grow specific complexes. Nor are there easy methods to predict, *a priori*, all possible polymorphs that could exist for any given constituent molecules or what their properties will be. This can easily be seen by the fact that novel polymorphs are still being discovered experimentally. [107, 89, 32].

Part of the problem is that the theoretical modelling is very difficult. In the case of physical vapour transport, it has been demonstrated that simple one dimensional models are inadequate for describing the system behaviour. [86] Solution based growth

methods fare little better. They are extremely solvent dependant, and must be tailored to the specific material. It has also been demonstrated that not all polymorphs are capable of being grown in solution. [41, 32]

Even once a given structure has been produced or proven to exist, modelling its behaviour can also prove difficult, as the material on the spin-Peierls transition (Subsection 2.5) demonstrates quite clearly. Modelling the interactions between a one dimensional Heisenberg chain and the three dimensional phonons is mathematically intractable unless a large number of assumptions are made. The validity and applicability of these assumptions can vary considerably depending on the system in question and great care must be made when attempting to carry out analysis. [12]

This is somewhat analogous to the various problems chemists struggle with regarding drug discovery. Here they must consider the supra-molecular interactions between a candidate drug molecule and a target receptor site. It is only within the last couple of decades that practical *in silico* techniques have developed to allow predictive computational modelling and virtual screening. [108]

8.2 Perylene-TCNQ

We have established two completely novel polymorphs of Perylene-TCNQ and demonstrate a temperature dependant phase transition from one polymorph to the other. We have characterised the physical structure of both polymorphs and provided estimates for the degree of charge transfer. We have also discovered, somewhat unusually, that the benzene rings of peryelene are heavily distorted. This is noteworthy as it is normally extremely energetically favourable for aromatic rings to be planar. This deviation appears to be a result of nitrogen short contact interactions.

Obvious future work would be to probe the energy band structure and to determine the precise nature of the supra-molecular interactions within the system and the physics of the system. Sadly, we were not able to carry out reflectance measurements as the crystals were extremely thin and needle-like and we were unable to reduce the beam spot size of the detector sufficiently.

Density Functional Theory (DFT) modelling could in principle provide insight into the electronic structure of the system, but attempting to implement DFT for charge transfer processes is still an area of ongoing research, as most current common techniques have proven unable to adequately predict the behaviour of these systems. [15]

8.3 DBTTF-F_4TCNQ

For DBTTF-F_4TNCQ we have demonstrated a high temperature structural transition which can be seen in both the unit cell parameters and the relative inter-molecular distances between adjacent DBTTF and F_4TCNQ molecules. This behaviour was previously predicted by Emge *et al.* but never confirmed. [23] Our observations generally match these predictions. In the process we also ascertained via both bond length and spectroscopic methods that the degree of charge transfer does not appear to change over this structural transition.

We also performed some low temperature measurements to try to further probe the behaviour of this system. Electron Paramagnetic Resonance (EPR) measurements appear to demonstrate a low temperature transition at around 150 K. Unfortunately, the spectra below this transition point are extremely complex and will require more theoretical work to be fully understood. Reflectance measurements were also carried out, and appear to corroborate the findings of the EPR data. Unfortunately, the data was obtained too late for detailed analysis here. Beyond that, obvious future work would be to carry out vibrational spectroscopy at low wave-numbers to try and ascertain the presence of phonon softening, which is expected to precede the structural changes.

Low temperature x-ray crystallography measurements were also carried out in an attempt to ascertain any structural changes corresponding to the changes in the EPR and reflectance spectra. Unfortunately, two sets of measurements were carried out and different times and with different crystal samples and they have produced inconsistent results. As such, the presence of any corresponding low temperature transition remains inconclusive. However, there is clearly scope for further research.

Bibliography

[1] M. Altarelli and D. Y. Smith. Superconvergence and sum rules for the optical constants: Physical meaning, comparison with experiment, and generalization. *Phys. Rev. B*, 9(4):1920–1298, 1974. doi: https://doi.org/10.1103/PhysRevB.9.1290.

[2] P. W. Anderson and P. A. Lee. Remarks on giant conductivity in ttf-tcnq. *Solid State Communications*, 13(5):595–598, 1973. doi: https://doi-org.ezproxy1.bath.ac.uk/10.1016/S0038-1098(73)80020-1. URL `http://journals.aps.org/rmp/abstract/10.1103/RevModPhys.32.466`.

[3] Graja Andrzej. *Low-dimensional Organic Conductors*. World Scientific, 1992. ISBN 9814506508.

[4] John E. Anthony. Functionalized acenes and heteroacenes for organic electronics. *Chemical Reviews*, 106(12):5028–5048, 2006. ISSN 0009-2665. doi: 10.1021/cr050966z. URL `https://doi.org/10.1021/cr050966z`.

[5] Neil W. Ashcroft and David N. Mermin. *Solid State Physics*. Holt, Rinehart and Winston, New York, 1976.

[6] R. Z. Bachrach and F. C. Brown. Exciton-optical properties of tlbr and tlcl. *Phys. Rev. B*, 1(2):818–831, 1970. ISSN 0556-2805. doi: http://dx.doi.org/10.1103/PhysRevB.1.818.

[7] A. D. Bandrauk, K. D. Truong, and C. Carlone. Optical and raman spectra of single crystals of perylene-tcnq charge transfer complexes. *Can. J. Chem.*, 60(5):588–595, 1982. doi: https://doi.org/10.1139/v82-087.

[8] C. J. Bender. Theoretical models of charge-transfer complexes. *Chem. Soc. Rev.*, 15:475–502, 1986. ISSN 0306-0012. doi: http://dx.doi.org/10.1039/cs9861500475.

[9] A. J. Berlinsky. Organic metals. *Contemporary Physics*, 17(4):331–354, 1976. ISSN 0010-7514. doi: 10.1080/00107517608224048. URL https://doi.org/10.1080/00107517608224048.

[10] Jason T. Bloking, George F. Burkhard, Alan Sellinger, Jean M. J. Fréchet, Aram Amassian, Moritz K. Riede, Michael D. McGehee, Dieter Neher, and Alberto Salleo. Efficient charge generation by relaxed charge-transfer states at organic interfaces. *Nat. Mater.*, 13(1):63–64, 2014. ISSN 1476-1122. doi: 10.1038/nmat3807.

[11] J. W. Bray, H. R. Hart, L. V. Interrante, I. S. Jacobs, J. S. Kasper, G. D. Watkins, S. H. Wee, and J. C. Bonner. Observation of a spin-peierls transition in a heisenberg antiferromagnetic linear-chain system. *Physical Review Letters*, 35(11):744–747, 1975. doi: 10.1103/PhysRevLett.35.744. URL https://link.aps.org/doi/10.1103/PhysRevLett.35.744.

[12] James W. Bray, Leonard V. Interrante, Israel S. Jacobs, and Jill C. Bonner. *The Spin-Peierls Transition*, pages 353–415. Springer US, Boston, MA, 1983. ISBN 978-1-4684-4175-8. doi: 10.1007/978-1-4684-4175-8_7. URL https://doi.org/10.1007/978-1-4684-4175-8_7.

[13] A. W. Brinkman and J. Carles. The growth of crystals from the vapour. *Progress in Crystal Growth and Characterization of Materials*, 37(4):169–209, 1998. ISSN 0960-8974. doi: 10.1016/S0960-8974(99)00004-2.

[14] A. J. C. Buurma, O. D. Jurchescu, I. Shokaryev, J. Baas, A. Meetsma, G. A. de Wijs, R. A. de Groot, and T. T. M. Palstra. Crystal growth, structure, and electronic band structure of tetracene-tcnq. *Journal of Physical Chemistry C*, 111(8):3486–3489, 2007. ISSN 1932-7447. doi: 10.1021/jp065944a. URL http://pubs.acs.org/doi/pdfplus/10.1021/cm049187%2B.

[15] Zheng-Li Cai, Maxwell J. Crossley, Jeffrey R. Reimers, Rika Kobayashi, and Roger D. Amos. Density functional theory for charge transfer: the nature of the n-bands of porphyrins and chlorophylls revealed through cam-b3lyp, caspt2, and sac-ci calculations. *The Journal of Physical Chemistry B*, 110(31):15624–15632, 2006. ISSN 1520-6106. doi: 10.1021/jp063376t. URL https://doi.org/10.1021/jp063376t.

[16] P. M. Chaikin and T. C. Lubensky. *Mean-field Theory*, page 144212. Cambridge University Press, 1995. doi: 10.1017/CBO9780511813467.005.

[17] J. S. Chappell, A. N. Bloch, W. A. Bryden, M. Maxfield, T. O. Poehler, and D. O. Cowan. Degree of charge transfer in organic conductors by infrared absorption spectroscopy. *Journal of the American Chemical Society.*, 103(9):2442–2443, 1981. ISSN 0002-7863. doi: 10.1021/ja00399a066.

[18] M. J. Cohen, L. B. Coleman, A. F. Garito, and A. J. Heeger. Electrical conductivity of tetrathiofulvalinium tetracyanoquinodimethan (ttf) (tcnq). *Phys. Rev. B*, 10(4):1298, 1974. doi: https://doi.org/10.1103/PhysRevB.10.1298.

[19] L. B. Coleman, M. J. Cohen, Do J. Sandman, F. G. Yamagishi, A. F. Garito, and A. J. Heeger. Superconducting fluctuations and the peierls instability in an organic solid. *Solid State Communications*, 12(11):1125–1132, 1973. ISSN 0038-1098.

[20] R. N. Compton and C. D. Cooper. Negative ion properties of tetracyanoquinodimethan: Electron affinity and compound states. *J. Chem. Phys.*, 66(10):4325–4329, 1977. ISSN 0021-9606. doi: 10.1063/1.433743.

[21] M. C. Cross and Daniel S. Fisher. A new theory of the spin-peierls transition with special relevance to the experiments on ttfcubdt. *Physical Review B*, 19(1): 402, 1979.

[22] J. J. De Yoreo and P. G. Vekilov. Principles of crystal nucleation and growth. *Rev. Mineral. Geochem.*, 54(1):57–93, 2003. doi: https://doi.org/10.2113/0540057.

[23] Thomas J. Emge, Wayne A. Bryden, F. Mitchell Wiygul, Dwaine O. Cowan, Thomas J. Kistenmacher, and Aaron N. Bloch. Structure of an organic charge-transfer salt derived from dibenzotetrathiafulvalene and tetrafluorotetracyanoquinodimethane (dbttf-tcnqf4). observation of a high-temperature phase transition. *The Journal of Chemical Physics*, 77(6):3188–3197, 1982. ISSN 0021-9606. doi: 10.1063/1.444193.

[24] Thomas J. Emge, F. Mitchell Wiygul, John S. Chappell, Aaron N. Bloch, John P. Ferraris, Dwaine O. Cowan, and Thomas J. Kistenmacher. Crystal structures for the electron donor dibenzotetrathiafulavalene, dbttf, and its mixed-stack charge-transfer salts with the electron acceptors 7,7,8,8-tetracyano-p-quinodimethane, tcnq, and 2,5-difluoro-7,7,8,8-tetracyano-p-quinodimethane, 2,5-tcnqf2. *Molecular Crystals and Liquid Crystals*, 87(1-2):137–161, 1982. ISSN 0026-8941. doi: 10.1080/00268948208083778. URL `https://doi.org/10.1080/00268948208083778`.

[25] John Ferraris, D. O. Cowan, V. Walatka, and J. H. Perlstein. Electron transfer in a new highly conducting donor-acceptor complex. *Journal of the American Chemical Society*, 95(3):948–949, 1973. ISSN 0002-7863. doi: 10.1021/ja00784a066. URL `https://doi.org/10.1021/ja00784a066`.

[26] H. Herbstein Frank and Moshe Kapon. Classification of closed shell tcnq salts into structural families and comparison of diffraction and spectroscopic methods of assigning charge states to tcnq moieties. *Crystallography Reviews*, 14(1):3–74, 2008. doi: 10.1080/08893110801980780.

[27] H. Bruce Friedrich and Willis B. Person. Infrared spectra of charge-transfer complexes. vi. theory. *The Journal of Chemical Physics*, 44(5):2161–2170, 1966. ISSN 0021-9606. doi: 10.1063/1.1726994.

[28] A. Girlando, R. Bozio, C. Pecile, and J. B. Torrance. Discovery of vibronic effects in the raman spectra of mixed-stack charge-transfer crystals. *Phys. Rev. B.*, 26 (4):2306, 1982. doi: https://doi.org/10.1103/PhysRevB.26.2306.

[29] Alberto Girlando, Anna Painelli, and Cesare Pecile. Electron-intramolecular phonon coupling in regular and dimerized mixed stack organic semiconductors. *Molecular Crystals and Liquid Crystals*, 120(1):17–26, 1985. ISSN 0026-8941. doi: 10.1080/00268948508075754.

[30] J. Gliński and J. Kalinowski. Thermoreflectance spectrum of tetracene single crystal. *Solid State Commun.*, 38(2):155–157, 1981. ISSN 0038-1098. doi: 10.1016/0038-1098(81)90810-3.

[31] Katelyn P. Goetz, Derek Vermeulen, Margaret E. Payne, Christian Kloc, Laurie E. McNeil, and Oana D. Jurchescu. Charge-transfer complexes: new perspectives on an old class of compounds. *Journal of Materials Chemistry C*, 2(17):3065–3076, 2014. ISSN 2050-7526. doi: 10.1039/c3tc32062f. URL `http://pubs.rsc.org/en/content/articlepdf/2014/tc/c3tc32062f`.

[32] Katelyn P. Goetz, Jun'ya Tsutsumi, Sujitra Pookpanratana, Jihua Chen, Nathan S. Corbin, Rakesh K. Behera, Veaceslav Coropceanu, Curt A. Richter, Christina A. Hacker, Tatsuo Hasegawa, and Oana D. Jurchescu. Polymorphism in the 1:1 charge-transfer complex dbttf-tcnq and its effects on optical and electronic properties. *Advanced Electronic Materials*, 2(10):1600203, 2016. ISSN 2199-160X. doi: 10.1002/aelm.201600203. URL `https://www.ncbi.nlm.nih.gov/pubmed/29387522`.

[33] D. J. Gundlach, L. Zhou, J. A. Nichols, T. N. Jackson, P. V. Necliudov, and M. S. Shur. An experimental study of contact effects in organic thin film transistors. *J. Appl. Phys.*, 100(2):024509, 2006. doi: https://doi.org/10.1063/1.2215132.

[34] A. W. Hanson. 7, 7, 8, 8-tetracyanoquinodimethane (perylene) 2perylene. *Acta Crystallogr. B*, 34(7):2339–2341, 1978. doi: https://doi.org/10.1107/S0567740878008110.

[35] Eugene Hecht. *Optics (4th Ed.)*. Addison Wesley, San Francisco, 2002.

[36] James Martindale Henderson, Matteo Masino, Lauren E. Hatcher, Gabriele Kociok-Köhn, Tommaso Salzillo, Aldo Brillante, Paul R. Raithby, Alberto Girlando, and Enrico Da Como. New polymorphs of perylene:tcnq charge transfer cocrystals. *Crystal Growth & Design*, 2018. ISSN 1528-7483. doi: 10.1021/acs.cgd.7b01391.

[37] Frank H. Herbstein. How precise are measurements of unit-cell dimensions from single crystals? *Acta Crystallographica Section B*, 56(4):547–557, Aug 2000. doi: 10.1107/S010876810000269X. URL `https://doi.org/10.1107/S010876810000269X`.

[38] Frank H. Herbstein. *Crystalline molecular complexes and compounds: structures and principles*, volume 1. Oxford University Press, 2005. ISBN 0198568932.

[39] Frank H. Herbstein and Moshe Kapon. Classification of closed shell tcnq salts into structural families and comparison of diffraction and spectroscopic methods of assigning charge states to tcnq moieties. *Crystallogr. Rev.*, 14(1):3–74, 2008. doi: https://doi.org/10.1080/08893110801980780.

[40] P. Hu, K. Du, F. Wei, H. Jiang, and C. Kloc. Crystal growth, homo–lumo engineering, and charge transfer degree in perylene-fxtcnq (x = 1, 2, 4) organic charge transfer binary compounds. *Cryst. Growth Des.*, 16(5):30193027, 2016. doi: 10.1021/acs.cgd.5b01675.

[41] Peng Hu, Lin Ma, Ke Jie Tan, Hui Jiang, Fengxia Wei, Chuhuan Yu, Katelyn P. Goetz, Oana D. Jurchescu, Laurie E. McNeil, and Gagik G. Gurzadyan. Solvent-dependent stoichiometry in perylene7, 7, 8, 8-tetracyanoquinodimethane charge transfer compound single crystals. *Crystal Growth & Design*, 14(12):6376–6382, 2014. ISSN 1528-7483. doi: 10.1021/cg501206f. URL `http://pubs.acs.org/doi/pdfplus/10.1021/cg501206f`.

[42] R. Hulthén. Kramers-kronig relations generalized: on dispersion relations for finite frequency intervals. a spectrum-restoring filter. *JOSA*, 72(6):794–803, 1982.

[43] Crystal Impact. Diamond version 3, 2014-2017.

[44] K. Ishii, K. Yakushi, H. Kuroda, and H. Inokuchi. Reflection and photoconduction spectra of the single crystals of perylene-tcnq 1: 1 and 3: 1 molecular complexes. *Bull. Chem. Soc. Jpn.*, 57(11):3043–3047, 1984.

[45] K. Iwasaki, T. Ida, A. Kawamoto, A. Ugawa, Y. Yamashita, K. Yakushi, and T. Suzuki. Structure of the chargetransfer complex of (dbttf)(btdatcnq). *Acta Crystallographica Section C*, 48(11):1982–1984, 1992. ISSN 0108-2701. doi: 10.1107/S0108270192003445.

[46] I. S. Jacobs, J. W. Bray, H. R. Hart Jr, L .V. Interrante, J. S. Kasper, G. D. Watkins, D. E. Prober, and J. C. Bonner. Spin-peierls transitions in magnetic donor-acceptor compounds of tetrathiafulvalene (ttf) with bisdithiolene metal complexes. *Physical Review B*, 14(7):3036, 1976.

[47] K. Jacobs, M. M. Faktor, and I. Garrett. Growth of crystals from the vapour. *Crystal research and technology*, 11(1):K10–K10, 1976. ISSN 0232-1300. doi: 10.1002/crat.19760110119info:doi/10.1002/crat.19760110119.

[48] David L. Jeanmaire and Richard P. Van Duyne. Resonance raman spectroelectrochemistry. 2. scattering spectroscopy accompanying excitation of the lowest 2b1u excited state of the tetracyanoquinodimethane anion radical. *Journal of the American Chemical Society*, 98(14):4029–4033, 1976. ISSN 0002-7863. doi: 10.1021/ja00430a001.

[49] Hui Jiang, Peng Hu, Jun Ye, Keke K. Zhang, Yi Long, Wenping Hu, and Christian Kloc. Tuning of the degree of charge transfer and the electronic properties in organic binary compounds by crystal engineering: a perspective. *J. Mater. Chem. C*, 6(8):1884–1902, 2018. ISSN 2050-7526. doi: 10.1039/c7tc04982j.

[50] Kazunori Kadota, Satoshi Tanida, Yoshiyuki Shirakawa, Atsuko Shimosaka, and Jusuke Hidaka. Production of asymmetrical particles in a crystallization process using liquid–liquid interfaces. *Journal of Chemical Engineering of Japan*, 40(3): 217–221, 2007. doi: 10.1252/jcej.40.217.

[51] E. Kampar. Degree of charge transfer in donor acceptor systems of the pi-pi type. *Russian Chemical Reviews*, 55:334–342, 1986. doi: 10.1070/RC1986v055n04ABEH003193.

[52] Z. M. Khoshhesab. *Reflectance IR spectroscopy*. INTECH Open Access Publisher, 2012.

[53] J. Kim, J. Chung, J. Hyon, C. Seo, J. Nam, and Y. Kang. Heterogeneous charge-transfer nanorods by strained melt-molding lithography. *J. Nanosci. Nanotechnol.*, 16(3):2715–2718, 2016. ISSN 1533-4880. doi: 10.1166/jnn.2016.11100.

[54] Jueun Kim, Youngjong Kang, and Jaejong Lee. Fabrication of the tetrathiafulvalene2,3,5,6-tetrafluoro-7,7,8,8-tetracyanoquinodimethane charge transfer complex with high crystallinity by eutectic melting method. *Japanese Journal of Applied Physics*, 57(6S1):06HD01, 2018. ISSN 00214922. doi: 10.7567/JJAP.57.06HD01.

[55] Katsumi Kimura and Masaji Kubo. Structures of dimethyl ether and methyl alcohol. *The Journal of Chemical Physics*, 30(1):151–158, 1959. ISSN 0021-9606. doi: 10.1063/1.1729867. URL `https://doi.org/10.1063/1.1729867`.

[56] Thomas J. Kistenmacher, Terry E. Phillips, and Dwaine O. Cowan. The crystal structure of the 1: 1 radical cation-radical anion salt of 2, 2'-bis-l, 3-dithiole (ttf) and 7, 7, 8, 8-tetracyanoquinodimethane (tcnq). *Acta Crystallographica Section B: Structural Crystallography and Crystal Chemistry*, 30(3):763–768, 1974. ISSN 0567-7408.

[57] Ch. Kloc, P. G. Simpkins, T. Siegrist, and R. A. Laudise. Physical vapor growth of centimeter sized crystals of α-hexathiophene. *Journal of Crystal Growth*, 182 (3):416–427, 1997. ISSN 0022-0248. doi: 10.1016/S0022-0248(97)00370-9.

[58] Christian Kloc, Theo Siegrist, and Jens Pflaum. *Growth of Single-Crystal Organic Semiconductors*, pages 845–867. Springer Berlin Heidelberg, Berlin, Heidelberg, 2010. ISBN 978-3-540-74761-1. doi: 10.1007/978-3-540-74761-1_25. URL `https://doi.org/10.1007/978-3-540-74761-1_25`.

[59] R. Klucker and U. Nielsen. Kramers-kronig analysis of reflection data. *Comput. Phys. Commun.*, 6(4):187–193, 1973.

[60] Hayao Kobayashi and Jyuzo Nakayama. The crystal structure of the charge-transfer complex of dibenzotetrathiafulvalene-tetracyanoquinodimethane, dbttftcnq. *Bulletin of the Chemical Society of Japan*, 54(8):2408–2411, 1981. doi: 10.1246/bcsj.54.2408. URL `https://doi.org/10.1246/bcsj.54.2408`.

[61] J. I. Krugler, C. G. Montgomery, and H. M. McConnell. Collective electronic

states in molecular crystals. *The Journal of Chemical Physics*, 41(8):2421–2428, 1964. ISSN 0021-9606. doi: 10.1063/1.1726281.

[62] T. M. Krygowski, R. Anulewicz, and J. Kruszewski. Crystallographic studies and physicochemical properties of electron compounds. iii. stabilization energy and the kekul structure contributions derived from experimental bond lengths. *Acta Crystallographica Section B*, 39(6):732–739, 1983. ISSN 01087681. doi: 10.1107/S0108768183003328.

[63] Kozo Kuchitsu, Tsutomu Fukuyama, and Yonezo Morino. The role of isotopic differences in the determination of molecular structure. a supplementary note on the structure of acrolein. *Journal of Molecular Structure*, 4(1):41–50, 1969. ISSN 0022-2860. doi: https://doi.org/10.1016/0022-2860(69)85027-1. URL `http://www.sciencedirect.com/science/article/pii/0022286069850271`.

[64] Kari Kveseth, Ragnhild Seip, and Denis A. Kohl. Conformational analysis. the structure and torsional potential. *Acta Chem. Scand. A*, 34(1), 1980.

[65] R. A. Laudise, Ch. Kloc, P. G. Simpkins, and T. Siegrist. Physical vapor growth of organic semiconductors. *J. Cryst. Growth*, 187:449–454, 1998.

[66] R. E. Long, R. A. Sparks, and K. N. Trueblood. The crystal and molecular structure of 7,7,8,8 tetracyanoquinodimethane. *Acta Crystallographica*, 18(5): 932–939, 1965. ISSN 0365-110X. doi: 10.1107/S0365110X65002256.

[67] Valerio Lucarini. *Kramers-Kronig Relations in Optical Materials Research*. Springer-Verlag, Berlin, Heidelberg, 2005.

[68] Clare F. Macrae, Ian J. Bruno, James A. Chisholm, Paul R. Edgington, Patrick McCabe, Elna Pidcock, Lucia Rodriguez-Monge, Robin Taylor, J. van de Streek, and Peter A. Wood. Mercury csd 2.0 – new features for the visualization and investigation of crystal structures. *Journal of Applied Crystallography*, 41(2): 466–470, 2008. doi: 10.1107/S0021889807067908. URL `https://doi.org/10.1107/S0021889807067908`.

[69] Benjamin Mahns, Olga Kataeva, Daut Islamov, Silke Hampel, Frank Steckel, Christian Hess, Martin Knupfer, Bernd Bchner, Cameliu Himcinschi, Torsten Hahn, Roman Renger, and Jens Kortus. Crystal growth, structure, and transport properties of the charge-transfer salt picene/ 2,3,5,6- tetrafluoro- 7,7,8,8- tetracyanoquinodimethane. *Crystal Growth & Design*, 14(3):1338–1346, 2014. ISSN 1528-7483. doi: 10.1021/cg401841n.

[70] H. M. McConnell, B. M. Hoffman, and R. M. Metzger. Charge transfer in molecular crystals. *Proceedings of the National Academy of Sciences of the United States of America*, 53(1):46–50, 1965. ISSN 0027-8424 (Print) 0027-8424 (Linking). URL http://www.ncbi.nlm.nih.gov/pubmed/16578588.

[71] Moreno Meneghetti and Cesare Pecile. Charge-transfer organic crystals: Molecular vibrations and spectroscopic effects of electronmolecular vibration coupling of the strong electron acceptor tcnqf4. *The Journal of Chemical Physics*, 84(8):4149–4162, 1986. ISSN 0021-9606. doi: Doi10.1063/1.450086. URL http://scitation.aip.org/docserver/fulltext/aip/journal/jcp/84/8/1.450086.pdf?expires=1449660428&id=id&accname=2116340&checksum=F55D98BF5460E0B1F2D36A1093AEB5F3.

[72] G. W. Milton, D. J. Eyre, and J. V. Mantese. Finite frequency range kramers-kronig relations: Bounds on the dispersion. *Phys. Rev. Lett.*, 79(16):3062–3065, 1997.

[73] R. S. Mulliken. Low electronic states of simple hetropolar diatomic molecules: Iii. hydrogen and univalent metal halides. *Phys. Rev.*, 51(5):310, 1937.

[74] R. S. Mulliken. Molecular compounds and their spectra. ii. *J. Am. Chem. Soc.*, 74(3):811–824, 1952.

[75] R. S. Mulliken. Molecular compounds and their spectra. iii. the interaction of electron donors and acceptors. *Journal of Physical Chemistry*, 56(7):801–822, 1952.

[76] R. S. Mulliken. The interaction of electron donors and acceptors. *Journal de Chimie Physique et de Physico-Chimie Biologique*, 61(1-2):20–38, 1964. doi: https://doi.org/10.1051/jcp/1964610020.

[77] International Union of Crystallography. R factor, 2017. URL http://reference.iucr.org/dictionary/R_factor. Accessed: 2019-09-30.

[78] C. Dastoor Paul, Feron Krishna, J. Belcher Warwick, and J. Fell Christopher. Organic solar cells: Understanding the role of forster resonance energy transfer. *International Journal of Molecular Sciences*, 13(12):17019–17047, 2012. ISSN 1422-0067. doi: 10.3390/ijms131217019.

[79] Robert E. Penn. Microwave spectrum of 2-propene-1-imine, ch2chchnh. *Journal of Molecular Spectroscopy*, 69(3):373–382, 1978. ISSN 0022-2852. doi: https://

doi.org/10.1016/0022-2852(78)90230-8. URL http://www.sciencedirect.com/science/article/pii/0022285278902308.

[80] R. R. Pennelly and C. J. Eckhardt. Quasi-metallic reflection spectra of tcnq single-crystals. *Chemical Physics*, 12(1):89–105, 1976. ISSN 0301-0104. doi: Doi10.1016/0301-0104(76)80115-2. URL <GotoISI>://WOS:A1976BB50100011.

[81] P. Peumanns, V. Bulovi, and S. R. Forrest. Efficient photon harvesting at high optical intensities in ultrathin organic doubleheterostructure photovoltaic diodes. *Apply. Phys. Lett.*, 76(19):2650–2652, 2000.

[82] P. Peumans, A. Yakimov, and S. R. Forrest. Small molecular weight organic thin-film photodetectors and solar cells. *J. App. Phys.*, 93(7):3693–3723, 2003.

[83] W. G. Pfann. Principles of zone-melting. *JOM*, 4(7):747–753, 1952. ISSN 1543-1851. doi: 10.1007/BF03398137. URL https://doi.org/10.1007/BF03398137.

[84] C. M. Pina and A. Putnis. The kinetics of nucleation of solid solutions from aqueous solutions: a new model for calculating non-equilibrium distribution coefficients. *Geochim. Cosmochim. Acta*, 66(2):185–192, 2002.

[85] Péter Pulay and Ferenc Török. Force constants, vibrational assignment and geometry of methyl amine from hartreefock calculations. *Journal of Molecular Structure*, 29(2):239–246, 1975. ISSN 0022-2860. doi: https://doi.org/10.1016/0022-2860(75)85032-0. URL http://www.sciencedirect.com/science/article/pii/0022286075850320.

[86] F. Rosenberger, J. Ouazzani, I. Viohl, and N. Buchan. Physical vapor transport revisited. *J. Crystal Growth*, 171(1):270–287, 1997.

[87] J. Rostalski and D. Deissner. Monochromatic versus solar efficiencies of organic solar cells. *Sol. Energy Mater. Sol. Cells*, 61(1):87–95, 2000.

[88] Sven P. Rudin. Generalization of soft phonon modes. *Phys. Rev. B*, 97:134114, Apr 2018. doi: 10.1103/PhysRevB.97.134114. URL https://link.aps.org/doi/10.1103/PhysRevB.97.134114.

[89] T. Salzillo, M. Masino, G. Kociok-Köhn, D. Di Nuzzo, E. Venuti, R. G. Della Valle, D. Vanossi, C. Fontanesi, A. Girlando, A. Brillante, and E. Da Como. Structure, stoichiometry, and charge transfer in cocrystals of perylene with tcnq-f x. *Crystal Growth & Design*, 16(5):3028–3036, 2016. ISSN 15287483. doi: 10.1021/acs.cgd.5b01663.

[90] D. Schwarzenbach, S. C. Abrahams, H. D. Flack, W. Gonschorek, Th. Hahn, K. Huml, R. E. Marsh, E. Prince, B. E. Robertson, J. S. Rollett, and A. J. C. Wilson. Statistical descriptors in crystallography: Report of the IUCr Subcommittee on Statistical Descriptors. *Acta Crystallographica Section A*, 45(1):63–75, Jan 1989. doi: 10.1107/S0108767388009596.

[91] Markus Schwoerer. *Organic molecular solids*. Weinheim : Wiley-VCH, Weinheim, 2008.

[92] M. I. Shchuka, A. L. Motyka, and M. R. Topp. Two-photon threshold ionization spectroscopy of perylene and van der waals complexes. *Chem. Phys. Lett.*, 164 (1):87–95, 1989.

[93] I. Shokaryev, A. J. C. Buurma, O. D. Jurchescu, M. A. Uijttewaal, G. A. de Wijs, T. T. M. Palstra, and R. A. de Groot. Electronic band structure of tetracene-tcnq and perylene-tcnq compounds. *Journal of Physical Chemistry A*, 112(11): 2497–2502, 2008.

[94] Mutasem Omar Sinnokrot and C. David Sherrill. High-accuracy quantum mechanical studies of interactions in benzene dimers. *The Journal of Physical Chemistry A*, 110(37):10656–10668, 2006. ISSN 1089-5639. doi: 10.1021/jp0610416. URL `https://doi.org/10.1021/jp0610416`.

[95] Douglas A. Skoog. *Principles of instrumental analysis*, pages 805–808. Saunders College, Philadelphia, Pa. ; London, 5th ed. edition, 1998.

[96] D. Y. Smith. Dispersion relations for complex reflectivities. *J. Opt. Soc. Am.*, 67 (4):570, 1977. ISSN 0030-3941. doi: 10.1364/JOSA.67.000570.

[97] D. Y. Smith and Corinne A. Manogue. Superconvergence relations and sum rules for reflection spectroscopy. *J. Opt. Soc. Am.*, 71(8):935–947, 1981.

[98] Paul J. Strebel and Zoltán G. Soos. Theory of charge transfer in aromatic donor-acceptor crystals. *The Journal of Chemical Physics*, 53(10):4077–4090, 1970. ISSN 0021-9606. doi: Doi10.1063/1.1673881.

[99] R. Swietlik. Phase transition in mem(tcnq)2 single crystals by infrared reflection spectroscopy. *Solid State Communications*, 45(1):27–29, 1983. ISSN 0038-1098. doi: https://doi.org/10.1016/0038-1098(83)90877-3. URL `http://www.sciencedirect.com/science/article/pii/0038109883908773`.

[100] Y. Takahashi, T. Hasegawa, Y. Abe, Y. Tokura, and G. Saito. Organic metal

electrodes for controlled p-and n-type carrier injections in organic field-effect transistors. *Appl. Phys. Lett.*, 88(7):3504, 2006.

[101] C. W. Tang. Two-layer organic photovoltaic cell. *Apply. Phys. Lett.*, 48(2): 183–185, 1986.

[102] Ranjit Thakuria, Naba K. Nath, and Binoy K. Saha. The nature and applications of interactions: A perspective. *Crystal Growth & Design*, 19(2):523–528, 2019. ISSN 1528-7483. doi: 10.1021/acs.cgd.8b01630. URL `https://doi.org/10.1021/acs.cgd.8b01630`.

[103] I. J. Tickle and C. K. Prout. Molecular complexes. part xvii. crystal and molecular structure of perylene7, 7, 8, 8-tetracyanoquinodimethane molecular complex. *J. Chem. Soc.*, 2(6):720–723, 1973.

[104] J. B. Torrance, J. E. Vazquez, J. J. Mayerle, and V. Y. Lee. Discovery of a neutral-to-ionic phase-transition in organic materials. *Physical Review Letters*, 46(4):253–257, 1981. ISSN 0031-9007. doi: DOI10.1103/PhysRevLett.46.253. URL `<GotoISI>://WOS:A1981KZ00700013`.

[105] J. Y. Tsutsumi, T. Yamada, H. Matsui, S. Haas, and T. Hasegawa. Competition between charge-transfer exciton dissociation and direct photocarrier generation in molecular donor-acceptor compounds. *Phys. Rev. Lett.*, 105(22):226601, 2010.

[106] J.Y. Tsutsumi, H. Matsui, T. Yamada, R. Kumai, and T. Hasegawa. Generation and diffusion of photocarriers in molecular donor–acceptor systems: Dependence on charge-transfer gap energy. *Journal of Physical Chemistry C*, 116(45):23957–23964, 2012.

[107] D. Vermeulen, L. Y. Zhu, K. P. Goetz, Peng Hu, Hui Jiang, C. S. Day, O. D. Jurchescu, V. Coropceanu, C. Kloc, and L. E. McNeil. Charge transport properties of perylene-tcnq crystals: The effect of stoichiometry. *The Journal of Physical Chemistry C*, 118(42):24688–2469, 2014. ISSN 1932-7447. doi: 10.1021/jp508520x.

[108] Chen Wang, Pan Xu, Luyu Zhang, Jing Huang, Kongkai Zhu, and Cheng Luo. Current strategies and applications for precision drug design. *Frontiers in pharmacology*, 9:787–787, 2018. ISSN 1663-9812. doi: 10.3389/fphar.2018.00787. URL `https://www.ncbi.nlm.nih.gov/pubmed/30072901`.

[109] Krzysztof Woniak and Tadeusz M. Krygowski. Crystallographic studies and physicochemical properties of -electron systems: Part xviii. crystal and molecu-

lar structure of n-n-propyl-quinoxalinium 7,7,8,8-tetracyano-p-quinodimethanide: estimation of charge at tcnq by the hose model. *Journal of Molecular Structure*, 193:81–92, 1989. ISSN 0022-2860. doi: https://doi.org/10.1016/0022-2860(89)80123-1. URL `http://www.sciencedirect.com/science/article/pii/0022286089801231`.

[110] H. D. Wu, F. X. Wang, Y. Xiao, and G. B. Pan. Preparation and ambipolar transistor characteristics of co-crystal microrods of dibenzotetrathiafulvalene and tetracyanoquinodimethane. *J. Mater. Chem. C.*, 1(12):2286–2289, 2013.

[111] Fred Wudl, Darold Wobschall, and Earl J. Hufnagel. Electrical conductivity by the bis(1,3-dithiole)-bis(1,3-dithiolium) system. *Journal of the American Chemical Society*, 94(2):670–672, 1972. ISSN 0002-7863. doi: 10.1021/ja00757a079. URL `https://doi.org/10.1021/ja00757a079`.

[112] Hiroshi Yada, Jiro Tanaka, and Saburo Nagakura. Infrared absorption spectrum of charge-transfer complex between trimethylamine and iodine. *Journal of Molecular Spectroscopy*, 9:461–468, 1962. ISSN 0022-2852. doi: https://doi.org/10.1016/0022-2852(62)90251-5. URL `http://www.sciencedirect.com/science/article/pii/0022285262902515`.

[113] R. Zeiz. Single crystal field-effect transistors. Report, University of Konstanz, 2005.

[114] Ly. Zhu, Eg. Kim, Yp. Yi, and Jl. Bredas. Charge transfer in molecular complexes with 2,3,5,6-tetrafluoro-7,7,8,8-tetracyanoquinodimethane (f-4-tcnq): A density functional theory study. *Chem. Mat.*, 23(23):5149–5159, 2011. ISSN 0897-4756. doi: 10.1021/cm201798x.

[115] Weigang Zhu, Yuanping Yi, Yonggang Zhen, and Wenping Hu. Precisely tailoring the stoichiometric stacking of perylene- tcnq co-crystals towards different nano and microstructures with varied optoelectronic performances. *Small (Weinheim an der Bergstrasse, Germany)*, 11(18):2150, 2015. doi: 10.1002/smll.201402330.